Spring 2011

MDCT-based dynamic, subject-specific lung models via image registration for CFD-based interrogation of regional lung function

Youbing Yin
University of Iowa

MDCT-BASED DYNAMIC, SUBJECT-SPECIFIC LUNG MODELS VIA IMAGE REGISTRATION FOR CFD-BASED INTERROGATION OF REGIONAL LUNG FUNCTION

by

Youbing Yin

An Abstract

Of a thesis submitted in partial fulfillment of the
requirements for the Doctor of Philosophy
degree in Mechanical Engineering in the
Graduate College of The
University of Iowa

May 2011

Thesis Supervisors: Professor Ching-Long Lin
Professor Eric A. Hoffman

ABSTRACT

Computational fluid dynamics (CFD) has become an attractive tool in understanding the characteristic of air flow in the human lungs. Due to inter-subject variations, subject-specific simulations are essential for understanding structure-function relationship, assessing lung function and improving drug delivery. However, currently the subject-specific CFD analysis remains challenging due, in large part to, two issues: construction of realistic deforming airway geometry and imposition of physiological boundary conditions. To address these two issues, we develop subject-specific, dynamic lung models by utilizing two or multiple volume multi-detector row computed tomography (MDCT) data sets and image registrations in this thesis. A mass-preserving nonrigid image registration algorithm is first proposed to match a pair of three-dimensional (3D) MDCT data sets with large deformations. A novel similarity criterion, the sum of squared tissue volume difference (SSTVD), is introduced to account for changes in intensity with lung inflation. We then demonstrate the ability to develop dynamic lung models by using a pair of lung volumes to account for deformations of airway geometries and subject-specific boundary conditions. The deformation of the airway geometry is derived by the registration-derived displacement field and subject-specific boundary condition is estimated from registration-predicted regional ventilation in a 3D and one-dimensional (1D) coupled multi-scale framework. Improved dynamic lung models are then proposed from three lung data sets acquired at different inflations by utilizing nonlinear interpolations. The improved lung models account for nonlinear geometry motions and time-varying boundary conditions during breathing. The capability of the proposed dynamic lung model is expected to move the CFD-based

interrogation of lung function to the next plateau.

Abstract Approved: _____
Thesis Supervisor

_____
Title and Department

_____
Date

_____
Thesis Supervisor

_____
Title and Department

_____
Date

MDCT-BASED DYNAMIC, SUBJECT-SPECIFIC LUNG MODELS VIA IMAGE REGISTRATION FOR CFD-BASED INTERROGATION OF REGIONAL LUNG FUNCTION

by

Youbing Yin

A thesis submitted in partial fulfillment of the
requirements for the Doctor of Philosophy
degree in Mechanical Engineering in the
Graduate College of The
University of Iowa

May 2011

Thesis Supervisors: Professor Ching-Long Lin
Professor Eric A. Hoffman

Graduate College
The University of Iowa
Iowa City, Iowa

CERTIFICATE OF APPROVAL

PH.D. THESIS

This is to certify that the Ph.D. thesis of

Youbing Yin

has been approved by the Examining Committee
for the thesis requirement for the Doctor of
Philosophy degree in Mechanical Engineering at the
May 2011 graduation.

Thesis Committee: Ching-Long Lin, Thesis Supervisor

Eric A. Hoffman, Thesis Supervisor

James H.J. Buchholz

Joseph M. Reinhardt

Merryn H. Tawhai

To Juan

ACKNOWLEDGMENTS

The work presented in this thesis could not have been done without the support and assistance of many others. I am very grateful for all the support from the staff and other students in the labs throughout the years. First of all, I would like to thank Drs. Ching-Long Lin and Eric Hoffman, my thesis advisors, for their guidance and support throughout this project. Their encouragement during the course of this research is sincerely appreciated.

In addition, I would like to thank Drs. Merryn Tawhai, Joe Reinhardt, James Buchholz, Gary Christensen, Jia Lu, Junfeng Guo and Guohua Xia. Such an interdisciplinary project cannot go so smooth without the help from all those experts. I have also enjoyed working with labmates Jiwoong Choi, Nathan Ellingwood, Matthew Fuld, Ahmed Halaweish, Haribalan Kumar, Dragos Vasilescu and so on and I want to thank them for valuable discussions. I also thank many fellow students from other departments including Kunlin Cao, Kai Ding, Qi Song and Yin Yin for being helpful.

Finally, I would like to thank my family and friends. Most importantly I want to thank to my wife, Juan Pang, for her love and support throughout this process.

This work was supported in part by NIH Grant Nos. NIH-R01-HL-064368, NIH-R01-EB-005823, NIH-S10-RR-022421, and R01-HL-094315. Computer time for CFD simulation was allocated by TeraGrid via the Texas Advanced Computing Center.

ABSTRACT

Computational fluid dynamics (CFD) has become an attractive tool in understanding the characteristic of air flow in the human lungs. Due to inter-subject variations, subject-specific simulations are essential for understanding structure-function relationship, assessing lung function and improving drug delivery. However, currently the subject-specific CFD analysis remains challenging due, in large part to, two issues: construction of realistic deforming airway geometry and imposition of physiological boundary conditions. To address these two issues, we develop subject-specific, dynamic lung models by utilizing two or multiple volume multi-detector row computed tomography (MDCT) data sets and image registrations in this thesis. A mass-preserving nonrigid image registration algorithm is first proposed to match a pair of three-dimensional (3D) MDCT data sets with large deformations. A novel similarity criterion, the sum of squared tissue volume difference (SSTVD), is introduced to account for changes in intensity with lung inflation. We then demonstrate the ability to develop dynamic lung models by using a pair of lung volumes to account for deformations of airway geometries and subject-specific boundary conditions. The deformation of the airway geometry is derived by the registration-derived displacement field and subject-specific boundary condition is estimated from registration-predicted regional ventilation in a 3D and one-dimensional (1D) coupled multi-scale framework. Improved dynamic lung models are then proposed from three lung data sets acquired at different inflations by utilizing nonlinear interpolations. The improved lung models account for nonlinear geometry motions and time-varying boundary conditions during breathing. The capability of the proposed dynamic lung model is expected to move the CFD-based

interrogation of lung function to the next plateau.

TABLE OF CONTENTS

LIST OF TABLES ix

LIST OF FIGURES x

CHAPTER

1 INTRODUCTION 1

1.1 Motivation 1
1.2 Background 3
1.2.1 Lung Anatomy And Physiology 3
1.2.2 MDCT Imaging 5
1.2.3 Regional Ventilation 6
1.2.4 MDCT-Based Quantitative Analysis 7
1.2.5 Image Registration 8
1.3 Aims 9
1.4 Thesis Overview 10

2 MASS PRESERVING NONRIGID REGISTRATION 15

2.1 Introduction 15
2.2 Methods 17
2.2.1 Transformation Model 17
2.2.2 Similarity Measure 20
2.2.3 Optimization 23
2.2.4 Summary 24
2.3 Experiments And Results 24
2.3.1 MDCT Image Data 24
2.3.2 Experimental Setup 25
2.3.3 Results 26
2.4 Discussion 29

3 HYBRID IMAGE REGISTRATION FOR MOVING AIRWAY GEOMETRY 41

3.1 Introduction 41
3.2 Methods 44
3.2.1 Hybrid Registration 44
3.2.2 Dynamic Lung Model 48
3.3 Results 49
3.3.1 Experiments With 2D Binary Images 49
3.3.2 Experiments With 3D MDCT Lung Images 51

3.3.3 Moving Airway Geometry 53
3.4 Discussion 54

4 SUBJECT-SPECIFIC BOUNDARY CONDITIONS 66

4.1 Introduction 66
4.2 Methods 68
4.2.1 Method Overview 68
4.2.2 MDCT Image Acquisition 69
4.2.3 Registration-Derived Regional Ventilation 69
4.2.4 Subject-Specific Boundary Conditions 70
4.2.5 CFD Simulation 71
4.3 Results 73
4.3.1 Registration Accuracy 73
4.3.2 1D Centerline Airway Trees 73
4.3.3 Regional Ventilation 74
4.3.4 CFD Results 75
4.3.5 Analysis Of Repeatability 77
4.4 Conclusion 79

5 BREATHING LUNG MODEL 94

5.1 Introduction 94
5.2 Methods 94
5.2.1 Method Overview 94
5.2.2 MDCT Image Acquisition 95
5.2.3 Image Registration 96
5.2.4 Moving Airway Geometry 97
5.2.5 Time-Varying Boundary Conditions 98
5.3 Results 101
5.3.1 Registration Accuracy 101
5.3.2 Moving Airway Geometry 101
5.3.3 Time-Varying Boundary Conditions 103
5.3.4 Dynamic Lung Model 105
5.4 Discussion 105

6 SUMMARY AND FUTURE WORK 119

6.1 Summary 119
6.1.1 Mass-Preserving Nonrigid Registration 119
6.1.2 Moving Airway Geometry 120
6.1.3 Subject-Specific Boundary Conditions 120
6.1.4 Breathing Lung Model 121
6.2 Future Work 121
6.2.1 Effects Of Airway Branching Patterns 122

6.2.2 Effects Of Gas Properties 122
6.2.3 Accounting For Lobar Sliding 123

BIBLIOGRAPHY 130

LIST OF TABLES

Table

2.1 The total lung volume (TLV), air volume (AV) and tissue volume (TV) for all six registration pairs are estimated from HU. 32

2.2 Statistical comparison of landmark errors between the SSTVD method, the SSD method and the MI method for all six registration pairs. . 33

3.1 Landmark distance and metric value of SSD before and after registrations with four approaches: LBR, IBR, LIBR and TPS-LIBR for 2D binary image experiments. 55

4.1 Comparison between measured and registration-derived values for average Jacobian value and total air volume difference. 82

4.2 Relative errors of the lobar distributions of flow rate ratio for the three outlet boundary conditions against measured values. 83

4.3 Mean and standard deviation of Jacobian and air volume change (AVC) across all subjects for three registration combinations (FRC1-TLC, FRC2-TLC, FRC2-FRC1). 84

LIST OF FIGURES

Figure

1.1 Definition of lung volumes and capacities. 13

1.2 A two-dimensional (2D) illustration of nonrigid image registration. An image with a square outer boundary and a circular inner boundary is mapped to the one with a circular outer boundary and a square inner boundary. The centers of objects are also shifted. It is noted that the warping function is defined in the domain of the image I_1 from a Lagrangian viewpoint while the warped image is obtained by transforming the image I_2 to the domain of image I_1 from an Eulerian viewpoint. 14

2.1 Framework of the multi-resolution strategy 34

2.2 A sketch of the nonrigid registration procedure. 35

2.3 Locations of the landmarks (marked by spheres) at TLC (a) and FRC (b) for the registration pair A. Surface rendering of five lobes and major vessel branches is shown for reference. 36

2.4 Distribution of landmark distance along the z-axis (from apex to base) before (a) and after registrations (b) using the SSTVD method (filled diamond) and the SSD method(unfilled circle) for the registration pair A. Note that all landmarks have an approximately uniform error distribution from apex to base for the SSTVD method while they have a large deviation of error for the SSD method in (b). . . 37

2.5 Surface distance maps of the warped TLC major vessel tree to the FRC major vessel tree for the SSTVD method (a) and the SSD method (b). The FRC major vessel tree is shown in white for reference. Note that the red segments in (a) are caused by missing segments in FRC major tree, not by mis-registration. Examples are marked as A and B. Segments with large errors in (b), marked as C,D,E, are due to clear mis-registration, as one can easily see that the white unwarped segments mis-align with the color coded tree. . 38

2.6 A slice from the registration pair A. (a) Slice from the reference image. (b) Corresponding slice from the warped image with the SSTVD method. (c) Corresponding slice from the warped image with the SSD method. Notice a mis-alignment of vessel trees indicated by the arrow for the SSD method in (c). 39

2.7 A slice from the registration pair F. (a) Slice from the reference image. (b) Corresponding slice from the warped image with the SSTVD method. (c) Corresponding slice from the warped image with the SSD method. Notice the good alignment between the lobar fissures (highlighted in lines) and between the vessel trees for the SSTVD method in (b) while an obvious mis-alignment of the fissure and vessels for the SSD method in (c). 40

3.1 Sketch of the multi-resolution framework and flow chart of the whole registration procedure for the hybrid registration approach. The sketch of the framework is illustrated in 2D but the basic idea also works for 3D. 56

3.2 "2D Squares" experiment. Column (a) shows the reference (top) and floating (middle) images, where the landmarks are marked and labeled with the numbers showing the correspondence; columns (b)-(e) show the results for registrations with LBR, IBR, LIBR, and TPS-LIBR, respectively. The deformed image (top), the deformed grid (middle) as well as the enlarged view of the deformed grid (bottom) are presented for each approach. 57

3.3 "2D Circles" experiment. Column (a) shows the reference (top) and floating (middle) images, where the landmarks are marked and labeled with the numbers showing the correspondence; columns (b)-(e) show the results for registrations with LBR, IBR, LIBR, and TPS-LIBR, respectively. The deformed image (top), the deformed grid (middle) as well as the enlarged view of the deformed grid (bottom) are presented for each approach. 58

3.4 Illustrate of landmark locations for (a) TLC and (b) FRC from one subject. The landmarks used for matching are marked by 'A' and the landmarks used for validation are marked by 'B'. Surface rendering of airways, major vessels and lungs is shown for reference. 59

3.5 Landmark distance of the validation landmarks before and after registrations with LBR, IBR and Hybrid across all registration pairs. . 60

3.6 Surface distance map of the registration-predicted FRC airway tree to the original FRC airway trees for LBR (a), IBR (b) and Hybrid (c). The original FRC airway trees are shown in white for reference. 61

3.7 Airway geometries at four different time points from the dynamic airway model for a TLC-FRC image pair with the LIBR method. The lung volume difference between the two images is 2.4 liters. From left to right: $t = 0$; $t = T/6$; $t = T/3$; and $t = T/2$ (T is the period). . . 62

3.8 Airway geometries at four different time points from the dynamic airway model for the 85%VC-55%VC image pair with the LBR method. The lung volume difference between the two images is 1.5 liters. From left to right: $t = 0$; $t = T/6$; $t = T/3$; and $t = T/2$ (T is the period). 63

3.9 Deformed geometries at four different time points from the dynamic lung model for the 85%VC-55%VC image pair with the LBR method. From left to right: $t = 0$; $t = T/6$; $t = T/3$; and $t = T/2$ (T is the period). Lobes, 3D upper and center airways, and 1D centerline airways are shown here. 64

3.10 Velocity contour in a vertical plane at four selected time points from the dynamic airway model for the 85%VC-55%VC image pair. The registration-derived deformation between the two scanned lung volumes is scaled down to a normal quiet breathing with a tidal volume of 500 ml. 65

4.1 A flow chart of the entire process to describe subject-specific boundary conditions. 85

4.2 Visual assessment of registration accuracy. A sagittal slice of the left lung from (a) the image I_r, (b) the warped image obtained by image registration, and (c) the image I_f at the same axial locations. . . . 86

4.3 Lobar and airway geometries. (a) Surface geometries of the lobes, MDCT-resolved upper and central airways for the image I_r. (b) 1D centerline airway trees generated with the volume filling method. The 3D MDCT-resolved upper airway, central airway tree and its skeleton (Orange) are also shown in (b) for reference. Different colors are used in both (a) and (b) for each lobe and lobar airway: green for left upper lobe (LUL), red for left lower lobe (LLL), cyan for right upper lobe (RUL), blue for right middle lobe (RML) and purple for right lower lobe (RLL). 87

4.4 Plots of the number of branches and the mean length on log scales against Strahler order. Regression line for each plot is also shown. 88

4.5 Outlet velocity vectors (pink) and pressure contours for the three different outlet boundary conditions: (a) proposed; (b) uniform velocity; (c) uniform pressure. 89

4.6 Lobar distribution of flow rate ratio for the three cases with different outlet boundary conditions. 90

4.7 Snapshots of particle transport (black dots) with an isosurface of airflow speed (1.7 m/s, green contour) for the three different outlet boundary conditions: (a) proposed; (b) uniform velocity; and (c) uniform pressure. 91

4.8 Lobar distribution of deposition fraction (top row) and ventilation fraction (bottom row) for the three cases with different outlet boundary conditions. 92

4.9 Bland-Altman plot of Jacobian and AVC between FRC1-TLC and FRC2-TLC registration. Solid line indicates upper and lower limits of agreement (2*S.D.). 93

5.1 A flow chart of the entire process to develop the breathing lung model. 107

5.2 Changes in normalized inhaled air flow rate and lung volume with time during a breathing cycle. Locations of the imaged lung volumes are marked on the curve. 108

5.3 Visual assessment of registration accuracy. A sagittal slice from (a) the image I_1, (b) the warped image of I_2, (c) the warped image of I_3, (d) the image I_2, and (e) the image I_3 at the same axial locations, respectively. All panels have the same sizes. 109

5.4 3D MDCT-derived airway geometries segmented from the three lung volumetric images: Red for I_1 (80% VC), green for I_2 (60% VC), and blue for I_3 (20% VC). 110

5.5 Comparison between the segmented airway from I_2 (60% VC) and the airway deformed from I_1 with the transform function $\mathbf{T}_{12}$: (a) whole airway from I_2 (green) and the deformed airway (pink); (b) the extracted curves from the I_2 (green) and from the deformed airway (pink dot) at a cross-section in the middle of trachea; (c) the extracted curves from the I_2 (green) and from the deformed airway (pink dot) at a cross-section after the carina. The undeformed airway geometry from I_1 at those two cross-sections are shown in red in both (b) and (c). In addition, an interpolated airway at 60%VC using the linear interpolation between the two lung volumes I_1 and I_3 is also shown in gray (surface or curves) to demonstrate the insufficiency of the linear interpolation. 111

5.6 Comparison between the segmented airway from I_3 (20% VC) and the airway deformed from I_1 with the transform function $\mathbf{T}_{13}$: (a) whole airway from I_3 (blue) and the deformed airway (orange); (b) the extracted curves from the I_3 (blue) and from the deformed airway (orange dot) at a cross-section in the middle of trachea; (c) the extracted curves from the I_3 (blue) and from the deformed airway (orange dot) at a cross-section after the carina. The undeformed airway geometry from I_1 at those two cross-sections are shown in red in both (b) and (c). 112

5.7 3D MDCT-resolved airway and generated 1D centerline airway from two views: (a) coronal and (b) sagittal. The generated airways are shown in different colors for each lobe: red for left upper lobe (LUL), green for left lower lobe (LLL), cyan for right upper lobe (RUL), blue for right middle lobe (RML) and pink for right lower lobe (RLL). . 113

5.8 Strahler-order-based log plots of number of branches and mean length for the generated 1D model. Both plots show log-scaled linear trends, consistent with existing morphometric analysis of the human bronchial tree. 114

5.9 The distributions of air volume associated with each terminal bronchiole for three data sets: (a) I_1, (b) I_2 and (c) I_3. The unit is mm^3. 115

5.10 The distribution of the air volume change associated with each terminal bronchiole for three data sets: (a) I_1, (b) I_2 and (c) I_3. The unit is mm^3. The air volume changes are calculated relative to the image I_1 and reflect the air flow associated with each terminal bronchiole. 116

5.11 Time-varying air flows associated with terminal bronchioles for four selected locations in the lung. The locations are marked with spheres in different colors and the curves of air flows at the four locations are plotted in the same colors as the corresponding locations. 117

5.12 Moving airway geometry and air flow associated with terminal bronchioles extracted from the breathing lung model at four different time points in a breathing cycle: (a) t=0; (b) t=T/6; (c) t=T/3; (d) t=T/2, with T as the period. (a) and (d) correspond to the lung volume, I_1, and lung volume, I_3, respectively. 118

6.1 Comparisons between MRI-based ^{3}He distribution and MDCT-based AVC map for three subjects. Two transverse sections are shown for each subject. 126

6.2 Normalized mean AVC or ^{3}He ventilation as a function of normalized lung height (dorsal-ventral) for three subjects. There are similar but not identical distribution patterns. 3He is consistently higher in the ventral lung regions (blue oval), possibly due to gas properties. . . . 127

6.3 Displacement profile of tangent components along a line perpendicular to the fissure surface at three different locations (left: near apex; middle: near lingula; and right: near base) for both the whole-lung-based (square) and the lobe-based (circle) methods. 128

6.4 Top row shows the sketches for 2D synthetic cases. Left: Complete Plane-Parabolic, a complete plane "fissure" is deformed into a parabolic surface; Middle: Complete Plane-Plane, a complete plane "fissure" is deformed with changed orientation; Right: Incomplete Plane-Plane, an incomplete plane "fissure" is deformed with changed orientation. A pair of adjacent points on the initial interface (marked by filled and unfilled squares on the solid lines) is deformed into corresponding points on the dashed lines. A reference line A-A is marked in red. The bottom row shows the comparisons of $x-$ and y-components of displacements (u, v) between predicted results and exact solutions along A-A from left to right for the three cases, respectively. It can be seen that overall the proposed approach could recover the true deformation field for all the three cases. Discontinuities of both normal (u) and tangent (v) components of displacements for cases with complete or incomplete "fissures" are captured and are consistent with the ground truth. 129

CHAPTER 1
INTRODUCTION

1.1 Motivation

Computational fluid dynamics (CFD) has been extensively utilized to simulate respiratory flows in the past two decades. A direct motivation is that a thorough understanding of the flow characteristics in airways can help predict the local deposition of therapeutic or pollutant particles. There is a growing interest to take the lungs as an alternative route for drug delivery [25]. Additionally evidence has shown that pollutant particle depositions in the lungs play a key role in the development of lung diseases [49]. Since particle deposition is highly dependent on flow characteristics, which, in turn, are dependent on the geometrical configuration of airways and regional ventilation of the lungs, it is desirable to conduct subject-specific CFD analysis.

Existing work has provided some insights into the characteristics of flow inside lungs and has also demonstrated the potential ability to understand structure-function relationships in the individual (see review article [107]). However, the subject-specific CFD analysis remains challenging due, in large part, to two issues: (1) construction of realistic deforming airway geometry and (2) imposition of physiological boundary conditions.

With regards to the first aspect, the airway geometry has been rapidly developed: from the symmetry symmetric Weibel model [120] or the asymmetric Horsfield model ([43] used in the earliest studies into the anatomically accurate and subject-specific airway geometries based on *in*-vivo volumetric imaging [11, 28, 64, 65]. Despite of such rapid development, the airway geometries in most of these studies

have generally been assumed to be rigid structures and deformations have been neglected. Deformations of conducting airways may be small in quiet breathing. However, during moderate, heavy and forced breathing, conducting airways may undergo large deformations. In addition, central airway collapse can be seen in some lung diseases [68], which results in significant changes in cross-sections of trachea. For example, from some patients with severe asthma we found that the cross section of trachea could be deformed from a circle at TLC into a triangle at FRC. Without considering the realistic deformations of airway geometries, the interaction between wall motion and air flows is neglected, which may affect flow patterns, particle depositions and, especially, the wall shear stress. It is known that the flow induced wall shear stress can alter cell shape and trigger different levels of cell signaling, which may be important in airway remodeling and abnormalities.

The second issue is how to describe a physiological boundary condition, which is also a common issue in simulations of other physiological flows, such as blood flows in the human arterial system [31, 98], nasal air flows [110] and so on. CFD is to numerically solve a set of differential equations and a boundary condition must be defined so that a unique solution to the equations can be determined. Thus, it is important to impose a physiologically consistent boundary condition for CFD simulation of pulmonary air flows. However, due to difficulties with measuring the *in*-vivo pressure and flow inside lungs, the approach taken in earlier CFD analysis had been to impose equal pressure or flow boundary conditions at the outlets of peripheral airways, neglecting the highly non-uniform regional ventilation.

With advances in imaging and computing technologies, it is now possible to address these two issues and perform subject-simulation by utilizing multi-detector

row computed tomography (MDCT)-based data sets and image registrations.

1.2 Background

1.2.1 Lung Anatomy And Physiology

Human lungs are the essential respiratory organs. The main function is to facilitate gas exchange between human body and the atmosphere. Human lungs consist of left and right lungs and the two lungs are located in the chest on either side of the heart. Each lung is surrounded by a completely closed pleural cavity. The pleura folds back onto itself and forms a two-layered, membrane structure. The outer pleura is attached to the chest wall. The inner pleura covers the lungs and divides the two lungs into five lobes. The left lung has two lobes, left upper lobe (LUL) and left lower lobe (LLL), separated by an oblique fissure. The right lung has three lobes, right upper lobe (RUL), right middle lobe (RML) and right lower lobe (RLL). The RUL and RML are separated by a horizontal fissure and the RML and RLL are separated by an oblique fissure. It is well known that lobes can slide against the chest wall and adjacent lobes [81]. Such motion may provide a means to reduce lung parenchymal distortion and avoid regions of high local stress. Conversely, it has previously been shown that lobar fissures fibrose and essentially disappear in animals (sloths) which undergo very little chest wall shape changes [40].

Gas is transported between lungs and the atmosphere through airways, which consist of a series of branching tubes with progressively decreasing dimensions. It is believed that such a bifurcation network connects to about 300 million alveoli, where gas exchange between air and blood takes place. Gas inspiration and expiration are driven by the pressure differences between the atmosphere and chest. During

inspiration, as the diaphragm contracts, the chest volume increases and the pressure inside it decreases, causing air to flow from the atmosphere through airways into the alveoli. During expiration, lung passively returns to its pre-inspiratory volume because of elasticity. Pressure inside lungs increases and forces air to flow from the alveoli through airways out to the atmosphere. According to the volume of air associated with different phrases of the respiratory cycle, we can then define lung capacities/volumes as shown in Figure 1.1. Their definitions are as follows:

Tidal volume : the air volume breathed in and out during a normal breath. Typical values are around $500ml$ for an adult.

Residual volume (RV) : the amount of air left in the lung after a maximum expiration.

Vital Capacity (VC) : the maximum amount of air volume that can be breathed in after a maximum expiration. It can be directly measured by a spirometer and is used in our lab-developed volume controller system to standardize the lung volume during imaging.

Total lung capacity (TLC) : the amount of air left in the lungs after a maximum inspiration. It is equivalent to 100% of VC.

Functional residual capacity (FRC) : the amount of air left in the lungs after a normal expiration.

Beside the air flow, there exists a blood circulation inside the lungs. Blood is pumped from the right ventricle through the pulmonary arteries and travels through the lungs, where it releases carbon dioxide and picks up oxygen during respiration.

The gas exchange occurs between capillaries and alveoli. The oxygenated blood then leaves the lungs through pulmonary veins to the left atrium.

1.2.2 MDCT Imaging

The CT scanner measures density map of the imaged object. Spiral CT was developed to allow for volumetric image of the lung in a short time. The image data are acquired as the scanner table is continuously moved through the scanner while the x-ray tube rotates. Three-dimensional (3D) data are then obtained by image reconstruction. With advances in imaging and reconstruction techniques, MDCT scanner can use multiple detector rows to collect more slices per rotation, thus allowing for increased z-coverage and fast acquisition speed. Currently MDCT has emerged as a powerful tool for imaging the lung due to its high spatial resolution, high signal:noise ratio and high acquisition speed. It has been used to provide anatomical and increasingly functional information of lungs. With the aid of CT images, anatomical information, such as lungs [44], lobes [114, 117], bronchial trees [112] and vessel trees [94], can be extracted and reconstructed in three dimensions. This provides accurate measurement of lung volumes, regional lung density as well as dimensions of airway and vascular trees [36, 39, 96]. Functional information can also be measured with the aid of contrast imaging or post-processing techniques. For example, regional ventilation can quantitatively be assessed with xenon-enhanced CT (Xe-CT) [14, 29, 72, 95, 103] and regional perfusion can be estimated with imaging with bolus contrast injection [2, 37, 122]. With regards to image-based modeling, such information derived from MDCT imaging is valuable for subject-specific simulations of pulmonary air flow inside human lungs. The anatomical information provides realistic subject-specific geometries while the functional

information provides physiologically meaningful boundary conditions.

Since lung volume changes as lung is breathing, it is important to standardize imaging protocols so that subjects are scanned at similar lung volumes. Commonly, static volumetric lung images are acquired during breath-holds at well controlled lung volumes to minimize artifacts caused by respiratory motion. In addition, four-dimensional (4D) dynamic imaging of lungs is also possible with respiratory gating or retrospective gating methods. 4D CT has been used to assess the lung function [8, 22, 32] and simulate lung tissue motion [1, 4, 26, 121, 127]. However, to our knowledge, 4D CT has not been applied to CFD studies. In this thesis, all CT data sets were acquired during breath-holds under scanning protocols approved by the University of Iowa's Institutional Review Board.

1.2.3 Regional Ventilation

Regional ventilation is used to quantify local gas exchange inside lungs. Since it highly correlates with lung function, accurate assessment of regional ventilation is essential for the diagnosis and evaluation of pathological conditions. Distribution of ventilation inside lungs is affected by many factors, such as airway geometries (diameters, branching patterns, etc), tissue mechanical properties, berating rate, postures, and so on. Several non-invasive imaging techniques have been developed to indirectly or directly measure regional ventilation. Nuclear medicine imaging methods, such as positron emission tomography (PET) and single-photon emission tomography (SPECT), provide estimation of regional ventilation by imaging spatial and of inhaled gas or aerosol (as tracer) [35]. Magnetic resonance imaging (MRI) using hyperpolarized helium gas is a non-radioactive method of measuring ventilation

[86, 115]. In contrast to these imaging modalities, MDCT is able to provide high-resolution quantification of pulmonary function. With inert and non-radioactive xenon gas as a contrast agent, MDCT yields better estimation of regional ventilation by measuring wash-in and wash-out time rates over multiple breaths [14, 72, 103]. In addition, ventilation has also been estimated based on changes in image intensities observed between two MDCT images [29] or image-registration-derived deformation [15, 32, 47, 79], where specific volume changes (normalized volume change by the initial air volume) or Jacobian values (ratio of volumes) are used to reflect regional ventilation.

1.2.4 MDCT-Based Quantitative Analysis

Image data acquired by CT scanners is usually displayed as a gray scale image with intensity values denoted by reconstructed Hounsfield unit (HU). The reconstructed HU of a non-contrast lung images can be used to estimate the amount of air or tissue in each voxel. It is assumed that HU of lung is primarily contributed by two components: tissue (parenchyma plus blood) and air. Any unit of lung may be considered a linear combination of these two compartments. Thus, the fractional air and tissue contents in a region can be estimated from HU. Let $I(x)$ denote HU for a voxel at $\mathbf{x}$. The tissue and air fraction can be estimated as

$$\gamma_{\text{air}}(I(\mathbf{x})) = \frac{\text{HU}_{\text{tiss}} - I(\mathbf{x})}{\text{HU}_{\text{tiss}} - \text{HU}_{\text{air}}} \tag{1.1}$$

$$\gamma_{\text{tiss}}(I(\mathbf{x})) = \frac{I(\mathbf{x}) - \text{HU}_{\text{air}}}{\text{HU}_{\text{tiss}} - \text{HU}_{\text{air}}}, \tag{1.2}$$

where HU_{air} and HU_{tiss} refer to HUs of air and tissue, respectively. HUs of imaged air and tissue can be sampled in the center of the trachea (air) and aorta (blood). In this work, we use-1000 for HU_{air} and 55 for HU_{tiss} since all CT data sets were

from a well calibrated scanner.

Based on this technique, we can measure air and tissue volumes in a specific region [38, 40]. There is currently considerable interest in quantifying the distribution of intensity values within CT images with the purpose of identifying disease early and following disease progression. For example, quantification of pulmonary fibrosis and emphysema has been based on identifying voxels inside lungs that fall outside of an empirically derived HU threshold [39, 58, 74, 80]. In addition, by acquiring a pair of images at different levels of inflation, we can also estimate local air volume change if a spatial mapping between two images is given, thus providing a way to estimate regional ventilation. Such information provides a way to describe physiologically meaningful boundary conditions for CFD studies.

1.2.5 Image Registration

Image registration is a process of determining an optimal spatial mapping that matches images collected at different times or using different imaging modalities. Given a pair of images I_1 and I_2, referred to as the reference and the floating images, image registration tries to determine an optimal warping function by minimizing a dissimilarity measure, also referred to as a cost function. Since lung motion varies from apex to base and ventral to dorsal, it is desirable to use nonrigid image registration to capture non-uniform deformation. Once an image registration is performed, the resulting warping function can be used to transform the floating image into the reference image domain from an Eulerian viewpoint, obtaining the warped image. Ideally, the warped image should be close to the image I_1. A 2D illustration of image registration is shown in Figure 1.2.

Image registration is becoming a key tool in medical image analysis as one

seeks to link images across modalities, across time, or between lung volumes in the use of pulmonary investigations. Registrations of lung data sets have been extensively investigated by several groups. A representative though not exhaustive list of such studies can be found in [7, 30, 34, 47, 97]. Of particular interest to this work is the registration of MDCT-derived 3D lung images with applications to subject-specific CFD studies of pulmonary gas flow. Image registration has at least two potential applications in subject-specific lung modeling: 1) estimation of regional ventilation, and 2) deformation of the airway geometries. With respect to the first application, registration-derived estimates of regional ventilation can produce physiologically consistent, subject-specific boundary conditions. For the second application, the registration-derived mapping can be used to deform the CFD meshes and extend studies from rigid airways to deforming airways as in realistic breathing lungs.

1.3 Aims

The main objective of this research is to develop MDCT-based dynamic, subject-specific lung models via image registration for CFD-based interrogation of regional lung function. Such dynamic lung models account for realistic deforming airway geometries and physiological boundary conditions, thus addressing the two issues discussed above. The specific aims are listed as follows:

1. Developing a nonrigid image registration algorithm to match 3D volume-controlled MDCT lung images acquired at different levels of inflation.

    - The nonrigid registration algorithm should be capable of recovering large deformation between images obtained at full inspiration and full or partial expiration for human subjects.

- Validation is performed to evaluate the accuracy of the registration algorithm.

2. Developing an image-based lung model by accounting for realistic deformations of airway geometries

   - Warping function obtained from image registration is used to adjust airway geometries for changes in lung volumes.
   - CFD simulation in rigid airway geometry is extended to breathing lungs with moving airway geometry.

3. Further developing the image-based lung model by accounting for physiological boundary conditions for CFD simulation.

   - Physiological boundary conditions are described based on registration-derived regional ventilation.
   - Proposed boundary condition is used for CFD simulation and is compared against traditional uniform boundary conditions.

The proposed dynamic lung model overcomes the two main obstacles encountered for subject-specific simulation. Its capability will bring about new understanding of the structure-function relationship in pulmonary air flow.

1.4 Thesis Overview

In this thesis, we first achieve each specific aim listed in Section 1.3 by using two volume-controlled MDCT data sets in Chapters 2, 3 and 4. With consideration of radiation dose, two lung volumes are commonly acquired with one imaged at full inspiration (TLC) and the other at end expiration (FRC, or RV). TLC can

provide detailed information related to airway geometry while FRC or RV provides information related to air trapping. However, only a linear interpolation is available with two lung volumes and such a linear interpolation may not be accurate to describe the lung motion. Thus, in Chapter 5, we integrate all the components and develop a dynamic lung model from three lung volumes. By adding an additional lung volume, a nonlinear interpolation can be utilized to account for the nonlinear geometry motion and time-varying boundary conditions during breathing. In addition, the framework is general and can be easily extended to the cases with more lung volumes and also 4D CT data sets in the future.

The rest of the thesis is organized as follows. In Chapter 2, a novel mass-preserving nonrigid image registration method is proposed to match two MDCT lung data sets acquired during breath-holds at different lung volumes. Its performance is evaluated using pairs of MDCT volumetric data sets acquired near TLC and FRC. This chapter is based on

- Yin, Y., Hoffman, E. A., Lin, C.-L., 2009. Local tissue-weight-based non-rigid registration of lung images with application to regional ventilation. In: Proceedings of SPIE Medical Imaging. Vol. 7262. Orland, US, p. 72620C.

- Yin, Y., Hoffman, E. A., Lin, C.-L., 2009. Mass preserving nonrigid registration of CT lung images using cubic B-spline. Medical Physics 36 (9), 4213–4222.

In Chapter 3, we first improve the registration algorithm by incorporating the landmark information at bifurcations of airway and vascular trees. By utilizing the improved registration, we demonstrate the ability to deform the airway geometry from a pair of two MDCT images. This chapter is based on

- Yin, Y., Hoffman, E. A., Ding, K., Reinhardt, J. M., Lin, C.-L., 2011. A cubic B-spline-based hybrid registration of lung CT images for a dynamic airway geometric model with large deformation. Physics in Medicine and Biology 56 (1), 203–218.

Chapter 4 presents a novel technique to estimate a physiological boundary condition from two MDCT lung data sets. The derived boundary condition is then applied for CFD simulation of pulmonary air flow and is compared against two traditional boundary conditions (uniform velocity or uniform pressure). It is based on

- Yin, Y., Choi, J., Hoffman, E. A., Tawhai, M. H., Lin, C.-L., 2010. Simulation of pulmonary air flow with a subject-specific boundary condition. Journal of Biomechanics 43 (11), 2159 – 2163.

In Chapter 5, we integrate the approaches proposed in Chapters 3 and 4, and use three volumetric MDCT data sets to develop an image-based breathing lung model, which accounts for nonlinear deforming airway geometry and time-varying boundary condition during breathing

Chapter 6 summarizes this thesis and discusses some interesting topics for future work.

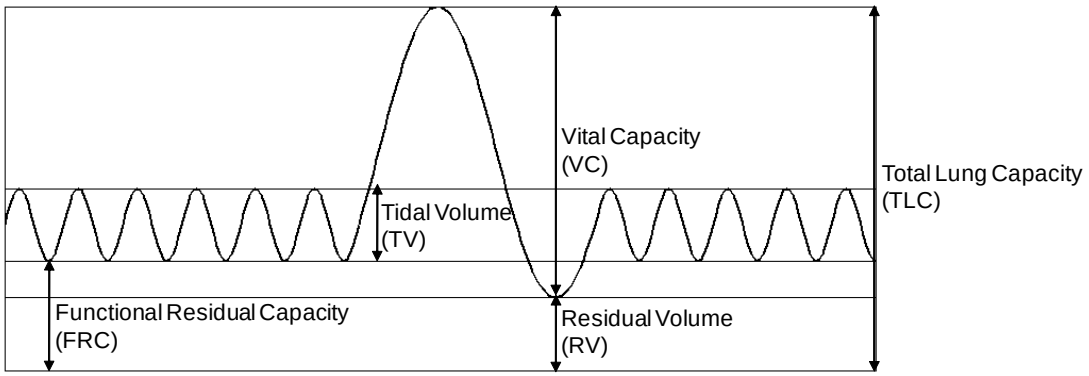

Figure 1.1: Definition of lung volumes and capacities.

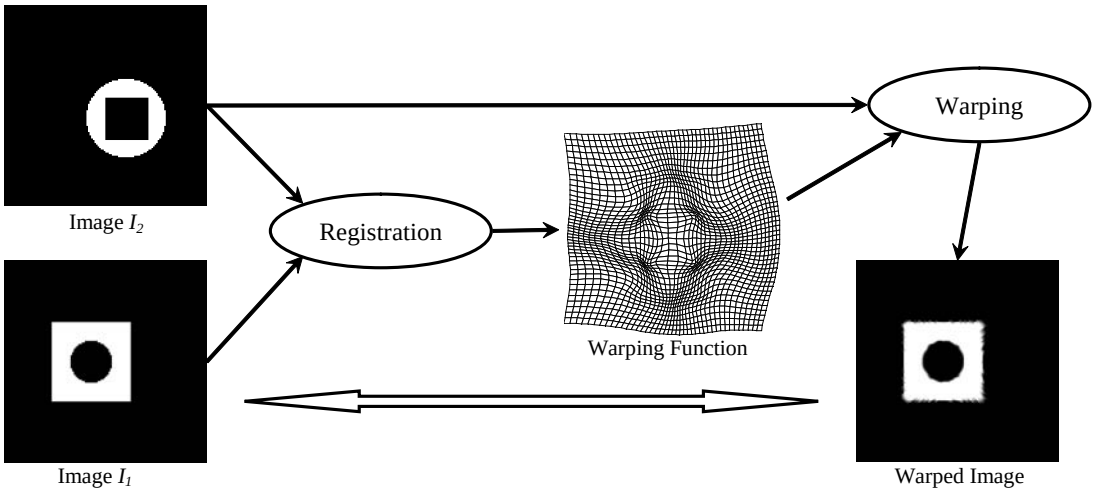

Figure 1.2: A two-dimensional (2D) illustration of nonrigid image registration. An image with a square outer boundary and a circular inner boundary is mapped to the one with a circular outer boundary and a square inner boundary. The centers of objects are also shifted. It is noted that the warping function is defined in the domain of the image I_1 from a Lagrangian viewpoint while the warped image is obtained by transforming the image I_2 to the domain of image I_1 from an Eulerian viewpoint.

CHAPTER 2
MASS PRESERVING NONRIGID REGISTRATION

2.1 Introduction

Registrations of lung data sets have been applied in establishing lung atlases [59], segmenting lungs with pathology [97], linking four-dimensional lung data sets [87] and tracking motion of lung tissues [15, 32, 79]. There is an important additional motivation to register data sets acquired in one study whereby the subject is imaged at full inspiration (total lung capacity, TLC) and at end expiration (functional residual capacity, FRC, or residual volume, RV). TLC provides detailed information related to airway and parenchyma structure while FRC or RV provides information related to air trapping.

A registration algorithm usually consists of three main components: a transformation model, a similarity measure, and an optimization step [19]. The transformation model specifies the spatial mapping of corresponding points between two images. The similarity measure defines how well those two images match and it provides a quantitative criterion for an optimization step to optimize the parameters of a transformation model. Since lung motion varies from apex to base and ventral to dorsal, it is desirable to use nonrigid image registration to capture non-uniform deformation. However, two main issues make nonrigid registration of lung MDCT images become challenging: (1) changes in voxel intensity due to inflation, and (2) large deformation between the two images to be registered, such as a FRC-TLC registration pair.

A common similarity measure used in registrations of MDCT lung images is the sum of squared intensity differences (SSD) [15, 59–61, 79, 87, 88, 93]. The

assumption of SSD is that corresponding points in both images have the same intensity. The assumption is also implied in registration using optical flow, another common method used to register lung images [24, 32, 33, 111, 127]. However, this assumption is not valid for the MDCT lung image which voxel intensity changes due to changes in densities associated with inflation. Although some similarity measures, such as normalized correlation [78, 91] and mutual information (MI) [18, 100], used for lung image registrations are insensitive to changes in voxel intensity, they are based on global statistical models of the intensity relationships between voxels in the two images and may not be appropriate to capture the non-uniform contraction / expansion of the lungs since changes in voxel intensity vary from apex to base and ventral to dorsal. Recently, Sarrut et al. [87] proposed a priori step to take into account changes in voxel intensity by artificially adjusting voxel intensity in one image according to the intensity in the other. Although it is only a preprocessing step, their results show improved registration results. This work also suggested the importance of taking into account such intensity changes when registering MDCT lung images.

Large deformation between two images to be registered also makes the problem challenging since it is more difficult to ensure local invertibility of the mapping. However, local invertibility is essential for biologically meaningful mapping and is especially important in our cases where the resulting deformation field is further used to deform the airway geometry for CFD simulation. One way to ensure local invertibility is to control the positivity of Jacobian values on the whole image domain [12, 16, 92]. Jacobian values reflect local contraction or expansion of a deformation field. A Jacobian value of one corresponds to no expansion or contraction. It is greater than one if there is local expansion and less than one if there is local

contraction. It is negative if local folding of the deformation exists.

In this chapter, we propose a mass-preserving nonrigid image registration method to align two MDCT lung data sets acquired during breath-hold at two different lung volumes in the same scanning session or over short periods of time. The performance of the new similarity measure is evaluated using six pairs of MDCT volumetric data sets acquired near TLC and FRC.

2.2 Methods

Given two images I_f and I_r, referred to as the floating and reference images, the goal of the registration is to determine a spatial warping function that can match the two images. We assume that $I_f(\mathbf{x})$ and $I_r(\mathbf{x})$ are continuous functions of intensity values at the position at the position $\mathbf{x}$ ($\mathbf{x} = (x, y, z)$) for the floating and reference images, respectively.

2.2.1 Transformation Model

One of the most common transformation models is cubic B-spline [54, 85, 113]. Compared with other spline-based transformation models, such as thin-plate spline [5, 83] or elastic-body spline [20, 123], B-spline is locally controlled. Each point in the N-dimensional space is only influenced by the corresponding ND grid consisting of 4^N control nodes. For example, a point is influenced by its 4×4 surrounding control nodes in 2D and by its $4 \times 4 \times 4$ surrounding control nodes in 3D. This advantage makes it computationally efficient even when a large number of control nodes are used.

Let Φ denote a $n_x \times n_y \times n_z$ uniform grid with $\phi_{i,j,k}$ as the displacement of the ijkth control node. The spacings between the control grids in x, y and z directions

are denoted by δ_x, δ_y and δ_z, respectively. The transformation function $T(\mathbf{x};\phi)$ is defined in terms of control nodes as

$$T(\mathbf{x};\phi) = \mathbf{x} + \sum_{l=0}^{3}\sum_{m=0}^{3}\sum_{n=0}^{3} B_l(u)B_m(v)B_n(w)\phi_{i+l,j+m,k+n}, \tag{2.1}$$

where $i = \lfloor x/\delta_x \rfloor - 1$, $j = \lfloor y/\delta_y \rfloor - 1$, $k = \lfloor z/\delta_z \rfloor - 1$, $u = x/\delta_x - (i+1)$, $v = y/\delta_y - (j+1)$, and $w = z/\delta_z - (k+1)$. Functions B_0 through B_3 are basis functions of cubic B-spline and are defined as follows:

$$\begin{aligned} B_0(t) &= \left(-t^3 + 3t^2 - 3t + 1\right)/6 \\ B_1(t) &= \left(3t^3 - 6t^2 + 4\right)/6 \\ B_2(t) &= \left(-3t^3 + 3t^2 + 3t + 1\right)/6 \\ B_3(t) &= t^3/6, \end{aligned} \tag{2.2}$$

where $0 \leq t < 1$. These basis functions have two important mathematical properties. First, they have a limited support, which allows efficient computation of the transformation function. Second, they are C^2 continuous, which allows the analytical computation of first-order derivatives of the transformation function. The second property ensures efficient computation and minimization of the new similarity measure described below, which is based on the first-order derivatives.

Since displacements of control nodes act as parameters of the transformation function, the ability of B-spline to capture deformations depends on the resolution of the control grid. A coarse control grid allows for modeling global deformations, while a fine control grid allows for modeling highly local deformations.

The basic algorithm described above may result in a noninvertible transformation, which causes parts of the image are folded upon nearby parts and further leads to failure of CFD simulation due to changes of topology. Several algorithms

have been proposed to ensure local invertibility of cubic-spline by controlling the positivity of the Jacobian values [12, 16, 92], among which Choi and Lee [12] proposed an easy-to-implement sufficient injective condition for both 2D and 3D cases. According to their analysis, a transformation function is locally injective over the entire continuous domain if the displacement of each control node is bounded by $\mathbf{h}/K$, where K is a constant and it is approximately 2.046392675 for the 2D case and 2.479472335 for the 3D case. With this condition, a point can be deformed at most by $\mathbf{h}/K$ if and only if all 4×4 (for 2D) or $4 \times 4 \times 4$ (for 3D) surrounding control nodes are displaced by $\mathbf{h}/K$. From this view, a control grid with large spacing is required to model large global deformations for a TLC-FRC registration pair. However, as we discussed above, a fine control grid is required to capture the highly local deformation. To overcome the conflicting requirements of coarse and fine control grids for global and local deformations, respectively, a multi-level B-spline technique [57, 84] is adopted in this work.

In the multi-level B-spline algorithm, a hierarchy of control grids, $\Phi_0, \Phi_1, \ldots, \Phi_n$, is used to derive a sequence of transformations with a single level B-spline manipulation defined above. The algorithm starts with the coarsest control grid Φ_0. A smooth and invertible transformation can be obtained with the displacement constraints. This transformation has the ability to capture the global deformation. The local deformation is progressively handled by the subsequent transformations with finer control grids. The final transformation is defined as a composite operation

$$\mathcal{T} = T_n \circ T_{n-1} \circ \ldots \circ T_0. \tag{2.3}$$

where $T_0, T_1, \ldots, T_n$ are the sequence of transformations.

To implement the composite operation, we introduce a warping image ϖ,

which is a discretized version of the transformation function. The value of each voxel is equal to the physical coordinates of the transformed point of that voxel. Given a voxel $\mathbf{p}$ and its corresponding physical coordinates $\mathbf{x}_0$, the value at $\mathbf{p}$ in the warping image is initially equal to $\mathbf{x}_0$ and then sequentially equal to the transformed point of $\mathbf{x}_0$ after the sequence of transformations. Thus, the composite operation is simplified as a recursive algorithm: $\varpi \leftarrow T_i(\varpi)$.

Since the composite operation will not change the property of diffeomorphism, we can get a final invertible transformation by imposing the sufficient injective condition for each B-spline level. Namely, local invertibility for the large deformation is guaranteed by the combination of the displacement constraints and the multi-level B-spline technique.

2.2.2 Similarity Measure

In order to take into account changes in voxel intensity due to inflation, we introduce the sum of squared tissue volume difference (SSTVD) as the similarity measure. In contrast to previous similarity criteria, SSTVD is based on quantitative MDCT analysis defined in Eq. (1.2) and aims to minimize the local tissue volume difference within lungs between matched regions. Its definition is as follows:

$$E = \sum_{\mathbf{x}\in\Omega} \left[V_f\left(\mathcal{T}(\mathbf{x};\phi)\right) \gamma_{\mathrm{tiss}\,f}\left(\mathcal{T}(\mathbf{x};\phi)\right) - V_r\left(\mathbf{x}\right) \gamma_{\mathrm{tiss}_r}\left(\mathbf{x}\right) \right]^2 \tag{2.4}$$

where V_r and V_f are total volumes of corresponding regions in the two images, respectively. Ω denotes the overlap lung regions between the two images.

This new similarity measure is based on the assumption that the tissue (blood plus parenchyma) volume of the lungs is preserved during respiration/static lung

volume changes. We recognize that the tissue volume changes slightly due to pulmonary blood volume changes with lung inflation, but this assumption we make have proven reasonable since volume change of "tissue" is small and such changes are much smaller than those of air (See Table 2.1 for changes in tissue and air volumes between TLC and FRC for all six registration pairs used in this work). In addition, the assumption used here has been successfully used in estimating regional specific volume [29] and linking four-dimensional lung data sets [87]. Although changes of "tissue" volume due to blood volume changes are taken into consideration by a correction step [32], such small change appears to be of minimal consequence to our registration process, taking into account the considerable improvement shown in registrations using our new method.

It is noted that $\mathcal{T}$ is used in Eq. (2.4) since the multi-level B-spline technique is adopted. Given a transformation level i, $\mathcal{T}(\mathbf{x};\phi)$ is a compound function defined by

$$\mathcal{T}(\mathbf{x};\phi) = T_i\left(\varpi(\mathbf{x});\phi\right), \tag{2.5}$$

where $T_i\left(\mathbf{x};\phi\right)$ is the warping function at the current level and $\varpi(\mathbf{x})$ is the warping image obtained at the previous level.

Given a warping function $\mathcal{T}(\mathbf{x};\phi)$, $I_f(\mathcal{T}(\mathbf{x}))$ can be interpolated from the floating image to further estimate tissue fraction $\gamma_{\text{tiss}f}\left(\mathcal{T}(\mathbf{x};\phi)\right)$ and $V_f\left(\mathcal{T}(\mathbf{x};\phi)\right)$ can be calculated from the Jacobian value J_T of the deformation as $V_f = J_T V_r$. Thus, the final form of the new similarity measure reads

$$E = \sum_{\mathbf{x}\in\Omega} \left\{ V_r\left(\mathbf{x}\right) \left[J_T(\mathbf{x};\phi)\gamma_{\text{tiss}f}\left(\mathcal{T}(\mathbf{x};\phi)\right) - \gamma_{\text{tiss}r}\left(\mathbf{x}\right) \right] \right\}^2. \tag{2.6}$$

Calculation of the gradient of the cost function is necessary for its efficient

and robust minimization. For a given transformation parameter ϕ, the gradient of cost function is calculated by

$$\frac{\partial E}{\partial \phi} = 2\sum_{\mathbf{x}\in\Omega} V_r^2(\mathbf{x}) \left[J_T(\mathbf{x};\phi)\gamma_{\text{tiss}_f}\left(\mathcal{T}(\mathbf{x};\phi)\right) - \gamma_{\text{tiss}_r}(\mathbf{x}) \right] \frac{\partial \zeta}{\partial \phi} \tag{2.7}$$

$$\text{with} \quad \frac{\partial \zeta}{\partial \phi} = \gamma_{\text{tiss}_f}\left(\mathcal{T}(\mathbf{x};\phi)\right) \frac{\partial J_T(\mathbf{x};\phi)}{\partial \phi} + \frac{J_T(\mathbf{x};\phi)}{\text{HU}_{\text{tiss}} - \text{HU}_{\text{air}}} \frac{\partial I_f\left(\mathcal{T}(\mathbf{x};\phi)\right)}{\partial \mathcal{T}} \frac{\partial \mathcal{T}(\mathbf{x};\phi)}{\partial \phi}$$

where $\partial I_f / \partial \mathcal{T}$ is the intensity gradient of the floating image.

Jacobian value J_T is defined as the determinant of derivative matrix of the deformation. From Eq. (2.5), we can obtain

$$J_T = \det(\mathbf{D}) = \det(\mathbf{D^T})\det(\mathbf{D}^{\varpi}), \tag{2.8}$$

with

$$\mathbf{D}^T = \begin{pmatrix} \frac{\partial T_{ix}}{\partial x} & \frac{\partial T_{ix}}{\partial y} & \frac{\partial T_{ix}}{\partial z} \\ \frac{\partial T_{iy}}{\partial x} & \frac{\partial T_{iy}}{\partial y} & \frac{\partial T_{iy}}{\partial z} \\ \frac{\partial T_{iz}}{\partial x} & \frac{\partial T_{iz}}{\partial y} & \frac{\partial T_{iz}}{\partial z} \end{pmatrix} \text{ and } \mathbf{D}^{\varpi} = \begin{pmatrix} \frac{\partial \varpi_x}{\partial x} & \frac{\partial \varpi_x}{\partial y} & \frac{\partial \varpi_x}{\partial z} \\ \frac{\partial \varpi_y}{\partial x} & \frac{\partial \varpi_y}{\partial y} & \frac{\partial \varpi_y}{\partial z} \\ \frac{\partial \varpi_z}{\partial x} & \frac{\partial \varpi_z}{\partial y} & \frac{\partial \varpi_z}{\partial z} \end{pmatrix}. \tag{2.9}$$

The derivatives of ϖ at a voxel can be derived from its neighbors by using central-difference approximation. For example, $\partial \varpi_x / \partial x = (\varpi_x^+ - \varpi_x^-)/(2\Delta x)$, where superscripts $+$ and $-$ denote the two neighbors of the current voxel in the x direction and Δx is the spacing of the warping image in that direction. In addition, since the cubic B-spline transform is the tensor product of independent one-dimensional functions, the entries of $\mathbf{D}^T$ can be analytically calculated. For example, derivative of its x-component with respect to x is given as

$$\frac{\partial T_{ix}(\mathbf{x};\phi)}{\partial x} = 1 + \frac{1}{\delta_x} \sum_{l=0}^{3} \sum_{m=0}^{3} \sum_{n=0}^{3} \frac{dB_l(u)}{du} B_m(v) B_n(w) \phi_{i+l,j+m,k+n}. \tag{2.10}$$

The remaining derivatives have an analogous form. Computation of these

derivatives is very similar to computing T_i itself with differences that basic functions $B_{0,1,2,3}$ are replaced by their respective derivatives, which are computed as follows:

$$\begin{aligned} dB_0(t)/dt &= \left(-t^2+2t-1\right)/2 \\ dB_1(t)/dt &= \left(3t^2-4t\right)/2 \\ dB_2(t)/dt &= \left(-3t^2+2t+1\right)/2 \\ dB_3(t)/dt &= t^2/2. \end{aligned} \tag{2.11}$$

The last terms to discuss are derivatives of both the transformation function and the Jacobian value with respect to transformation parameters in Eq. (2.7): $\partial\mathcal{T}/\partial\phi$ and $\partial J/\partial\phi$. Since ϖ is not a function of ϕ at the current level, both terms are only contributed by T_i. Eqs. (2.1), (2.9) and (2.10) show that $\mathcal{T}$ and J_T have a linear relationship with ϕ. Thus, it is straightforward to compute those two terms: $\partial\mathcal{T}/\partial\phi$ and $\partial J_T/\partial\phi$.

2.2.3 Optimization

An efficient and robust optimization algorithm is required to minimize the cost function by adjusting transformation parameters. A limited-memory, quasi-Newton minimization method with bounds on the variables (L-BFGS-B) [6] is adopted considering its two advantages. First, it is well suited to handle the high dimensionality of parameter space. Second, it allows bound constraints on the independent variables, making it easy to implement the displacement constraints for a one-to-one mapping discussed in Sec. 2.2.1.

Multi-resolution strategy helps to improve the computational efficiency and to avoid some local minima. In addition to hierarchical transformation models, multi-resolution strategy is also used on images. A pair of image pyramids is built with

sequences of gradually reduced resolution images for both the floating and reference images. Here, we use three different levels in both the image pyramids and the hierarchy transformation models. The whole registration is composed of six levels and starts with the coarsest versions of both images and control grid. The images and control grids are then alternatively refined until the finest versions. On each level, optimization is used to minimize the cost function and the displacement constraint is imposed to ensure a one-to-one mapping. The warping image is calculated once the convergence criterion is reached. The warping image is then propagated to the next finer level and is used as a starting transformation at that level. It is noted that up-sampling of the warping image is required if the image resolution level changes. The basic idea of the multi-resolution strategy is illustrated in Figure 2.1.

2.2.4 Summary

In summary, the whole registration procedure is illustrated in Figure 2.2. First, an undeformed warping function is given to calculate an initial cost function between the reference and floating images I_r and I_f with SSTVD. This cost function is then minimized by adjusting displacements of control nodes of the B-spline to get a new warping function. With the new warping function, we can obtain a new warped image and update the cost function. This cycle repeats until the convergence criterion is reached.

2.3 Experiments And Results

2.3.1 MDCT Image Data

Data sets from six normal human subjects were used in this study to evaluate the performance of the proposed similarity measure. The subjects were examined

under a protocol approved by the University of Iowa's Institutional Review Board. Two volumetric scans were acquired with a Siemens Sensation 64 MDCT scanner (Forchheim, Germany) during breath-holds near FRC and TLC in the same scanning session for each subject. Each volumetric data set contains $550 - 760$ image sections with a section spacing from $0.5 - 0.7mm$ and a reconstruction matrix of 512×512 pixels. In-plane pixel spatial resolution is approximately $0.6 \times 0.6mm$. For each data set, automatic lung segmentation is performed using the algorithm in [44]. Experimental studies using human MDCT lung images have shown that this segmentation algorithm can accurately extract the lung with a root mean square difference between the computer and human analysis of 0.8 voxels and the computational time is $2 - 3$ minute on a PC workstation with 300Mhz [44]. Once the lung is extracted, we can estimate the total lung volume, tissue volume and air volume, among which total lung volume is the sum of voxel volumes in the lungs, tissue and air volume can be estimated from HU using Eq. (1.2). Table 2.1 lists these volumes for all data sets. We can find that changes in tissue volume between TLC and FRC are small for all six registration pairs with an average percentage change of 3.5%. Thus, it is reasonable to assume that the tissue volume is preserved.

2.3.2 Experimental Setup

Given a registration pair, the data set with the smaller lung volume is taken as the floating image and the one with the larger lung volume is the reference image. Both reference and floating images are first down-sampled by a factor of 2 in each dimension, so 8 times less voxels, in order to reduce the computational time. The down-sampled images are then registered in the multi-resolution framework shown in Figure 2.1. Once the registration is done, the warped image is up-sampled so

that it has the same size as the reference image.

In order to evaluate the new similarity measure, we perform registrations with both SSD and SSTVD for comparison. The cost function for the SSTVD method is evaluated by Eq. (2.4), whereas for the SSD method it is computed by

$$E_{SSD}(\phi) = \sum_{\mathbf{x}\in\Omega} \left[I_r(\mathbf{x}) - I_f\left(\mathcal{T}(\mathbf{x})\right)\right]^2 . \tag{2.12}$$

Lung segmentations of reference and floating images are used as masks for both methods. The mask of the floating image is then dilated by 5×5 voxels in order to improve the matching at lung boundaries. The potential influence of the segmentation on registration results is not yet to be investigated. However, we expect that the influence might be small by considering the accuracy of segmentation as discussed previously and that the lung boundary has an obvious contrast with high value of tissue volume for the body and low value inside the lung.

2.3.3 Results

Landmarks located at vessel bifurcations are used to evaluate registration accuracy. A semi-automatic landmark annotating system [75] was used to guide the observer to generate the corresponding landmarks in TLC and FRC images. Each registration pair has $120 - 210$ landmarks and approximately $20 - 40$ are located in each lobe. Figure 2.3 shows an example of the landmark locations.

A linear mixed model analysis was used to compare mean landmark error of the SSTVD method with the SSD method and further with the MI method (see the description in the last paragraph in this section). The fixed effects of the model were method (SSTVD, SSD and MI), initial distance d_0 ($d_0 < 20mm$, $20 \leq d_0 < 40mm$, $40 \leq d_0 < 60mm$, $d_0 \geq 60mm$), and method×distance interaction, with subject

as the random effect. To satisfy the assumption of normal distribution for the dependent variable, the natural log transformation was applied to landmark error to normalize the data distribution.

The test of fixed effects from the fitted model shows a significant method×distance interaction (p-value=0.006) which indicates that the mean difference in landmark error between methods varies with initial distance. Thus, pairwise comparison of the SSTVD method with the SSD method and with the MI method was done at each distance interval. The tests for these pairwise comparisons were performed using test of mean contrast based on parameter estimates from the fitted model. Since multiple tests were performed, the p-values for the pairwise comparisons were adjusted using Bonferroni's method to account for the number of tests performed (which are 8 tests, 2 pairwise comparisons at 4 distances). The estimate of the mean landmark error for each method computed from the fitted linear mixed model and the mean ratio are shown in Table 2.2. Landmark error for the SSTVD method compared to the SSD method is on average $69\% + 13\%$ smaller at initial distances of $d_0 < 20mm$ and $74\% + 11\%$ smaller at $20 \leq d_0 < 40mm$. Significantly smaller landmark error for the SSTVD method compared to the SSD method was observed at $40 \leq s < 60mm$ and $d_0 \geq 60mm$, with the SSTVD method error being smaller by $83\% + 7\%$ and $85\% + 8\%$, respectively.

Figure 2.4 shows an example of the distribution of landmark distances along the z-axis (from apex to base) before and after registrations using both the SSTVD method and the SSD method. The initial landmark distance increases as landmarks are closer to the base, see Figure 2.4(a), since the deformation of the lung is mainly driven by the diaphragm. However, with the SSTVD method, the landmark distances decrease and all landmarks have an approximately uniform error distribution

from apex to base in Figure 2.4(b). This means that the SSTVD method shows good registration for both small and large deformations within the same lung independent of lung location. Also note in Figure 2.4(b) that the landmarks have a large deviation of errors for the SSD method.

Figures 2.5 (a) and (b) show surface distance maps of the warped TLC major vessel tree to the FRC major vessel tree for the SSTVD method and the SSD methods, respectively. The FRC major vessel tree is also shown in white for reference. The warped TLC major vessel tree is obtained by applying the transformation to the surface mesh of the TLC tree. Vessel trees at both TLC and FRC images are automatically extracted by using the algorithm in [94] implemented in the Pulmonary Workstation (VIDA Diagnostics, Coralville, Iowa). The major vessel trees are then obtained by applying morphology opening with a structure element of $3 \times 3 \times 3$ voxels followed by a connected component process on the segmented vessel trees to remove small branches. Figure 2.5(a) demonstrates that the surface distances are less than $2mm$ for the SSTVD method. Large distances of some segments are possibly due to the inconsistent tree structure between TLC and FRC caused by segmentation or morphology operation steps. Examples are marked as A and B in Figure 2.5(a), which show cases with missing segments in the FRC major trees. In contrast with the SSTVD, the SSD method yields an obvious mis-match in several regions, marked as C, D, and E in Figure 2.5(b). One can see that the white unwarped segments mis-align with the color coded tree in these regions.

Figures 2.6 and 2.7 show a slice from registration pairs A and F, respectively. These two registration pairs are chosen because one has the smallest lung volume difference and the other has the largest (see Table 2.1) among all registration pairs tested here. In each figure, the slice from the reference image is shown in (a), the

corresponding slice from the warped image obtained from the SSTVD method is shown in (b) and the corresponding slice from the warped image obtained from the SSD method is shown in (c). Although both methods yield a good alignment of the overall shapes of lungs, it can be seen that the SSTVD approach improves the alignment of structures within the lungs, such as the vessels and fissures.

The proposed SSTVD similarity measure is further compared with MI using the same statistical method described earlier for the SSTVD vs. SSD comparison. For MI, we used a publicly available registration package elastix [50]. The optimal parameters specified in elastix include five levels of resolution for both the images and the transformation, a stochastic gradient descent optimization method [51] using a decaying function of the iteration number $k : a_k = a/(A + K)^{\alpha}$ with user-defined constants $A = 50$ and $\alpha = 0.6$. a was set to 50000.0, 30000.0, 10000.0, 10000.0 and 5000.0 for the five resolutions. The statistical comparisons of landmark errors between the SSTVD method and the MI method can be seen in Table 2.2. Mean landmark error does not differ between the two methods at initial distances of $d_0 < 20mm$, $20 \leq d_0 < 40mm$ and $40 \leq d_0 < 60mm$. At initial distances of $d_0 \geq 60mm$, mean landmark error for the SSTVD method is $77\% + 8\%$ smaller than the MI method (p-value=0.0002). This is consistent with our hypothesis that the SSTVD provides registration improvements for large deformations such as occur when comparing TLC and FRC image data sets as done in this study.

2.4 Discussion

In this chapter, we have presented a nonrigid image registration method to align two MDCT lung data sets acquired during breath-holds at different lung volumes. Our method is of particular use when the volume differences between the two

image sets are large as demonstrated in Table 2.2, utilizing TLC and FRC scans. In order to take into consideration changes in voxel intensity of lungs with inflation, we introduced the sum of squared tissue volume difference as the similarity criterion. This new criterion aims to minimize the local tissue volume difference within the lungs between matched regions. The local tissue volume difference is contributed by two factors: change in regional volume due to deformation and change in the fractional tissue content within a region due to respiration. The change in regional volume is calculated from the Jacobian value of the deformation and the change in the fractional tissue content is estimated from HU. A composite of multi-level B-spline transformations is adopted and a sufficient condition is imposed to ensure a one-to-one transformation, even for a pair of data sets with large volume differences.

To evaluate the effectiveness of the new similarity measure, we performed registrations for six lung volumetric pairs which were acquired at near TLC and FRC in the same scanning session. Over 100 landmarks located at vessel bifurcations were generated for each registration pair and the results show that the SSTVD method yields smaller average landmark errors than the SSD method. In addition, visual inspection shows that the SSTVD approach improves the alignment of structures within the lungs although both the SSD and SSTVD methods give a good alignment of the overall shapes of lungs.

Recently, Gorbunova et al. [30] independently proposed a similar similarity criterion as our SSTVD to monitor disease progression in longitudinal image studies where volume differences are smaller than those used here and, with pathology progression, tissue densities can undergo considerable changes. Different from their work, we seek to apply this approach to match multiple lung volumes acquired between TLC and FRC in the same scanning session or over short periods of time

with one goal trying to apply to CFD studies with moving lung boundaries [64, 65]. The registrations are performed to match those data sets to adjust the geometry of airways for changes in lung volumes and to estimate the boundary condition by accounting for regional lung distensibility. In estimating the regional lung distensibility from a TLC-FRC registration pair, Yin et al. [129] demonstrated that the SSTVD method yields a much more physiologically-consistent ventilation map than that of SSD. In this work, all data sets were from a well calibrated scanner whereby imaged air is -1000HU and water is 0. However, the SSTVD can be extended to the cases when the scanner is out of calibration. Imaged air and tissue can be sampled in the center of the trachea (air) and aorta (blood). Assuming that HUs are linear between these ends of the scale, a voxel-by-voxel shift can be achieved. This is an important step as it is becoming well recognized that there are fairly significant variabilities between manufacturers in regards to HUs of reconstructed air within the thorax [38, 101].

Table 2.1: The total lung volume (TLV), air volume (AV) and tissue volume (TV) for all six registration pairs are estimated from HU.

Registration Pair	Volume	TLC (l)	FRC (l)	Difference (l)	Percentage Change | TLC-FRC | /TLC
	TLV	5.31	2.91	2.40	
A	AV	4.62	2.17	2.45	
	TV	0.69	0.74	-0.05	7.2%
	TLV	5.11	2.68	2.43	
B	AV	4.51	2.07	2.44	
	TV	0.60	0.61	-0.01	1.7%
	TLV	5.94	3.40	2.54	
C	AV	5.23	2.67	2.56	
	TV	0.71	0.73	-0.02	2.8%
	TLV	6.41	3.20	3.21	
D	AV	5.58	2.33	3.25	
	TV	0.83	0.87	-0.04	4.8%
	TLV	7.18	3.76	3.42	
E	AV	6.31	2.87	3.44	
	TV	0.87	0.89	-0.02	2.3%
	TLV	7.28	3.37	3.91	
F	AV	6.41	2.52	3.89	
	TV	0.87	0.85	0.02	2.3%
Overall					3.5%

$*$: The percentage change of tissue volume is also listed for reference. The unit for volumes is liter (l).

Table 2.2: Statistical comparison of landmark errors between the SSTVD method, the SSD method and the MI method for all six registration pairs.

d_0	SSTVD	SSD	MI	SSTVD vs. SSD		SSTVD vs. MI	
(mm)	(mm)	(mm)	(mm)	SSTVD/SSD	p-value[1]*	SSTVD/MI	p-value*
$d_0 < 20$	0.56 ± 0.04	1.84 ± 0.76	0.54 ± 0.07	0.31 ± 0.13	0.243	1.04 ± 0.15	>0.99
$20 \leq d_0 < 40$	0.76 ± 0.06	2.90 ± 1.20	0.70 ± 0.09	0.26 ± 0.11	0.151	1.08 ± 0.16	>0.99
$40 \leq d_0 < 60$	0.81 ± 0.07	4.66 ± 1.94	0.92 ± 0.12	0.17 ± 0.07	0.050	0.88 ± 0.14	>0.99
$d_0 \geq 60$	1.90 ± 0.39	12.47 ± 6.08	8.11 ± 2.06	0.15 ± 0.08	0.021	0.23 ± 0.08	0.0002

$*$: Bonferroni adjustment p-value

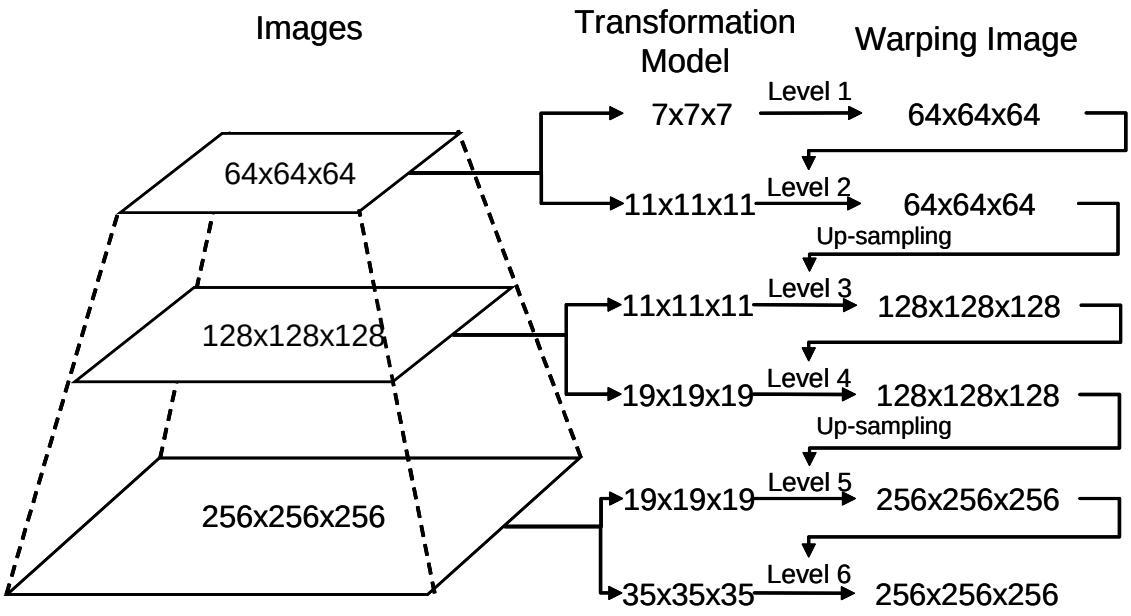

Figure 2.1: Framework of the multi-resolution strategy

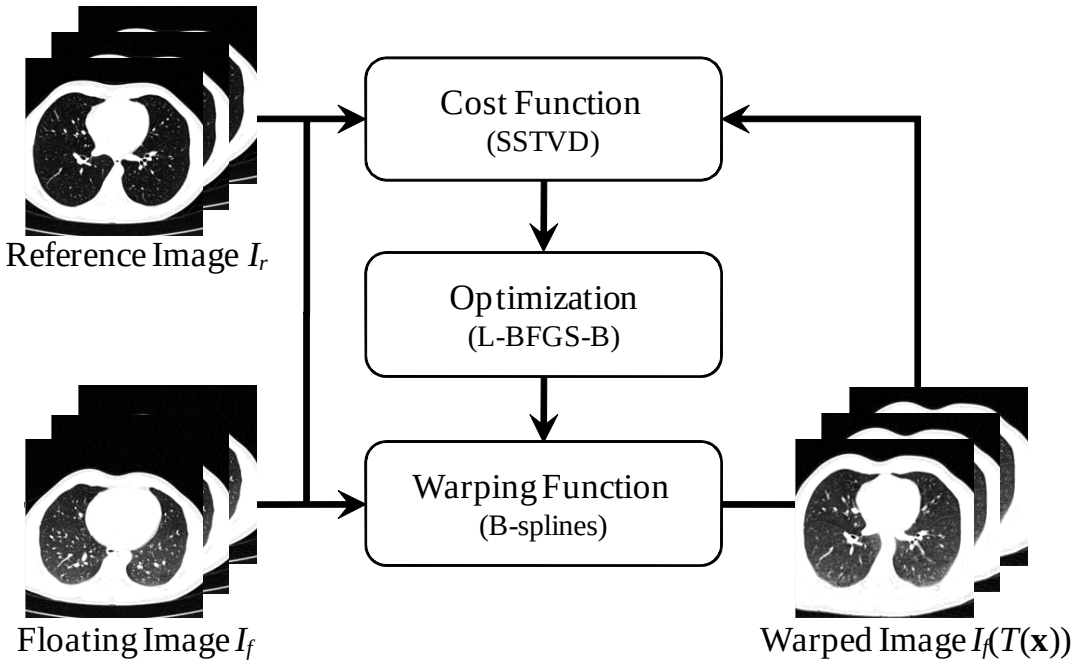

Figure 2.2: A sketch of the nonrigid registration procedure.

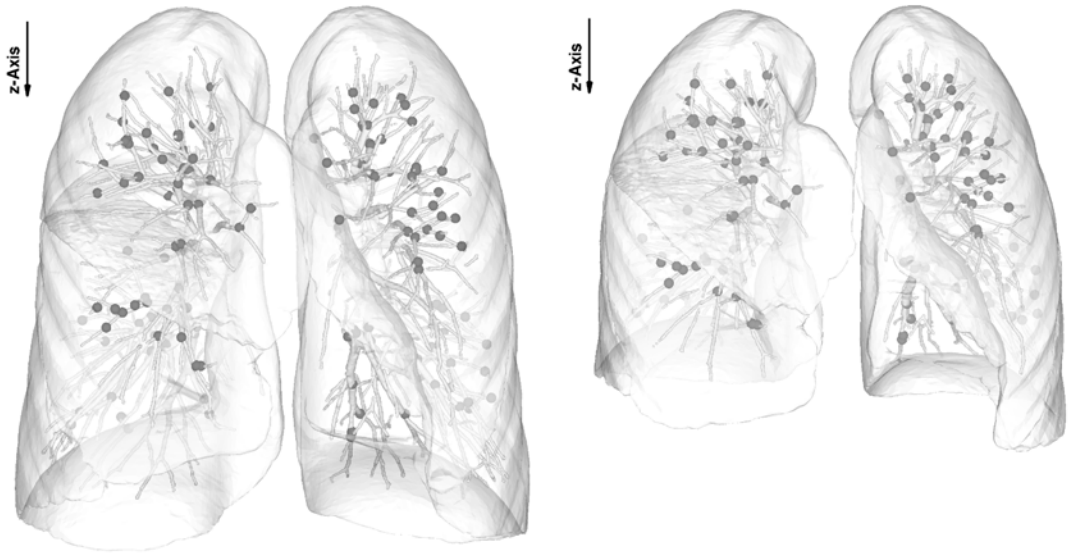

Figure 2.3: Locations of the landmarks (marked by spheres) at TLC (a) and FRC (b) for the registration pair A. Surface rendering of five lobes and major vessel branches is shown for reference.

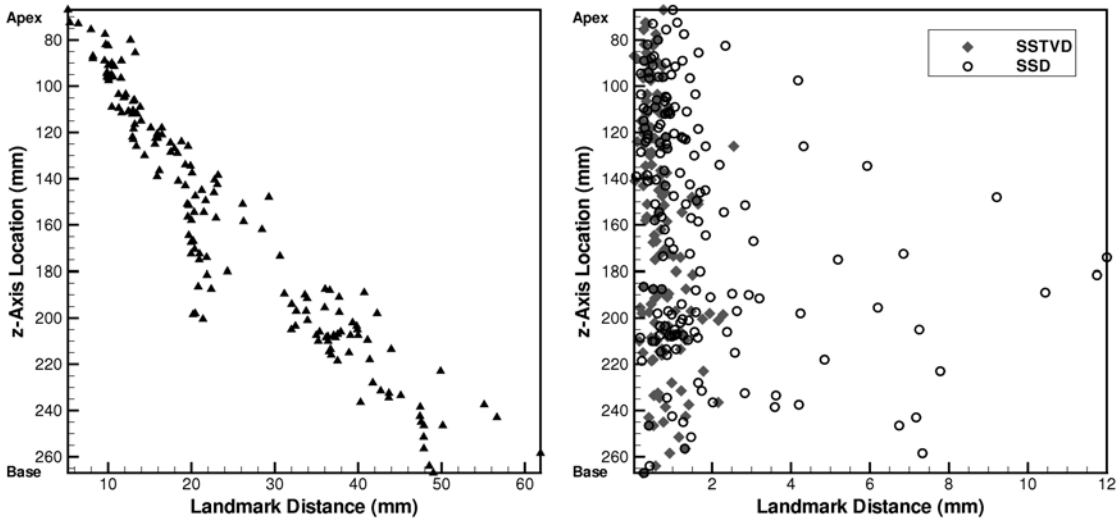

Figure 2.4: Distribution of landmark distance along the z-axis (from apex to base) before (a) and after registrations (b) using the SSTVD method (filled diamond) and the SSD method(unfilled circle) for the registration pair A. Note that all landmarks have an approximately uniform error distribution from apex to base for the SSTVD method while they have a large deviation of error for the SSD method in (b).

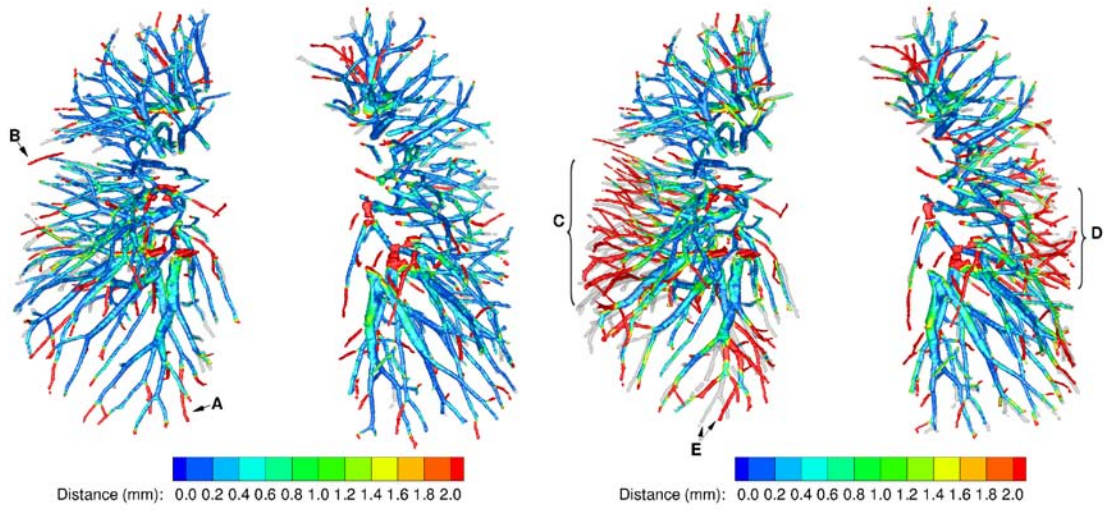

Figure 2.5: Surface distance maps of the warped TLC major vessel tree to the FRC major vessel tree for the SSTVD method (a) and the SSD method (b). The FRC major vessel tree is shown in white for reference. Note that the red segments in (a) are caused by missing segments in FRC major tree, not by mis-registration. Examples are marked as A and B. Segments with large errors in (b), marked as C,D,E, are due to clear mis-registration, as one can easily see that the white unwarped segments mis-align with the color coded tree.

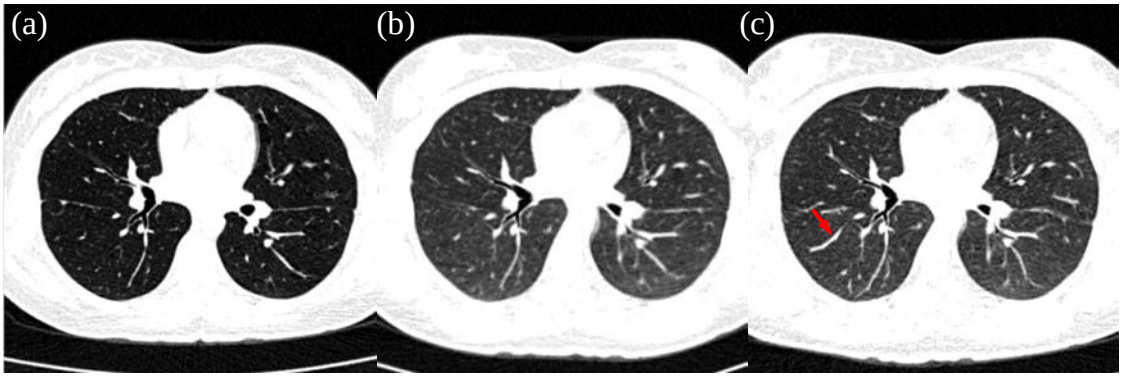

Figure 2.6: A slice from the registration pair A. (a) Slice from the reference image. (b) Corresponding slice from the warped image with the SSTVD method. (c) Corresponding slice from the warped image with the SSD method. Notice a mis-alignment of vessel trees indicated by the arrow for the SSD method in (c).

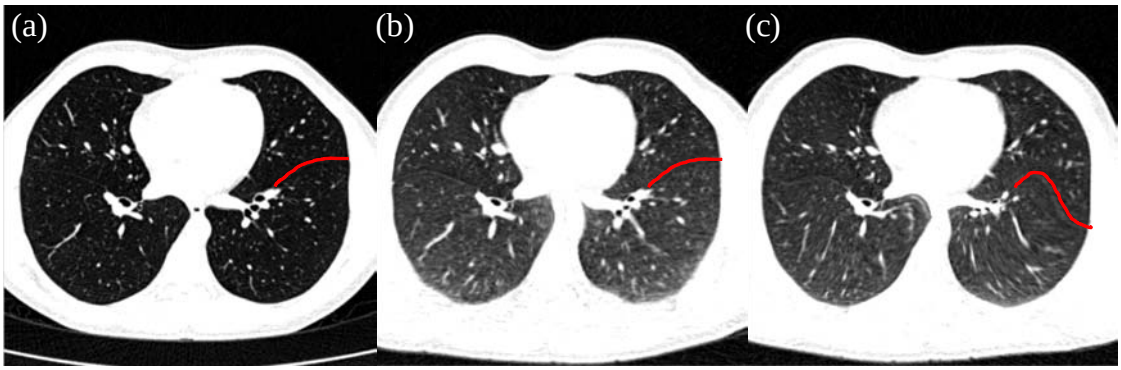

Figure 2.7: A slice from the registration pair F. (a) Slice from the reference image. (b) Corresponding slice from the warped image with the SSTVD method. (c) Corresponding slice from the warped image with the SSD method. Notice the good alignment between the lobar fissures (highlighted in lines) and between the vessel trees for the SSTVD method in (b) while an obvious mis-alignment of the fissure and vessels for the SSD method in (c).

CHAPTER 3
HYBRID IMAGE REGISTRATION FOR MOVING AIRWAY GEOMETRY

3.1 Introduction

Currently most of CFD studies have used rigid structures of airways though it is known that airways are compliant structures and can be deformed due to changes in lung volumes. Several factors could affect changes in dimensions of airway geometries, such as the mechanical properties, tethering force of the airway to the surrounding lung parenchyma and so on. Attempts have been made to account for deformation of airway geometry by using fluid-structure interaction (FSI) techniques [119, 125]. For example, Xia et al. [125] recently investigated the effects of airway-parenchymal tethering and airway wall motion on flow structure and wall shear stress with a realistic 3D CT-based airway bifurcation between the 3rd and 4th generations. Their finding shows that wall shear stress decreases by 80% when allowing wall compliance and can further decrease by 50% when allowing both the compliance and parenchymal tethering force. However, currently it is still challenging to develop a valid model for FSI-based analysis due to unclear material properties and complex airway-parenchyma interaction.

Alternatively, the registration-derived displacement field can be used to deform the CFD mesh for simulation of a breathing lung. Different from FSI-based simulation, the image-based CFD with deforming airway geometries is a one-way coupling analysis and, thus, requiring neither coupling with computational solid mechanics nor specifying tissue mechanical properties and tethering forces.

In this chapter, we aim to develop an image-based deforming airway model for

CFD simulations. In Chapter 2 we present a mass preserving registration method, which has been shown to be effective at matching intensity patterns of intra-subject data sets. However, such intensity-based registration approaches do not use anatomical knowledge. As a result, it may cause mismatch of important anatomical landmarks, such as airway bifurcations, when a registration falls into local minima. Thus, we further incorporate the landmark information at bifurcations of airway and vascular trees to improve the registration accuracy, especially the alignment of the airway trees. The proposed registration is then applied to build a dynamic airway model from a pair of lung volumetric images.

There are two main approaches to implement non-rigid registration for lung CT images according to similarity measures: feature-based approaches and intensity-based approaches. The feature-based approach uses corresponding anatomical features, mostly landmarks or surfaces, to define the transformation from one lung data set to the other [3, 9, 18, 27, 48]. In earlier landmark-based registration (LBR), several anatomical points, such as bifurcation points of airway and/or vascular trees, vertebra and so on, were manually selected by experts. Recent published work has shown the possibilities to generate large numbers of corresponding landmarks (more than 1,000) from a pair of lung CT data sets with semi-automatic tools [9, 75]. Several landmark-based registration algorithms have been proposed based on thin-plate spline (TPS) [45, 83] or elastic-body spline [20, 123] or moving least squares [9]. The use of B-spline was also proposed by [56] to compute a C^2 continuous and one-to-one mapping to warp 2D points. Alternatively, intensity-based registration (IBR) matches intensity patterns of the images by minimizing/maximizing a defined similarity measure. A representative though not exhaustive list of such studies can be found in [15, 22, 32, 79, 87, 91, 100, 102, 130]. Although both LBR and IBR have

been applied in registering lung images, they each have limitations. IBR matches intensity patterns over the whole image but does not use anatomical knowledge. As a result, it may cause mismatch of important anatomical landmarks, such as airway bifurcations, when a registration falls into local minima. Conversely, LBR uses anatomical landmarks. Those landmarks, however, are usually sparsely distributed throughout the images, leading to the mismatch of regions away from the landmarks. Thus, utilization of both anatomical landmark information and intensity patterns in image registration is desirable. In recent years, hybrid landmark- and intensity-based registration (LIBR) has been proposed to register lung images [59, 60, 78]. In most of these LIBR methods, a TPS model, which minimizes the bending energy of a thin plate for a smooth transformation between designated landmarks, is used to match landmarks. However, as pointed out by [42], the TPS transformation is a globally supported function so that it cannot accurately model localized deformation and it has high computational complexity when a large number of landmarks are used. More importantly, for large deformations a TPS model does not ensure local invertibility of the transformation, which is essential for biologically meaningful mapping and is especially important in our cases where the resulting deformation field is further used to deform the airway geometry for CFD simulation.

We propose a novel B-spline-based hybrid registration framework for lung CT datasets and apply it to build a dynamic lung airway model. The proposed hybrid registration is first evaluated using 2D artificial binary images and then applied in matching inspiration/expiration 3D CT human lung dataset pairs. The CFD simulation with moving airway geometry is then performed.

3.2 Methods

3.2.1 Hybrid Registration

3.2.1.1 Intensity-Based Registration

IBR matches intensity patterns by using mathematical or statistical criteria, also referred to as cost functions. The simplest cost function is the sum of squared intensity difference (SSD), which is defined as

$$E = \frac{1}{\Omega} \sum_{\mathbf{x} \in \Omega} \left[f_F \left(T(\mathbf{x}) \right) - f_R(\mathbf{x}) \right]^2, \tag{3.1}$$

The gradient of the cost function defined in (3.1) with respect to parameters of the transformation function is calculated by

$$\frac{\partial E}{\partial \phi_{\mathbf{i}_m}} = \frac{1}{\Omega} \sum_{\mathbf{x} \in \Omega} \frac{\partial e}{\partial f_F} \left. \frac{\partial f_F(\mathbf{z})}{\partial \mathbf{z}} \right|_{\mathbf{z}=T(\mathbf{x})} \frac{\partial T(\mathbf{x})}{\partial \phi_{\mathbf{i}_m}}, \tag{3.2}$$

where $\phi_{\mathbf{i}_m}$ denotes the mth component of the displacement vector at the ith node. $\partial e / \partial f_F = 2 \left[f_F \left(T(\mathbf{x}) \right) - f_R(\mathbf{x}) \right]$ and it reflects the current intensity errors between the corresponding points. The second term $\partial f_F(\mathbf{z}) / \partial \mathbf{z}$ is the intensity gradient of the floating image. The last term $\partial T(\mathbf{x}) / \partial \phi_{\mathbf{i}_m}$ is the derivative of the transformation function with respect to its parameters.

The assumption of the SSD is that corresponding points in both images have the same intensity. This assumption is valid for matching the binary image while is not suitable for matching pulmonary CT images since the voxel intensity changes within lungs due to inflation. A similarity measure SSTVD was recently proposed as an extension of the SSD to account for such intensity changes [129, 130]. In this work, the SSD is used for matching 2D artificial binary images while the SSTVD is used for matching 3D pulmonary CT images.

The SSTVD minimizes the local tissue volume differences between matched regions. Its expression is given as

$$E = \frac{1}{\Omega} \sum_{\mathbf{x} \in \Omega} \left[V_F \left(T(\mathbf{x}) \right) \tilde{f}_F \left(T(\mathbf{x}) \right) - V_R(\mathbf{x}) \tilde{f}_R(\mathbf{x}) \right]^2, \tag{3.3}$$

where V_R and V_F are total volumes of corresponding regions in the reference and floating images, respectively, and V_F can be calculated from the Jacobian value J as $V_F = JV_R$. It should be noted that the Jacobian value must be positive here, which can be ensured for the invertible transformation. In addition, $\tilde{f}$ is the tissue fraction estimated from the Hounsfield unit (HU) by $\tilde{f} = [f(\mathbf{x}) - HU_{air}]/[HU_{tissue} - HU_{air}]$, where HU_{air} and HU_{tissue} refer to the intensities of air and tissue, respectively [38]. Here, we assume that air is -1000HU and tissue is 55HU.

A limited-memory, quasi-Newton, bound constrained optimization method (L-BFGS-B) [6] is used as the optimization method to minimize the cost function. This optimization method has two main advantages. First, it is well suited for optimization with high dimensionality of parameter space. Second, it allows bound constraints on independent parameters, facilitating employment of displacement constraints for an invertible transformation.

3.2.1.2 Landmark-Based Registration

Let $P = \{\mathbf{p}\}$ and $Q = \{\mathbf{q}\}$ be a pair of corresponding ND landmark sets from the reference and floating images, respectively. The goal of LBR is to find a $\mathbb{R}^N \rightarrow \mathbb{R}^N$ mapping to match the corresponding landmarks.

Given an initial configuration of the B-spline control grid ϕ^0, the transformed point $\mathbf{p}'$ of a landmark point $\mathbf{p}$ can be calculated from Eq.(2.1) as $\mathbf{p}' = \mathbf{p} + \sum_{\mathbf{i} \in I_c} \phi^0_{\mathbf{i}} \beta_{\mathbf{i}}$, where $\mathcal{I}_c$ is a set of control nodes that can influence the point $\mathbf{p}$. $\beta_i = \prod_{k=1}^{N} B_k(t_k)$

is a ND tensor product of basis functions of cubic B-spline. In order to move the point p to its corresponding point q, the displacements of control nodes must satisfy that $\mathbf{q} = \mathbf{p} + \sum_{\mathbf{i} \in I_c} \phi_{\mathbf{i}} \beta_{\mathbf{i}}$. Thus, we can obtain

$$\Delta \mathbf{q} = \mathbf{q} - \mathbf{p}' = \sum_{\mathbf{i} \in \mathcal{I}_c} \Delta \phi_{\mathbf{i}} \beta_{\mathbf{i}}, \tag{3.4}$$

where $\Delta \phi_{\mathbf{i}} = \phi_{\mathbf{i}} - \phi_{\mathbf{i}}^0$ and it is the desired deviation of displacement at the control node $\mathbf{i}$ to transform the point $\mathbf{p}$ to its corresponding point $\mathbf{q}$. Among all possible solutions to Eq. (3.4), Lee et al. [56] chose the following one in the least-squared sense

$$\Delta \phi_{\mathbf{i}} = \frac{\beta_{\mathbf{i}} \Delta \mathbf{q}}{\sum_{\mathbf{i} \in \mathcal{I}_c} \beta_{\mathbf{i}}^2}. \tag{3.5}$$

For this solution, the control nodes close to point $\mathbf{p}$ have larger deviations than others since $\beta_{\mathbf{i}}$, which depends on the distance between the control node and $\mathbf{p}$, decreases as the distance increases.

When all points in the set P are independent (in other words, when they share no control nodes), the solution given in Eq. (3.5) can move each point in P to its specified position in Q. However, when multiple points in P are influenced by the same control node, the displacements of B-spline control nodes calculated for one point may mislead other points to other positions rather than the specified ones. Without loss of generality, we assume that P_s is a set of points in P which share a control node $\mathbf{i}$. Thus, the value of $\phi_{\mathbf{i}}$ can influence movements of all points in P_s. Given a point $\mathbf{p}_s$ in P_s, we can calculate $\Delta \phi_{\mathbf{i},s}$ by Eq. (3.5), where $\Delta \phi_{\mathbf{i},s}$ is the required displacement deviation to just move that single point to its specified position in Q. Since different points in P_s may result in different values of $\Delta \phi_{\mathbf{i},s}$, the final $\Delta \phi_{\mathbf{i}}$ can be chosen as a weighted average of all different $\Delta \phi_{\mathbf{i},s}$ by minimizing

$\sum_s \left(\beta_{\mathbf{i},s}\Delta\phi_{\mathbf{i}} - \beta_{\mathbf{i},s}\Delta\phi_{\mathbf{i},s}\right)^2$, thus obtaining

$$\Delta\phi_{\mathbf{i}} = \frac{\sum_s \beta_{\mathbf{i},s}^2 \Delta\phi_{\mathbf{i},s}}{\sum_s \beta_{\mathbf{i},s}^2}. \tag{3.6}$$

where the point close to the control node have larger influence than others since $\beta_{\mathbf{i},\mathbf{s}}$ decreases as the distance increases.

It is noted that the solution given by Eq. (3.6) becomes Eq. (3.5) if P_s consists of only one point. This means that Eq. (3.6) is suitable regardless of whether the points in P are independent. If we calculate the displacements of control nodes by Eq. (3.6), the resulting transformation cannot be guaranteed to be invertible. In order to get an invertible transformation, the displacements calculated by Eq. (3.6) must be truncated to satisfy that $\phi_{\mathbf{i}} \leq \mathbf{h}/K$. However, this limits the maximum displacement of each control node, leading to the problem that the above algorithm cannot always move points in P to their specified positions in Q. This problem can be overcome by the multi-level B-spline technique described in Section 2.2.1. The landmark matching is first solved at a coarse control grid. An invertible transformation can be obtained with the sufficient injective condition although the transformed points are not exactly deformed to the specified positions. The remaining deviations can be handled by subsequent deformations with finer control grids.

The LBR approach proposed here is combined with the IBR approach in a multi-resolution framework. The whole registration is composed of six levels and starts with the coarsest scales of both images and control grid. The images and control grids are then alternatively refined until the finest versions. On each level, LBR is first performed. The resulting transformation is then used as the starting point to guide IBR in which the transformation is refined based on matching the intensity patterns of the images. The transformation obtained from IBR is

then propagated to the next finer level and used as an initial transformation at that level. In order to ensure local invertibility, the displacement constraints are imposed during both LBR and IBR on each level. This is explicitly implemented by truncating the displacement of each control node during LBR while it is implicitly handled by the L-BFGS-B optimization method during IBR. The whole flow chart of the proposed hybrid method is given in Figure 3.1.

The transformation produced by LBR is used to guide IBR, which helps the latter to avoid some local minima. This manner is similar to other commonly used hybrid registration approaches [45, 59, 60, 78, 82]. However, owing to the consistent deformation models, in the current hybrid algorithm the additional overhead for the transition from LBR to IBR is negligible and, more importantly, it is easy to ensure the local invertibility of the transformation. In addition, the computational cost for the current LBR is low even when matching a large number of landmarks.

3.2.2 Dynamic Lung Model

Registration-derived warping function can also be used to derive airway geometry at an arbitrary phase by using an suitable interpolation technique. Currently we assume that voxel trajectories are straight lines and the intermediate deformation field is defined as [87]

$$\mathbf{d}_s(\mathbf{x}, t) = s(t)\mathbf{d}(\mathbf{x}), \tag{3.7}$$

where $\mathbf{d}(\mathbf{x})$ is the registration-derived displacement at the location $\mathbf{x}$ from the two CT images. $s(t)$ is a displacement coefficient and is correlated with the actual respiratory breathing curve (air flow) from the subject as monitored at the mouthpiece.

We recognize that non-straight-line displacement should not be neglected [4].

Future work is to seek a high-order interpolation technique for multiple lung volumes to account for non-straight-line displacement.

3.3 Results

The performance of the proposed hybrid algorithm is first evaluated on 2D artificial binary images in Section 3.3.1. The algorithm is then applied to match pairs of 3D CT lung data sets in Section 3.3.2. The SSD (Eq. (3.1)) is used for matching 2D artificial binary images with uniform intensity while the SSTVD (Eq. (3.3)) is used for matching 3D lung CT data sets with variable intensity.

3.3.1 Experiments With 2D Binary Images

The performance of current algorithm is evaluated by two pairs of 2D binary images. The goal is to demonstrate that the proposed LIBR algorithm has the ability to recover the large deformations of the images. The results are compared with those obtained by only LBR or IBR, seen in Figures 3.2 and 3.3. In addition, TPS-LIBR, where TPS algorithm is used to match the landmarks instead of B-spline, is also performed for comparison. Each binary image has a size of 128×128 pixels and a spatial resolution of 1×1 mm. The pixel value is set to be 255 for the object and 0 for the background. In Figures 3.2 and 3.3, column (a) shows the floating and reference images, where the landmarks are marked and labeled with the numbers showing the correspondence; columns (b)-(e) show the results obtained by LBR (b), IBR (c), LIBR (d) and TPS-LIBR (e), respectively. For each approach, the deformed image and the deformed grid are presented, where the deformed image is obtained by transforming the floating images from an Eulerian viewpoint while the deformed grid is obtained by deforming the regular grids from the reference image

domain to the floating image domain from a Lagrangian viewpoint. The enlarged views of the deformed grids are also presented to show the details in regions where large deformations occur.

In Figures 3.2 and 3.3, the objects being mapped are two squares or circles with the same center point and a staggered pattern of landmarks. The outer square or circle rotates clockwise by 45^o while the inner one rotates anticlockwise by 45^o. In other words, the desirable transformation should be a non-rigid rotation. First of all, we see that no folding occurs in any deformed grids from (b)-(d), demonstrating that the transformations are invertible for all LBR, IBR and LIBR. By contrast, folding occurs in the TPS-LIBR deformed grid, as shown in (e). In addition, we can see that LIBR not only yields a good alignment over the whole image, but also avoids some local minima because of utilization of both the intensity and landmark information. IBR yields better alignment over the whole image than LBR while IBR fails to recover the non-rigid rotation.

The performance of the proposed LIBR algorithm is further quantified in Table 3.1 by the landmark distance and metric value of SSD before and after registrations. The landmark distance is used to measure the agreement of the landmarks and the metric value of SSD is used as a measurement of agreement for intensity patterns.

In Table 3.1, the initial landmark distance (before registration) is calculated between the corresponding landmarks in the floating and reference images while the landmark distance after registrations is calculated between the actual landmark positions in the floating images and the registration-predicted positions. The initial SSD (before registration) is calculated between the floating and reference images and the SSD after registration is calculated between the deformed and reference

images. It is clear that LIBR yields low SSD values and small landmark mismatch errors compared with LBR and IBR. In addition, the minimum Jacobian values (J_{min}) are shown in Table 3.1 and they are positive for LBR, IBR and LIBR. The minimum Jacobian is negative for TPS-LIBR, further demonstrating that folding of the deformation field exists.

The results above demonstrate that the current LIBR algorithm has the ability to match both the intensity patterns and the designated landmarks. It also has the ability to generate an invertible transformation to recover large deformation. In addition to good performance, the computational cost is low. The total computational time on a single 3GHz processor is about 0.71 sec, shown in Table 3.1. The advantage of low computational cost becomes more obvious when a large number of landmarks are used. A test case was performed by using the "2D circles" case while choosing 500 even-distributed landmarks on each circle (1000 landmarks in total). It takes 0.95 sec for the current LIBR while 6.5 min for TPS-LIBR.

3.3.2 Experiments With 3D MDCT Lung Images

In this section, we compare the proposed hybrid method against LBR and IBR using the same 3D MDCT lung images in Section 2.3.1. In order to evaluate different approaches, we randomly chose half the landmarks for matching and the rest for validation for each subject. Figure 3.4 shows an example of the landmark locations, where segmentations of lungs, vascular and airway trees are automatically obtained by using a segmentation software package PW2: VIDA Diagnostics (Coralville, Iowa, USA). It is noted that the beginning point of the trachea is used for both matching and validation. It is reasonable to assume that these beginning points at FRC and TLC have the correspondence in these cases since they are close to the

vocal cord and the trachea is relatively rigid in that region.

Figure 3.5 shows the landmark distance of the validation landmarks before and after registrations with LBR, IBR and the hybrid across all registration pairs. The hybrid yields the smallest registration errors since it combines both landmark and intensity information. A linear mixed model with "method" as the fixed effect and "subject" as the random effect is used to compare the average landmark errors among the three methods. The results show that the hybrid yields a significant improvement against both LBR (with p-value < 0.001) and IBR (with p-value $= 0.002$). In addition, TPS-Hybrid is used for all six subjects but the registration fails for two subjects because negative Jacobian occurs after the landmark matching. Statistical analysis is also performed to compare the average landmark errors by using TPS-Hybrid and the proposed hybrid based on the other four subjects and the differences are not statistically significant (with p-value $= 0.96$). This shows that the proposed hybrid can produce accurate results as TPS-Hybrid but ensure local invertibility for large deformation transformations.

Figure 3.6 shows the surface distance map of the registration-predicted FRC airway tree to the original FRC airway trees for (a) LBR, (b) IBR and (c) the hybrid. The registration-predicted FRC airway tree is obtained by applying the transformation to the airway surface mesh at TLC. By comparing these plots, the hybrid yields the best matching result among all three approaches. LBR can match the airway tree at bifurcations but it yields a poor matching for the branches. IBR can match the branches well but it causes a shift at the beginning point of the trachea, which causes the trachea to erroneously shorten. The large distances in the distal ends of the airways do not represent mismatches but rather differences in the FRC vs TLC segmentations. At TLC the airways are detectible further out

towards the peripheral lung.

3.3.3 Moving Airway Geometry

The moving airway geometry could then be derived based on Eq. (3.7). Figure 3.7 demonstrates a dynamic airway geometrical model by using the LIBR method. The four panels shown in Figure3.7 correspond to four different time points in a breathing curve ($t = 0$, $t = T/6$, $t = T/3$, and $t = T/2$, with T as the period), where left and right panels correspond to the lower lung volume and higher lung volume, respectively.

In addition, we build a dynamic lung model and apply it for CFD simulation by using a pair of data sets acquired at 85%VC and 55%VC from a normal subject (the same data sets used in Chapter 4). The lung volume difference between the two data sets is about 1.5 liters. We derive the geometries, such as airways, lungs, and lobes, at an arbitrary phase. Figure 3.8 shows the deformed airway at four different time points (left: $t = 0$; middle left: $t = T/6$; middle right: $t = T/3$; right: $t = T/2$, with T as the period). Similarly, we also show the deformed geometries for lungs and 1D airway tree, see Figure 3.9. The 1D airway tree is generated by a volume filling method [105]. The CFD simulation with the prescribed airway motions is performed and the results are shown in Figure 3.10, where the registration-derived deformation between the two imaged lung volumes is scaled down to a normal quiet breathing with a tidal volume of 500 ml.

We recognize that non-straight-line displacement and the effect of hysteresis should not be neglected [4], however, these assumptions might be appropriate since a high-order parameterization cannot be fully utilized given only a pair of images. In this work, we aim to demonstrate the capability to develop a dynamic lung model

based on image registration. This idea can be extended to account for non-straight-line displacement and hysteretic effects by using multiple lung volumes (or dynamic lung data sets) and high-order trajectory modeling approach.

3.4 Discussion

In this chapter, we aim to develop a compliant airway model for CFD simulation. We first proposed a hybrid registration approach to further improve the alignment of airway geometry by incorporating the airway bifurcation points into the mass preserving registration. We then used a simple linear interpolation method to derive airway geometry at arbitrary phases during respiration from two MDCT volumetric images. Statistical results from 6 registration pairs show that LIBR yields the significantly improved results compared with LBR or IBR alone. LBR can match the airway tree at bifurcations but it yields a poor matching for the branches. By contrast, in spite of a good match in the branches, IBR yields a shift at the beginning point of the trachea, shortening erroneously the trachea. We seek to apply this approach to match multiple lung volumes acquired between TLC and FRC in the same scanning session or over short periods of time and adopt high-order interpolation to take into consideration to improve the current dynamic airway model for CFD simulation in future. It is believed that understanding airway motion and wall shear stress is important in understanding lung pathophysiology because localized change in tissue stiffness (or compliance) occurs during development and progression of lung diseases, such as emphysema and/or chronic obstructive pulmonary disease (COPD), interstitial pulmonary fibrosis (IPF), and asthma.

Table 3.1: Landmark distance and metric value of SSD before and after registrations with four approaches: LBR, IBR, LIBR and TPS-LIBR for 2D binary image experiments.

	"2D Squares"				"2D Circles"			
	SSD	Landmark Distance (mm)	J_{min}	Time (s)	SSD	Landmark Distance (mm)	J_{min}	Time (s)
Before Reg.	32.4	22.27±12.66	-	-	0.0	27.58±9.49	-	-
LBR	11.9	0.0 ±0.0	0.19	0.04	9.5	0.0 ±0.0	0.13	0.10
IBR	1.3	24.44±13.03	0.44	0.56	0.0	27.58±9.49	1	0.19
LIBR	1.4	0.74±0.48	0.34	0.51	1.7	0.68±0.44	0.19	0.71
TPS-LIBR	4.1	0.80±0.40	-0.38	0.54	22.7	0.81±0.36	-0.51	0.84

$*$: The minimum Jacobian value (J_{min}) and computational time for each approach are also listed.

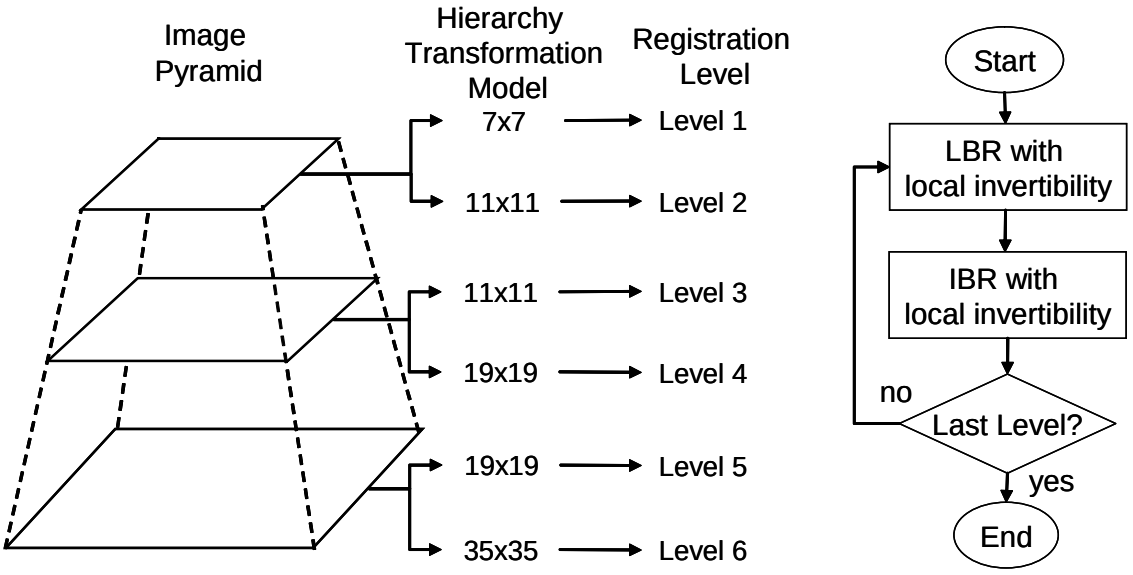

Figure 3.1: Sketch of the multi-resolution framework and flow chart of the whole registration procedure for the hybrid registration approach. The sketch of the framework is illustrated in 2D but the basic idea also works for 3D.

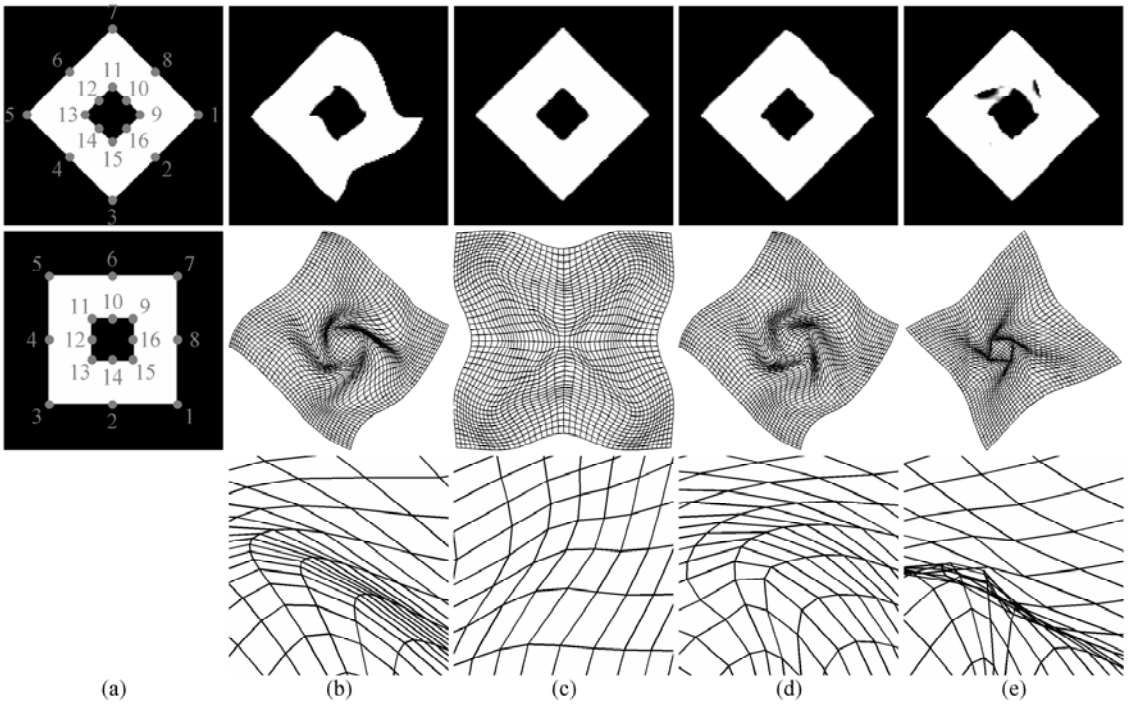

Figure 3.2: "2D Squares" experiment. Column (a) shows the reference (top) and floating (middle) images, where the landmarks are marked and labeled with the numbers showing the correspondence; columns (b)-(e) show the results for registrations with LBR, IBR, LIBR, and TPS-LIBR, respectively. The deformed image (top), the deformed grid (middle) as well as the enlarged view of the deformed grid (bottom) are presented for each approach.

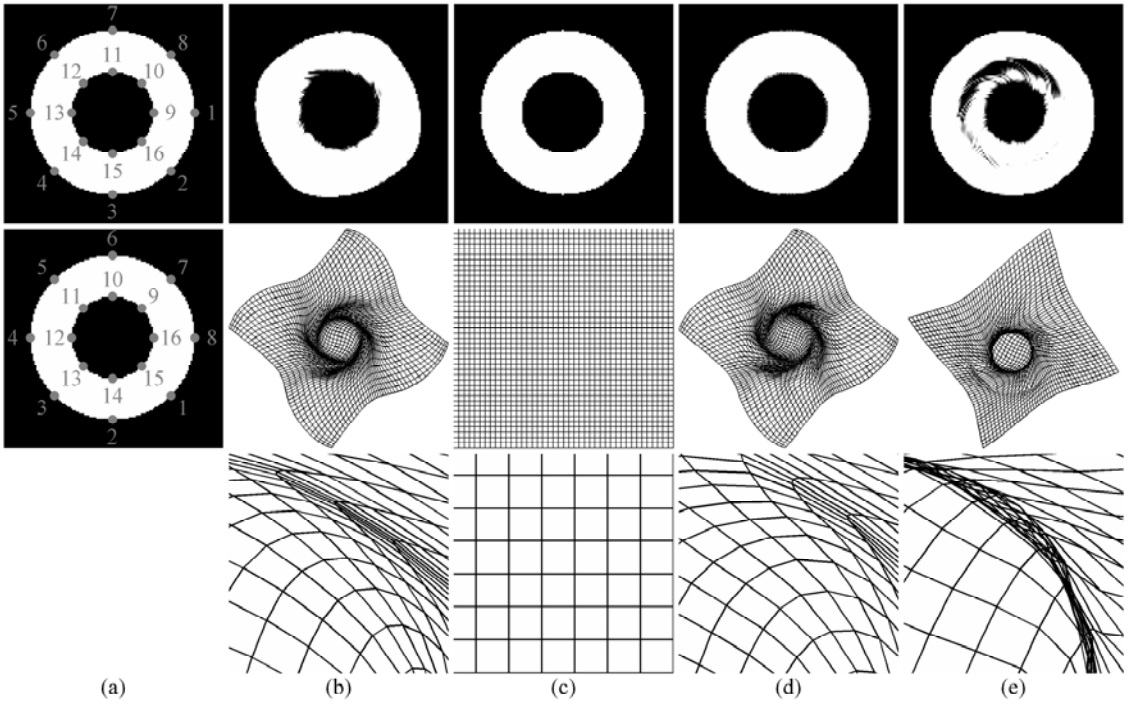

Figure 3.3: "2D Circles" experiment. Column (a) shows the reference (top) and floating (middle) images, where the landmarks are marked and labeled with the numbers showing the correspondence; columns (b)-(e) show the results for registrations with LBR, IBR, LIBR, and TPS-LIBR, respectively. The deformed image (top), the deformed grid (middle) as well as the enlarged view of the deformed grid (bottom) are presented for each approach.

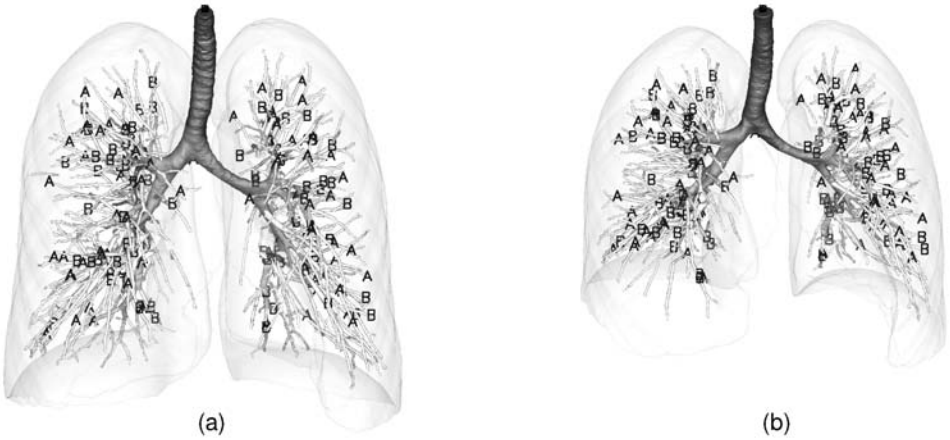

Figure 3.4: Illustrate of landmark locations for (a) TLC and (b) FRC from one subject. The landmarks used for matching are marked by 'A' and the landmarks used for validation are marked by 'B'. Surface rendering of airways, major vessels and lungs is shown for reference.

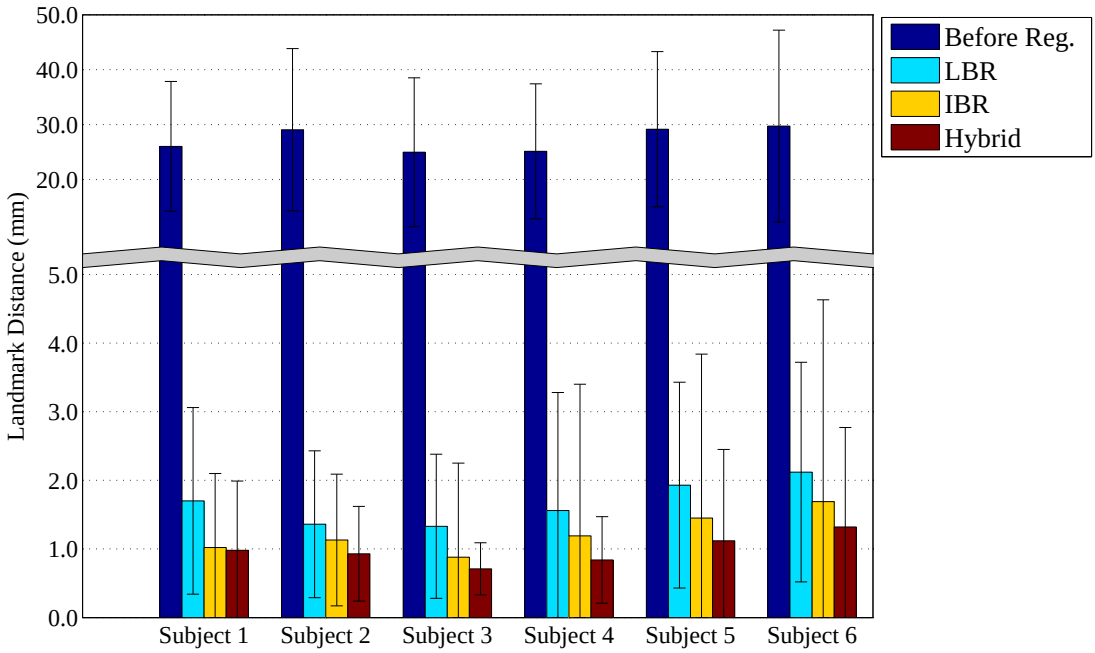

Figure 3.5: Landmark distance of the validation landmarks before and after registrations with LBR, IBR and Hybrid across all registration pairs.

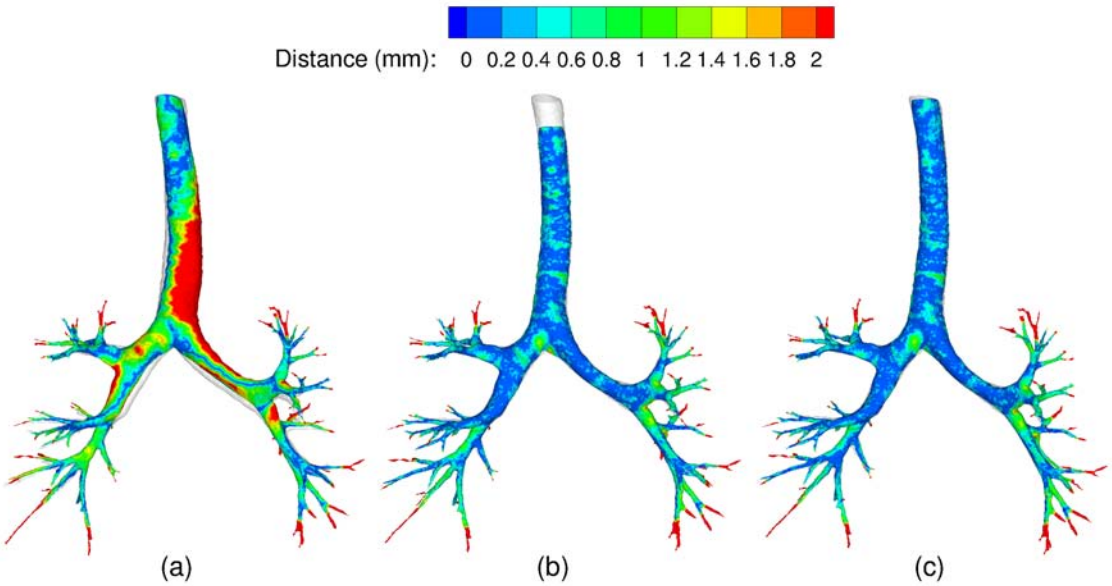

Figure 3.6: Surface distance map of the registration-predicted FRC airway tree to the original FRC airway trees for LBR (a), IBR (b) and Hybrid (c). The original FRC airway trees are shown in white for reference.

Figure 3.7: Airway geometries at four different time points from the dynamic airway model for a TLC-FRC image pair with the LIBR method. The lung volume difference between the two images is 2.4 liters. From left to right: $t = 0$; $t = T/6$; $t = T/3$; and $t = T/2$ (T is the period).

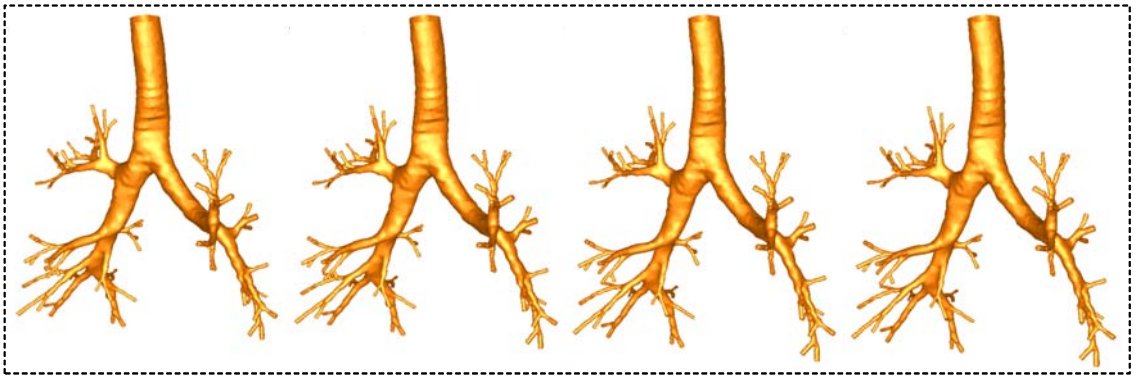

Figure 3.8: Airway geometries at four different time points from the dynamic airway model for the 85%VC-55%VC image pair with the LBR method. The lung volume difference between the two images is 1.5 liters. From left to right: $t = 0$; $t = T/6$; $t = T/3$; and $t = T/2$ (T is the period).

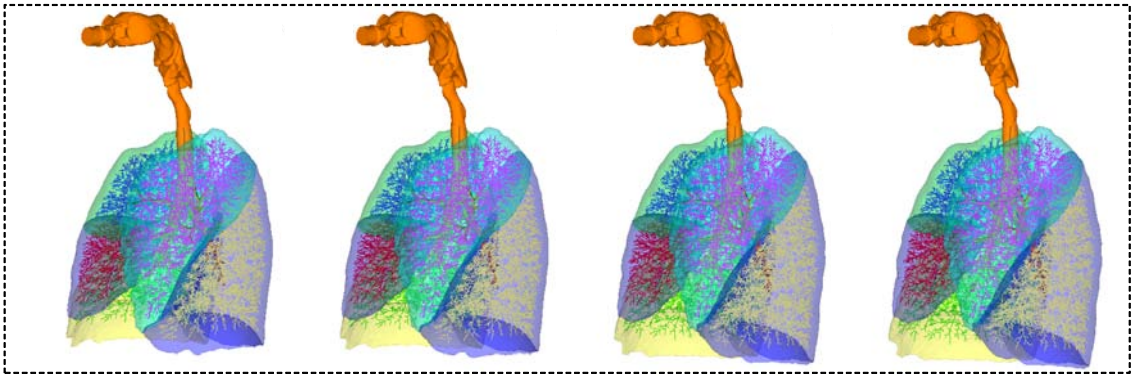

Figure 3.9: Deformed geometries at four different time points from the dynamic lung model for the 85%VC-55%VC image pair with the LBR method. From left to right: $t = 0$; $t = T/6$; $t = T/3$; and $t = T/2$ (T is the period). Lobes, 3D upper and center airways, and 1D centerline airways are shown here.

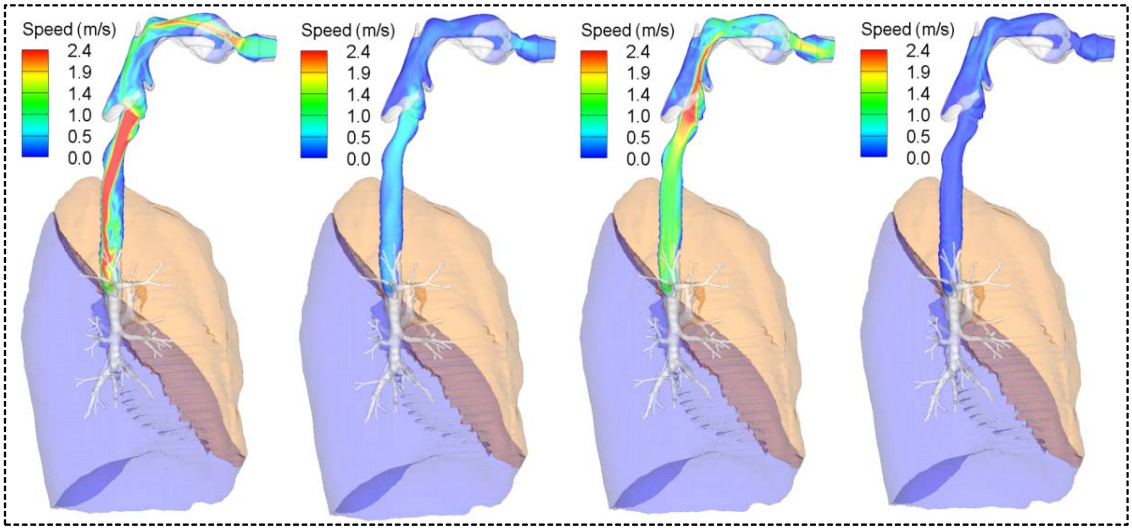

(a) t/T = 0.15 (b) t/T = 0.5 (c) t/T = 0.8 (d) t/T = 1.0

Figure 3.10: Velocity contour in a vertical plane at four selected time points from the dynamic airway model for the 85%VC-55%VC image pair. The registration-derived deformation between the two scanned lung volumes is scaled down to a normal quiet breathing with a tidal volume of 500 ml.

CHAPTER 4
SUBJECT-SPECIFIC BOUNDARY CONDITIONS

4.1 Introduction

CFD has been extensively used to investigate pulmonary air flow in the human lungs from the large central bronchial airways to the acinar regions. A representative though not exhaustive list of such studies can be found in [11, 28, 53, 62, 64–66, 71, 99, 116]. Due to the complexity of the human tracheobronchial tree, most earlier CFD studies of pulmonary air flow used either the symmetric Weibel model [120] or the asymmetric Horsfield model [43]. Although these studies provide some insights into the characteristics of flow in systems of bifurcating tubes, their idealized airway models lack subject-specific geometrical features for assessing an individual's response to inhaled particulates and for better tailoring a treatment plan for the individual. With rapid advances in medical imaging and computational techniques, 3D realistic airway geometries with major branches derived from high resolution MDCT images have recently been used in CFD studies [11, 28, 64, 65]. In addition, one-dimensional (1D) centerline airway models generated from subject-specific lobe configurations, such as by Tawhai et al. [105], have been used to investigate gas mixing [106]. However, in most of these studies simple uniform boundary conditions (either uniform velocity, uniform pressure, or uniform flow distribution) were imposed at the ending airway segments, which may limit the accuracy of the results due to the inability to take into consideration the realistic non-uniform ventilation and regional lung pathology. Different approaches have also been proposed with attempts to overcome this boundary condition problem. Nazridoust and Asgharian [76] have studied particle depositions in a three-generation cylindrical tube

network using non-uniform outlet boundary conditions which were derived based upon a mathematical lung ventilation model [10]. De Backer et al. [21] specified two different pressure values at the ends of the 3D CT-resolved left and right main bronchi as an approximation of a subject-specific boundary condition. In addition, 3D-impedance coupled approaches, in which the impedance is estimated from a 1D model in the frequency domain and is transformed into the time domain to define the pressure at the specific outlet, have also been applied to air flows in the human respiratory system [17, 70]. However, currently a uniform zero pressure at the distal end of the alveoli-tissue unit (root of 1D impedance tree) is still assumed in these 3D-impedance coupled approaches. Recently, Tawhai et al. [108, 109] developed a soft-tissue-mechanics-based model for elastic deformation of the compressible lung tissue, in which the local volume change of the peripheral tissue can be used for setting a flow boundary condition for the 1D centerline airway model. And Lin et al. [65] proposed a multi-scale CFD framework that couples a 3D MDCT-resolved central airway tree with a 1D centerline airway tree in a physiologically and morphometrically consistent manner: the 1D peripheral airway tree serves as a link between 3D central airway tree and lung parenchyma. With the 1D and 3D coupling framework, a subject-specific boundary condition can be imposed on the 3D central airways via the 1D tree using the information of regional ventilation.

Regional ventilation has been measured using imaging techniques, such as MR [86, 115] and xenon CT [13, 14]. Currently MR is only partially quantitative because of a limited capability for depiction of anatomic detail. MR is also costly, requiring specialized equipment to hyperpolarize the gas that is used for imaging. Xenon CT can predict a high resolution ventilation map but it requires the use of expensive xenon gas and the associated hardware for controlled gas delivery. Alternatively,

regional ventilation can be generated by registering two volumetric MDCT data sets [15, 22, 32, 79, 129]. In contrast to MR or xenon CT, such registration-based analysis of regional ventilation requires only two volumetric data sets of the lung at different levels of inflation and the resulting ventilation map has a high resolution.

In this chapter, we propose a technique to estimate a subject-specific boundary condition with two MDCT lung data sets by means of an image registration method. The derived boundary condition is then applied for CFD simulation of pulmonary air flow and is compared against two traditional boundary conditions (uniform velocity or uniform pressure).

4.2 Methods

4.2.1 Method Overview

Figure 4.1 shows a flow chart of the entire process. Two CT volumetric data sets are acquired at different levels of inflation in the same scanning session. A mass-preserving image registration is then performed to match the two data sets to derive a warping function, defined as a voxel-by-voxel displacement, to estimate regional ventilation. Meanwhile, a subject-specific 1D centerline airway tree is generated based on the image with larger lung volume using a volume filling method proposed in [105], by using the lobes as "boundary conditions" and the skeleton of the 3D CT-resolved central airway tree as "initial conditions". The registration-derived regional ventilation map is then associated with the 1D tree to estimate air flow at the approximately 30,000 terminal branches of the tree. Terminal airway flows are further used to produce the subject-specific boundary conditions for the 3D CT-resolved central airway by utilizing the connectivity information between the

3D airway and the associated downstream 1D airway branches.

4.2.2 MDCT Image Acquisition

The two 3D MDCT volumetric data sets were acquired from a normal human subject (a 32-year old white non-Hispanic male) with a Siemens Sensation 64 MDCT scanner (Forchheim, Germany) during breath-holds in a single scanning section. The protocol was approved by the University of Iowa's Institutional Review Board. The subject lay supine and breathed through a mouthpiece during the scanning session. One volumetric data set was acquired at 85% of vital capacity (VC), referred to hereafter as the reference image I_r, and the other was at 55% of VC, referred to hereafter as the floating image I_f. Each data set consists of 553 slices with a spacing of 0.6 mm and a reconstruction matrix of 512×512 pixels. In-plane pixel spatial resolution is 0.68×0.68 mm^2. The two data sets were processed using a software package Pulmonary Workstation 2 (PW2: VIDA Diagnostics, Coralville, Iowa) to segment the lungs, lobes and central airways. The segmented airways were further skeletonized to obtain the centerlines of individual branches.

4.2.3 Registration-Derived Regional Ventilation

The mass preserving nonrigid registration method described in Chapter 2 is used to match the pair of volumetric MDCT data sets. Once image registration is performed, we can calculate regional ventilation, which is referred to as the local air volume difference in this work. The local air volume difference is jointly estimated from changes in local air fraction along with the registration-derived local Jacobian value and is written as

$$\begin{aligned} \mathrm{rV}(\mathbf{x}) &= V_r(\mathbf{x})\,\gamma_{\mathrm{air}}\left(I_r(\mathbf{x})\right) - V_f\left(\mathbf{T}(\mathbf{x})\right)\gamma_{\mathrm{air}}\left(I_f\left(\mathbf{T}(\mathbf{x})\right)\right) \\ &= V_r(\mathbf{x})\left[\frac{\mathrm{HU}_{\mathrm{tiss}} - I_r(\mathbf{x})}{\mathrm{HU}_{\mathrm{tiss}} - \mathrm{HU}_{\mathrm{air}}} - J_T(\mathbf{x})\frac{\mathrm{HU}_{\mathrm{tiss}} - I_f\left(\mathbf{T}(\mathbf{x})\right)}{\mathrm{HU}_{\mathrm{tiss}} - \mathrm{HU}_{\mathrm{air}}}\right]. \end{aligned} \tag{4.1}$$

The regional ventilation map describes local air volume changes between two volumetric data sets. Thus, it can be used to provide a subject-specific boundary conditions for the 3D central airways in a 3D and 1D coupling framework [65].

4.2.4 Subject-Specific Boundary Conditions

Region ventilation can be used to provide subject-specific boundary conditions for the 3D central airway in the 3D and 1D coupling framework [65], in which the 1D airway model serves as a link between 3D central airway and lung parenchyma. The current 1D airway model is generated using the volume filling method proposed by Tawhai et al. [105] that takes the lobes as "boundary conditions" and the skeleton of the 3D MDCT-resolved central airway tree as "initial conditions". The volume filling method is a recursive algorithm that fills lobes with bifurcating trees spanning the entire conducting airway from the ending segments of MDCT-resolved central airways to terminal bronchioles. At first, a set of seed points, each corresponding to a region approximately representing a cubic pulmonary acinus, is uniformly distributed in lungs with the number approximately equal to the expected number of terminal bronchioles (30,000). The recursive algorithm starts by associating each seed point to its nearest peripheral branch in the respective lobe. The set of associated seed points are then divided into two subsets by a plane, defined by two nodes of the associated branch and the centroid of the set itself. Two daughter branches are created with direction towards the centroid of the respective subset,

and length 40% of the distance from the end of its parent branch to the centroid. This process repeats until all peripheral branches are terminal branches that are determined based on their lengths (less than a predefined length limit) or the number of associated seed points (equal to 1). If a branch is determined as a terminal branch, it would no longer be associated with any seed points and the closest seed point to its ending node is removed from the global set of seed points.

Since each terminal branch of the 1D airway model is associated with a specific cubic region of lung, it is reasonable to assume that change of air volume within the cube is equivalent to air flow for the corresponding terminal bronchiole. Thus, when a branch is determined as the terminal bronchiole, we calculate the sum of registration-predicted regional ventilation of all voxels in its associated cubic region and impose it as the air flow for that branch. By mass conservation the air flow at the ending segments of the MDCT-resolved 3D central airways can be determined by summing the air flow of terminal bronchioles with the connectivity information between the 3D airway and the associated downstream 1D airway branches.

4.2.5 CFD Simulation

Simulations of air flows using the proposed subject-specific boundary conditions can then be performed. Large eddy simulation (LES) was adopted to capture transitional and turbulent flow. The governing equations consist of the filtered continuity equation and Navier-Stokes equations for incompressible flow:

$$\frac{\partial \bar{u}_j}{\partial x_j} = 0, \tag{4.2}$$

$$\frac{\partial \bar{u}_i}{\partial t} + \bar{u}_j \frac{\partial \bar{u}_i}{\partial x_j} = -\frac{1}{\rho}\frac{\partial \bar{p}}{\partial x_i} + \frac{\partial}{\partial x_j}\left[(\nu + \nu_T)\frac{\partial \bar{u}_i}{\partial x_j}\right], \tag{4.3}$$

where u_i, p, ρ, ν, and ν_T are the ith component of velocity, pressure, density,

kinematic viscosity, and subgrid-scale eddy viscosity, respectively. The density and the kinematic viscosity of the air are 1.2 kg/m^3 and $1.7 \times 10^{-5} m^2/s$, respectively. The overbar denotes resolved quantities. The eddy-viscosity subgrid-scale model proposed by Vreman [118] was used to account for the transitional and anisotropic flow characteristics. A fractional four-step and characteristic Galerkin method based finite element scheme was employed in solving Eqs. (4.2) and (4.3) [63].

Once the CFD simulation was performed, particle tracking was done as a post-processing step. Each particle's motion was individually computed based on Lagrangian particle tracking equation

$$\frac{\partial u_{p_i}}{\partial t} = F_D(u_i - u_{p_i}) + g_i(\rho_p - \rho)/\rho_p \tag{4.4}$$

where i denotes the ith component direction, u_p is the particle velocity, u is the fluid velocity, g is the gravitational acceleration, ρ_p is the particle density equal, and ρ is the fluid air density. In this work, g is set as $(0, -9.8m/s^2, 0)$ and ρ_p is set to $1,200kg/m^3$. The term $F_D(u_i - u_{p_i})$ is the drag force per unit mass on the particle and the calculation of F_D can be found in [77] and [55]. Equation (4.4) is integrated to calculate the particle motion. Spherical particles are distributed at the mouthpiece inlet and particle velocity was initialized to be equal to fluid velocity plus a small random component. The particle diameter of 10 μ m is selected in this study to investigate effects of boundary condition on both ventilation and deposition of the particles, considering that its overall deposition efficiency is about 50% and oral deposition is only about 10% as we have shown before [55]. A total of 46 LES data sets were used for particle tracking, with each data set being $0.048s$ apart. At each time step increment, the fluid velocity is interpolated between two of the LES data sets in order to obtain an instantaneous flow field for the particle transport.

The interpolation method used a second-order approach that utilizes fluid velocity at each of the four node points of the tetrahedral element containing the particle. If the shortest distance from the center of mass of the particle to the airway wall is less than the particle radius, it is considered deposited.

4.3 Results

4.3.1 Registration Accuracy

The mass preserving image registration method has previously been tested using six pairs of lung MDCT scans in Chapter 2. The registration accuracy in this work is assessed visually by examining anatomic information. Figures 4.2(a) to (c) show sagittal sections of the left lung from: (a) the reference image I_r; (b) the warped image obtained by the registration; and (c) the floating image I_f at the same axial locations, respectively. The sagittal sections are oriented such that the diaphragm is at the bottom, the dorsal surface (nearest the scanner table) is on the right and the ventral surface is on the left. The comparison of Figures 4.2(a) and (b) shows good anatomic correlation between the image I_r and the warped image.

4.3.2 1D Centerline Airway Trees

With the segmentation of the lobes and the skeleton of MDCT-resolved central airway, we can generate the 1D centerline airway trees using the volume filling method. Figure 4.3(a) shows the surface geometries of the lobes, MDCT-resolved upper and central airways. These surface geometries are obtained by converting the segmentation into surface meshes with a Marching Cubes algorithm [67] and further smoothing the meshes using a without-shrinkage smoothing technique [104].

Figure 4.3(b) shows the generated 1D centerline airway trees. The 3D MDCT-resolved upper and central airways with the skeleton (orange) of central airways are also shown in Figure 4.3(b) for reference. The lobes and lobar airway trees in both Figures 4.3(a) and (b) are shown in different colors: green for left upper lobe (LUL), red for left lower lobe (LLL), cyan for right upper lobe (RUL), blue for right middle lobe (RML) and purple for right lower lobe (RLL).

Once the entire 1D centerline airway tree is generated, we can calculate the Strahler order for each branch. The Strahler ordering scheme is commonly used for a tree and it starts at the terminal branches (order 1) and proceeds up towards the trachea. The parent branch is one order higher than the child branch only if all child branches are of equal order; otherwise the parent has the same order as the child branch of the highest order. Morphometric analysis for the human bronchial tree shows a linear relationship if the number of branch and mean length of branches at each order are plotted on a log scale against the Strahler order. Figure 4.4 shows these Strahler-order-based log plots of the number of branches and mean length for our generated 1D model with regression line shown for each. It is clear that both plots show log-scaled linear trends.

4.3.3 Regional Ventilation

Registration-derived regional ventilation was validated by comparison with measured global values: (1) the average Jacobian value and (2) the total air volume difference. The measured average Jacobian value is defined as the ratio of the total lung volume of the floating image I_f to that of the reference image I_r, where the total lung volumes for images I_r and I_f are 7.60 liter (L) and 6.09 L, respectively. The measured total air volumes can be calculated from the total lung volume and

the average air fraction, where the average air fraction is estimated from average HU inside the lung with Eq. (1.2). For the images I_r and I_f used in this study, the measured total air volumes are 6.72 L and 5.20 L, respectively. Thus, the measured total air volume difference is 1.52 L between the two images. In contrast to the measured values, the registration-derived average Jacobian value is calculated from local Jacobian values in the lungs and the registration-derived total air volume difference is the sum of local air volume difference of all voxels in the lungs. Table 4.1 shows the comparison between the measured values and the registration-derived values. It is clear that the registration-derived average Jacobian value matches well with the measured one and the registration-derived total air volume difference is also close to the measured value with a small error of 2.6%.

4.3.4 CFD Results

The 3D MDCT-resolved upper airway and central airway tree shown in Figure 4.3 are used as computational domain for CFD simulation. An unstructured mesh with 899,465 nodes and 4,644,447 tetrahedral elements was generated. The whole computational domain was divided into 256 partitions and the simulation was conducted on the Lonestar cluster at the Texas Advanced Computing Center. The time step was set to $2.0 \times 10^{-5} s$, resulting in an average Courant-Friedrichs-Lewy (CFL) number of about 0.044. Further details of the 3D fluid solver including validation can be found in [64] and [11]. A flow rate of 0.342 L/s at the peak inspiration was imposed at the mouthpiece inlet, resulting in a Reynolds number of 1,380 in the trachea. The outlet boundary conditions at the ending airway segments were set with the proposed subject-specific boundary condition (case 1), uniform velocity boundary condition (case 2) and uniform pressure boundary condition (case 3),

respectively. The reference pressure was selected at the tracheal inlet.

In the trachea and main bronchi, no obvious differences are found for the mean and turbulent velocity features. The strength and structure of the turbulent laryngeal jet is similar in all three cases (not shown). However, the differences in regional distribution of velocity and pressure become noticeable as the air flow is bifurcated into the airways in downstream generations.

Figures 4.5(a)-(c) show comparison of distributions of outlet velocity and static pressure for the three cases. The distributions in Figure 4.5(a) for the proposed boundary condition are more heterogeneous than those of the uniform velocity boundary condition in Figure 4.5(b) and the uniform pressure boundary condition in Figure 4.5(c). In particular, the proposed boundary condition predicts much greater pressure drop at the airways in the LLL and the RLL shown in Figure 4.5(a). In contrast, the uniform velocity boundary condition yields greater pressure drop in the RML than others, whereas the uniform pressure boundary condition enforces the same pressure drop in all five lobes.

Quantitative comparisons of lobar distribution of air flow are presented in Figure 4.6. The proposed method results in larger deviation between lobes, reflecting the nature of heterogeneity of ventilation in the human lung. The measured values (the lobar difference of air content) are also shown. The lobar distributions predicted by the proposed method match well with these measured values with an overall relative error of 4.79%, seen from Table 4.2. The large relative error for RML is due to the small measured value for that lobe (0.052). However, the uniform outlet velocity and uniform outlet pressure methods yield errors of 43.42% and 27.08%, respectively. The uniform velocity boundary condition results in over-prediction (more than twice) of the ventilation to the RML, yielding a greater pressure drop

in the RML shown in Figure 4.5(b). Both uniform pressure and uniform velocity boundary conditions under-predict the ventilation to the two lower lobes LLL and RLL.

In addition, a snapshot of regional distribution of flow velocity and particles is presented in Figure 4.7 for the comparison among three different boundary conditions. It is observed that at the instant more particles propagate toward upper side of RMB for the proposed BC, while they are toward the lower wall for the uniform velocity BC. For the pressure BC case, most particles enter LMB instead of RMB. Figure 4.8 shows the comparison of particle ventilation and deposition fractions in five lobes. The lobar particle ventilation fraction is defined by the number of the particles that enter each lobe over the total number of particles that enter all five lobes. And the lobar particle deposition fraction is defined as the number of the particles that deposit in airway branches associated with each lobe over the total number of particles that deposit in all lobes. As shown in Figure 4.8, lobar particle ventilation and deposition fractions follow the lobar flow rate fractions. More particles enter and deposit in the lower lobes than the upper or middle lobes. Lobar difference of both particle ventilation and deposition are under-predicted by the uniform velocity and the uniform pressure boundary conditions compared to the proposed one.

4.3.5 Analysis Of Repeatability

In this chapter, subject-specific boundary conditions are described from a pair of MDCT lung data sets acquired during breath-holds at different levels of inflation. The registration-derived regional ventilation is passed to 3D central airways via a 3D-1D airway coupling framework. In the following sections we will discuss

the uncertainty due to the generated 1D airway tree and the repeatability of the registration-based assessment of regional ventilation.

4.3.5.1 Uncertainty Due To 1D Tree Structure

The generated 1D airway tree is served as the link between 3D airway outlets and parenchyma to describe the boundary conditions at the 3D airway outlets. We expect that the effects of the generated 1D tree structure on the 3D boundary conditions should be subtle since the 3D boundary conditions depend on the affected parenchyma regions, instead of the local 1D airway structures. However, in order to quantify the uncertainty due to the 1D airway, we generated three different 1D airway trees (Tree 1, Tree 2 and Tree 3) by adjusting the parameters and calculated the differences of the resulting 3D outlet boundary conditions among the three 1D airway trees. The results shows that the differences are considered to be not statistically significant between Trees 1 and 2 (with p-value = 0.9943) and Trees 1 and 3 (with p-value = 0.9898), thus demonstrating that the 3D boundary conditions are not sensitive to 1D airway trees.

4.3.5.2 Repeatability Of Registration-Based Assessment Of Regional Ventilation

In addition, fourteen human subjects were used to assess the repeatability of registration-based assessment of regional lung function. For each subject, one scan was acquired at TLC (90% VC) and the two repeat scans were acquired at FRC (20% VC). Scans were performed on a multi-detector row CT (Siemens Sensation 64 or Siemens Definition Flash 128: 110mAs, 120kV, pitch=1, slice thickness = 0.72mm, slice spacing = 0.5mm and voxel size 0.62mm) during breath-holds

using a pneumotachometer-based volume controller. The mass preserving image registration was adopted to register the two repeat FRC scans to TLC scan (i.e. FRC1-TLC, FRC2-TLC) and also register between two repeat FRC scans (FRC2-FRC1). Regional ventilations were assessed by registration-derived Jacobian values and air volume changes (AVC), respectively.

The registration results demonstrate similar Jacobian and AVC values between FRC1-TLC and FRC2-TLC registration pairs, with a mean difference of 0.022 and 0.03, respectively (see Table 4.3). When both FRCs are registered to each other, mean Jacobian is approximately is 1.03, and AVC is -0.04. Inter-subject variability, demonstrated through a Bland-Altman plot, show residual clustering around zero, with most subjects (except subject 2 and 6) within limits of agreement, see Figure 4.9. The two subjects that were outliers had poor compliance during volume control and when removed from the cohort, decreased the standard deviation of the results. The analysis above demonstrates the use of subject-specific image registration to obtain measurement of regional lung function following repeat breath holds.

4.4 Conclusion

In this chapter, we described a technique to estimate subject-specific boundary conditions using a mass preserving image registration. The registration provides an estimation of regional ventilation from a pair of MDCT lung data sets acquired during breath-holds at different levels of inflation in the same scanning session. The registration-predicted regional ventilation map is then associated with a 1D airway tree model generated by a volume filling algorithm to derive a subject-specific boundary condition for 3D MDCT-resolved central airway tree in a 3D and

1D coupling framework.

In contrast to the idealized symmetric airway models, the real human airways are asymmetric and boundary conditions most certainly play an important role in determining the regional distributions of basic flow properties. Advantages of the current boundary condition have been investigated by comparing the CFD results using the proposed subject-specific boundary condition against two conventional boundary conditions (uniform outlet velocity and uniform outlet pressure). It was found that the proposed method resulted in physiologically reasonable regional distribution of velocity and pressure, which was not accomplished by the other two boundary condition methods. We observed that the lobar and the regional distributions of pressure and flow rates in the bronchioles were noticeably affected by the outlet boundary conditions. Moreover, a potential advantage of the proposed boundary condition is that, independent of variation of MDCT resolved airways geometry, 1D airway tree structure is consistently extended to the lung periphery, providing subject-specific boundary conditions to upstream segments. The uniform velocity or uniform pressure condition likely leads to inconsistent results when more or less airway branches are included.

To our knowledge, this work is the first attempt to provide realistic boundary conditions for CFD simulations based upon image registration. The method proposed here uses two volumetric images of the lungs acquired at different inflation and produces boundary conditions that are specific to the subject and to their change in regional lung volume. This method can be extended to match multiple lung volumes acquired between TLC and FRC in the same scanning session, thus providing a way to develop a computational lung model with realistic time-varying boundary conditions in a breathing period. In addition, the proposed method would

benefit from further validation of the registration-derived regional ventilation, such as comparing with the measurements from xenon CT, or hyperpolarize ^{3}He MR [13, 14, 29]. The validated technique would then be applicable to studying pulmonary airflow in subjects with lung diseases that affects ventilation distribution, such as asthma or chronic obstructive pulmonary disease. In these cases, a next step will be to adjust the airway model based upon additional image-based information related to regional tissue destruction [41].

Table 4.1: Comparison between measured and registration-derived values for average Jacobian value and total air volume difference.

	Average Jacobian value	Total air volume difference (liter)
Measured	0.80	1.52
Registration-derived	0.80	1.56
Error percentage (%)	0.0	2.6

Table 4.2: Relative errors of the lobar distributions of flow rate ratio for the three outlet boundary conditions against measured values.

	Proposed (%)	Uniform velocity (%)	Uniform pressure (%)
LUL	3.13	38.61	39.19
LLL	0.09	28.81	16.56
RUL	3.86	18.99	1.00
RML	14.73	117.93	67.69
RLL	2.12	12.76	10.94
Overall	4.79	43.42	27.08

Table 4.3: Mean and standard deviation of Jacobian and air volume change (AVC) across all subjects for three registration combinations (FRC1-TLC, FRC2-TLC, FRC2-FRC1).

		Mean	Standard Deviation
FRC1-TLC	Jacobian	0.486	0.057
	AVC	0.757	0.135
FRC2-TLC	Jacobian	0.503	0.053
	AVC	0.734	0.139
Difference	Jacobian	0.022	0.027
	AVC	0.03	0.037
FRC2-FRC1	Jacobian	1.032	0.068
	AVC	-0.04	0.091

$*$: The differences between FRC1-TLC and FRC2-TLC are also listed.

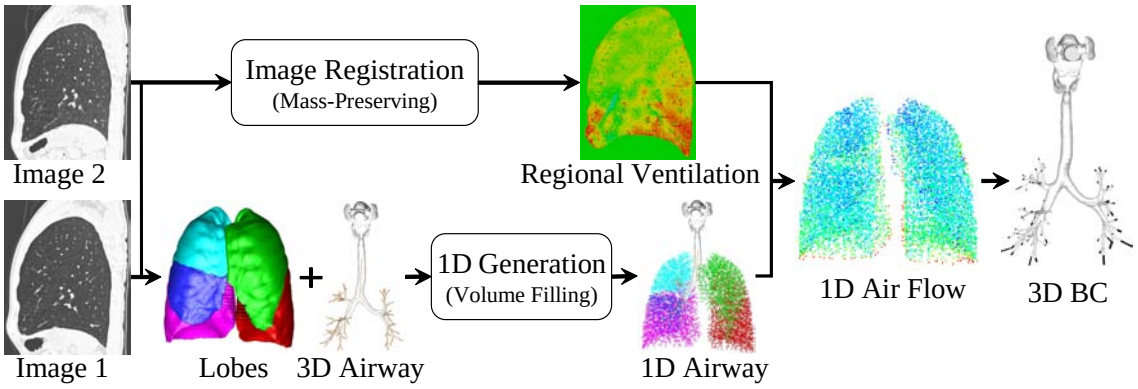

Figure 4.1: A flow chart of the entire process to describe subject-specific boundary conditions.

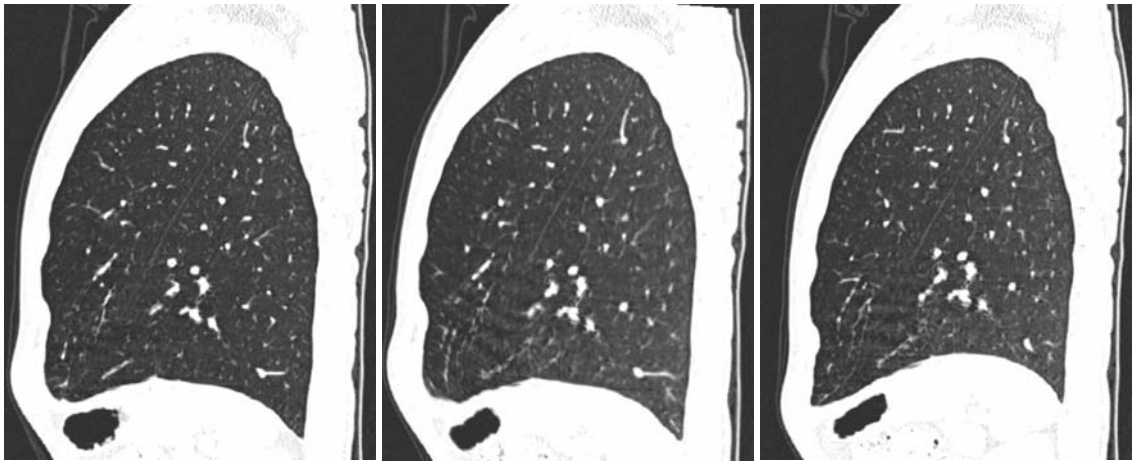

(a) Image I_1 (b) Warped Image $I_2(T(x;\phi))$ (c) Image I_2

Figure 4.2: Visual assessment of registration accuracy. A sagittal slice of the left lung from (a) the image I_r, (b) the warped image obtained by image registration, and (c) the image I_f at the same axial locations.

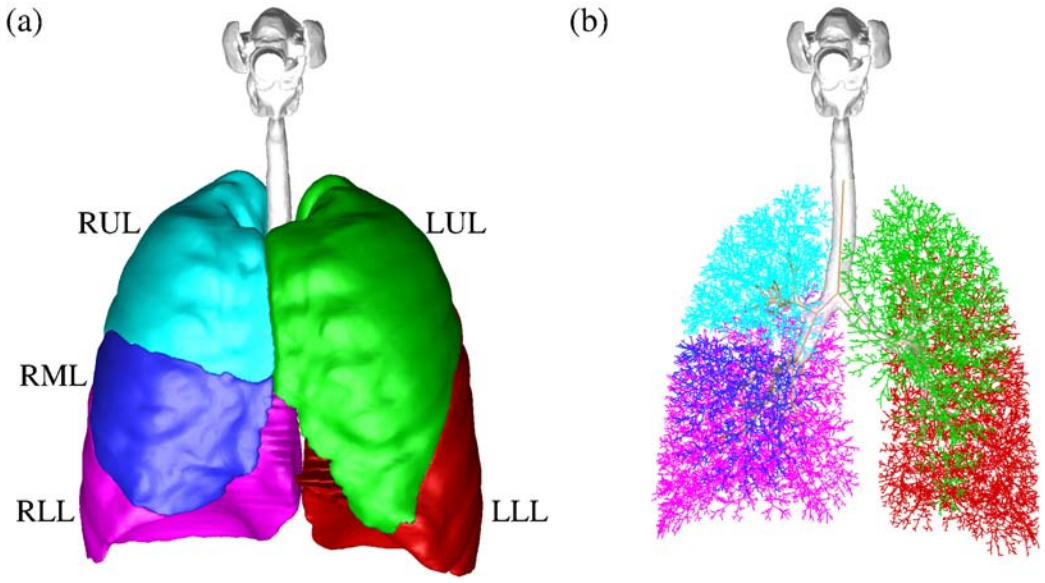

Figure 4.3: Lobar and airway geometries. (a) Surface geometries of the lobes, MDCT-resolved upper and central airways for the image I_r. (b) 1D centerline airway trees generated with the volume filling method. The 3D MDCT-resolved upper airway, central airway tree and its skeleton (Orange) are also shown in (b) for reference. Different colors are used in both (a) and (b) for each lobe and lobar airway: green for left upper lobe (LUL), red for left lower lobe (LLL), cyan for right upper lobe (RUL), blue for right middle lobe (RML) and purple for right lower lobe (RLL).

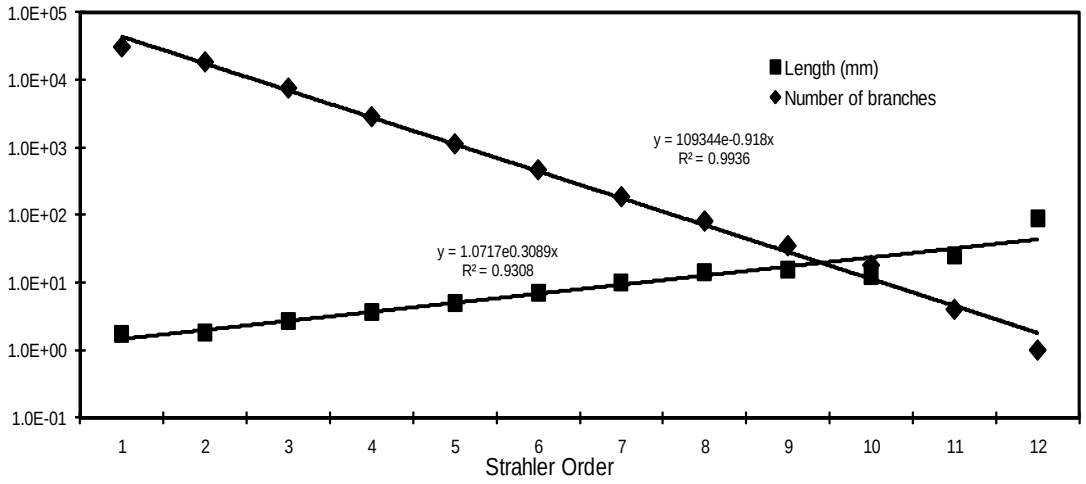

Figure 4.4: Plots of the number of branches and the mean length on log scales against Strahler order. Regression line for each plot is also shown.

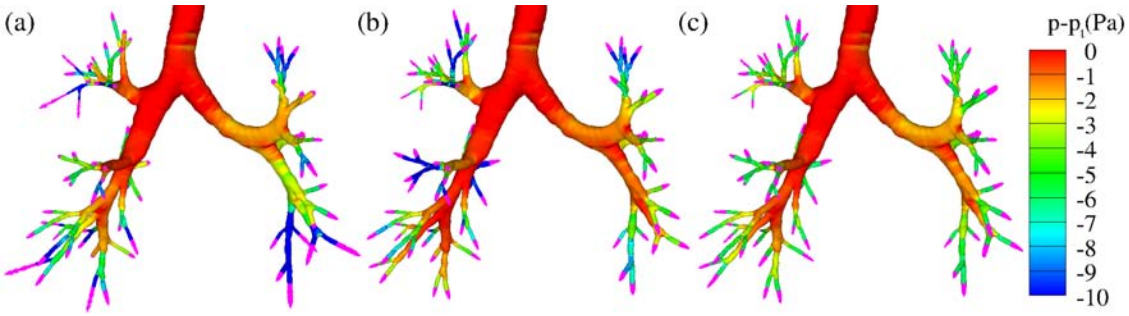

Figure 4.5: Outlet velocity vectors (pink) and pressure contours for the three different outlet boundary conditions: (a) proposed; (b) uniform velocity; (c) uniform pressure.

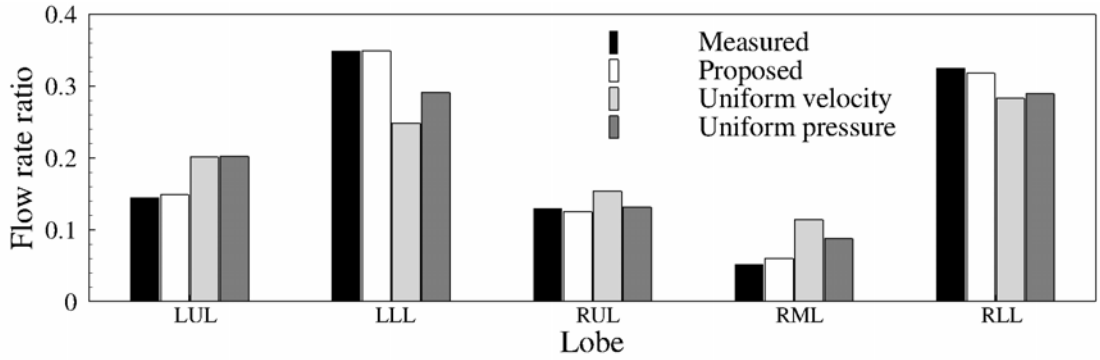

Figure 4.6: Lobar distribution of flow rate ratio for the three cases with different outlet boundary conditions.

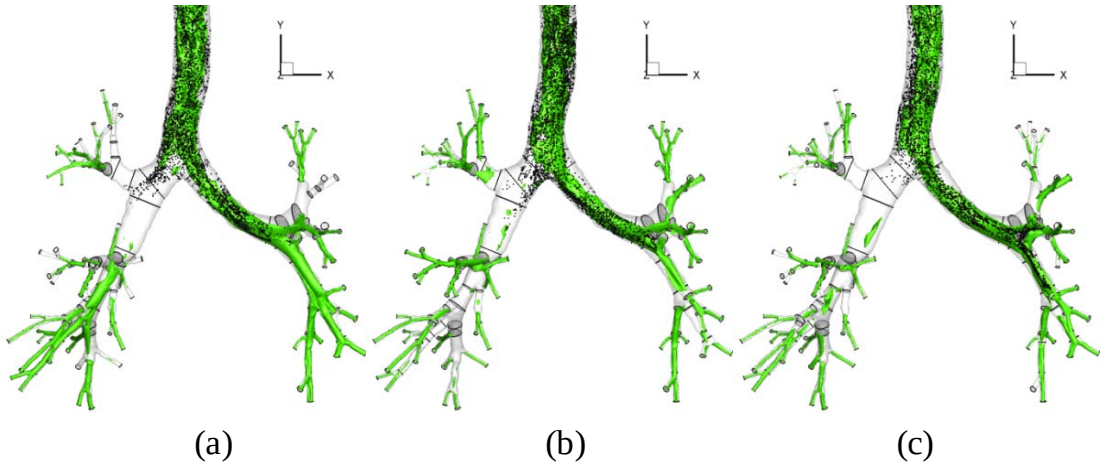

Figure 4.7: Snapshots of particle transport (black dots) with an isosurface of airflow speed (1.7 m/s, green contour) for the three different outlet boundary conditions: (a) proposed; (b) uniform velocity; and (c) uniform pressure.

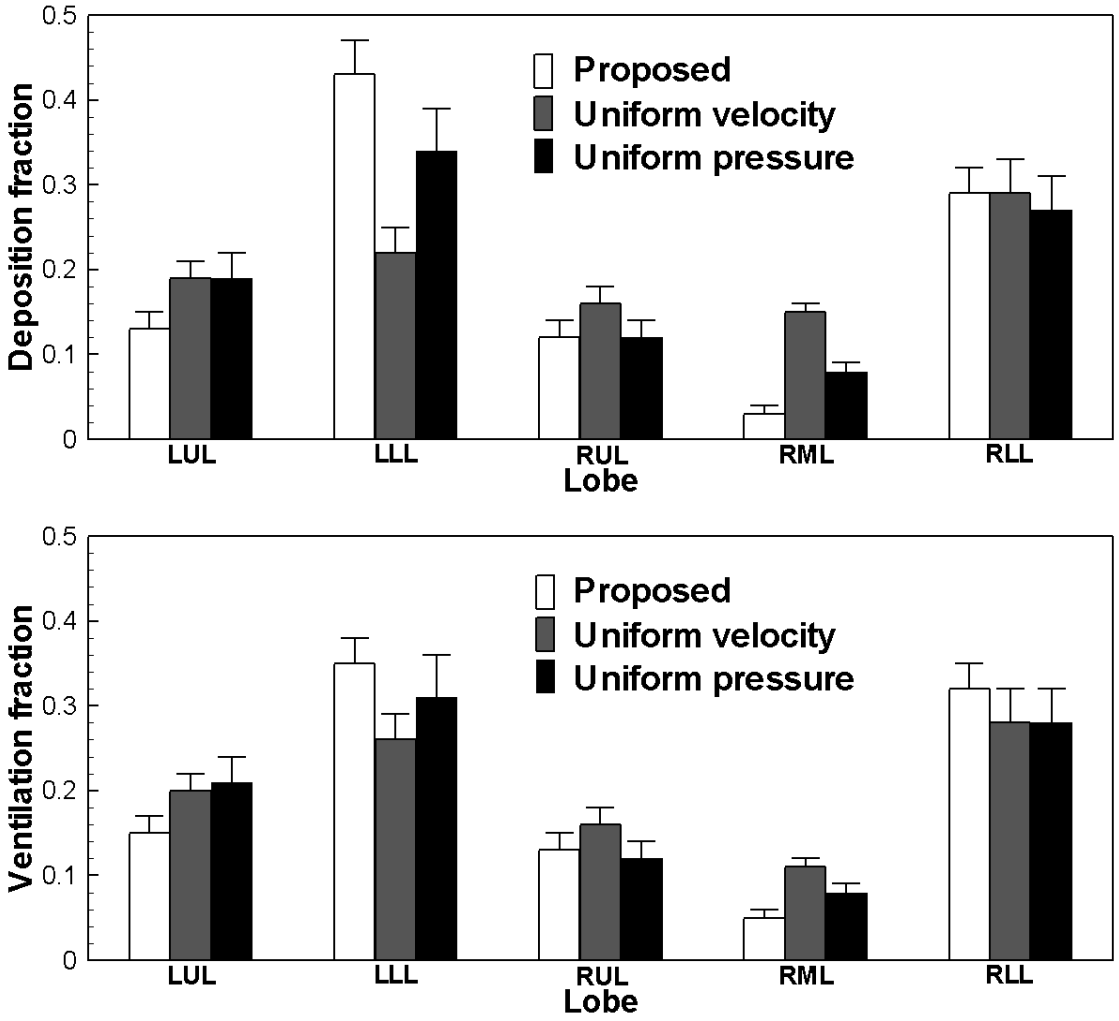

Figure 4.8: Lobar distribution of deposition fraction (top row) and ventilation fraction (bottom row) for the three cases with different outlet boundary conditions.

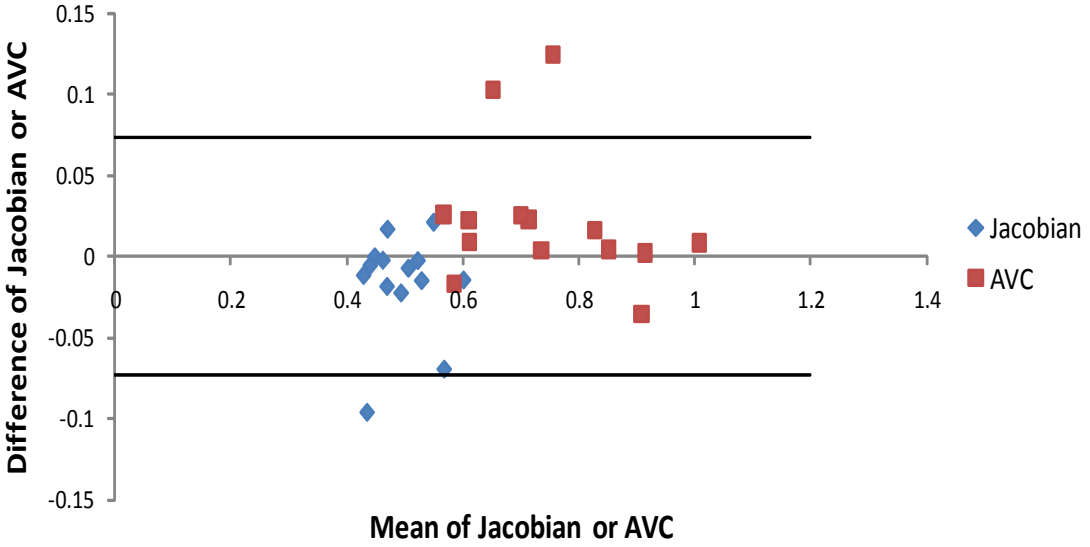

Figure 4.9: Bland-Altman plot of Jacobian and AVC between FRC1-TLC and FRC2-TLC registration. Solid line indicates upper and lower limits of agreement (2*S.D.).

CHAPTER 5
BREATHING LUNG MODEL

5.1 Introduction

We have previously demonstrated the ability to deform the airway geometry in Chapter 3 and to estimate the flow boundary condition in Chapter 4 from a pair of images acquired at two different levels of inflation. Since a linear interpolation is adopted in those studies, each node of the airway geometry is deformed along a straight-line trajectory and each outlet remained a constant flow rate ratio with time. In this chapter, we aim to integrate the approaches proposed in Chapters 3 and 4 to develop an MDCT-based dynamic, subject-specific lung model from three MDCT data sets acquired at different levels of inflation. A cubic spline interpolation is utilized to derive the nonlinear wall motion and time-varying boundary conditions. Such a dynamic lung model will then be constructed for CFD simulations.

5.2 Methods

5.2.1 Method Overview

Figure 5.1 shows a flow chart of the entire process. Three MDCT volumetric data sets are acquired at different levels of inflation in the same scanning session. Pair-wise mass-preserving image registration is then performed to match any two data sets to derive transform functions, defined as a voxel-by-voxel displacement. Meanwhile, segmentations of 3D CT-resolved airway and lobes of the image with the largest lung volume (the image I_1 in the figure) are obtained and are further used to generate a subject-specific 1D centerline airway tree using a volume filling

method. Each terminal bronchiole of the 1D airway tree is assumed to be associated with a specific cubic region inside the lungs, representing a pulmonary acinus. The registration-derived transform functions are then respectively used to deform the airway geometry segmented from the largest lung volume into the domains of other two lung volumes, establishing the correspondence of the airway geometries. In addition, air volumes inside each "acinus" associated with a terminal bronchiole in all three lung images are estimated with intensity-based air fractions along with registration-derived Jacobian values. Interpolations are then adopted to derive the moving airway geometries and time-varying changes in air flows associated with terminal bronchioles. Subject-specific boundary conditions for the 3D CT-resolved central airways at the instant are produced based on air flows associated with 1D terminal bronchioles by utilizing the connectivity information between the 3D airway and the associated downstream 1D airway trees. Thus, the dynamic lung model with the moving airway geometry and physiological boundary conditions can be constructed for CFD simulations.

5.2.2 MDCT Image Acquisition

A normal human subject (non-smoker, white non-Hispanic, 20-year old, male) is used in this study. Subject lay supine and breathed through a mouthpiece during the scanning session. The lung volume was well-controlled during the scanning session with a lab-developed volume controller system and three static volumetric images were acquired during breath-holds at 20%, 60% and 80% of vital capacity (VC), denoted by I_1, I_2 and I_3, respectively. The scans were performed with the following settings for a Siemens Sensation 64-slice MDCT scanner (Forchheim, Germany): 120kV, 75mAs, 0.75 mm slice thickness, 500 mm field of view. The protocol

was approved by the University of Iowa's Institutional Review Board. Each data set consists of 645-772 slices with a spacing of 0.5 mm and a reconstruction matrix of 512 $\times$ 512 pixels. In-plane pixel spatial resolution is 0.65 $\times$ 0.65 mm^2. All data sets are processed using a software package Pulmonary Workstation 2 (PW2: VIDA Diagnostics, Coralville, Iowa) to segment the lungs, lobes and central airways. The segmented airways are further skeletonized to obtain the centerlines of individual branches.

5.2.3 Image Registration

Pair-wise image registrations are performed to match any two images to derive transform functions. For each registration pair, a mass-preserving registration algorithm is adopted. This registration method uses the sum of squared local tissue volume difference (SSTVD) as the dissimilarity measure to account for changes in image intensities due to lung inflation [128–130]. The transform function is described by a composite operation of multi-level B-splines and a sufficient condition is imposed to ensure a one-to-one mapping even for a registration pair with large volume difference. Parameters of the transform function are optimized by a limited-memory, quasi-Newton minimization approach in a multi-resolution framework. In registering two images, one image is used as the reference image and the other is the floating image. An optimal transform function, which is defined in the domain of the reference image, is obtained after the registration. The resulting transform function can be used to transform the floating image into the reference image domain from an Eulerian viewpoint, obtaining the warped image. And it can also be used to deform any meshes in the reference image into the floating image domain from a Lagrangian viewpoint. The difference of viewpoints in transforming image and

mesh is because an image is defined in a discrete domain while a mesh is defined in a continuous domain. In the following sections, for simplicity we will use the words "warped" and "deformed" to distinguish the transformed image and mesh.

With the pair-wise registration, the transform function $\mathbf{T}_{12}$ is obtained from the registration pair I_1–I_2 with I_1 as the reference image and I_2 as the floating image, and $\mathbf{T}_{23}$ is from the registration pair I_2–I_3 with I_2 as the reference image and I_3 as the floating image. An composite operation of $\mathbf{T}_{12}$ and $\mathbf{T}_{23}$ is then set as a start point for the registration pair I_1–I_3, which has the maximum deformation, to obtain the transform function $\mathbf{T}_{13}$.

5.2.4 Moving Airway Geometry

Although 3D MDCT-derived airway geometries can be segmented for all three images, they provide no correspondence information and cannot be used for interpolations. With image registration, we can transform the airway segmented from the image I_1 into the domains of images I_2 and I_3 to obtain the deformed airways at I_2 and I_3 using the transform functions $\mathbf{T}_{12}$ and $\mathbf{T}_{13}$, respectively. The segmented I_1 airway, the deformed airways at I_2 and I_3 have the same node and connectivity information, thus providing the correspondence information for interpolation. In addition, the deformed airway will be compared against the airway segmented from the corresponding image to ensure the accuracy of the mapping.

In order to perform CFD simulation with a moving geometry, intermediate geometries have to be derived from these three base geometries by interpolation. Since the images are statically acquired during breath-holds, the time information has to be artificially modeled. In this work, we assume that the lung motion is correlated with the respiratory breathing curve. The time information for each image

is extracted based on the normalized lung volume and also by assuming that the image I_1 corresponds to the beginning of exhalation and I_3 corresponds to the beginning of inspiration. Figure 5.2 shows changes in the normalized inhaled air flow rate (negative denoted for exhalation) and lung volumes with time in one breathing cycle. The curve starts from the beginning of exhalation. The three imaged lung volumes are marked in the breathing curve and the corresponding time information $(t_1, t_2, \cdots, t_N)$ can be extracted for the following interpolations. A simple linear interpolation method has been previously used to derive intermediate airway geometry from two volumetric images with a straight-line trajectory assumption. However, it would not be suitable for three images or more since the C_1 discontinuities at the intersections of two segments would result in high discontinuities in the pressure solution. Higher order interpolations on the other hand may lead to overshoot at the intermediate phases and also involve the solution of an additional equation system for each vertex. To alleviate these issues we use a constrained cubic-spline interpolation method, which combines the smooth curve characteristics of spline interpolation and the non-overshooting behavior of linear interpolation [52]. An additional benefit of the constrained cubic-spline interpolation is that the resulting trajectory exactly passes all the base geometries. With the interpolation, airway geometry at an intermediate phase is independently calculated for each vertex.

5.2.5 Time-Varying Boundary Conditions

In Chapter 4, we have shown that subject-specific boundary conditions could be estimated for the 3D MDCT-derived central airway from a pair of lung volumes in

a 3D and 1D coupling framework, in which the 1D airway model serves as a link between 3D central airway and lung parenchyma. Although it provides physiologically-meaningful boundary conditions and CFD simulation shows improved results, the outlets remain constant flow rate ratios during breathing, not sufficient to describe the non-linear regional ventilation with time. In this chapter, we extend the approach by using three lung volumes.

The current 1D airway model is generated using the volume filling method proposed by Tawhai et al. [105]. It takes the lobes as "boundary conditions" and the skeleton of the 3D MDCT-resolved central airway tree as "initial conditions". The lobes are first filled with a group of uniformly distributed seed points, where each seed point corresponds to a region approximately representing a pulmonary acinus. The location of the seed points is defined at the largest lung volume (the image I_1 in this work) with the assumption that the lung is uniformly expanded. The number of seed points is approximately equal to the expected number of terminal bronchioles (30,000), which also determines the size of each acinus (roughly equal to the lung volume divided by 30,000). For the subject used in this work, the total lung volume of the image I_1 is 6.08 $liters$ and the size of each acinus is approximately 200 mm^3. The algorithm then works recursively by associating the seed points with the nearest peripheral branch in the respective lobe, calculating the center of mass of each group of seed points, splitting each group into two using the plane defined by the "parent" branch and the group's center of mass, and then creating branches that point towards the center of mass of the two-point groups. A generated branch is declared as a terminal bronchiole if it is shorter than a user-defined limit or if it supplies only a single seed point.

Since each terminal bronchiole of the 1D airway tree is associated with a

specific cubic region of lung, it is reasonable to assume that change in air volume within each cube is equivalent to air flow for the corresponding terminal bronchiole. With the image registration, we can track the air volume within each cubic region across the three image domains. Let Ω_a denote an acinus region in the lung volume I_1. The air volumes inside Ω_a at three lung data sets could then be estimated from intensity-based air fractions along with registration-derived local Jacobian values as follows:

$$\begin{aligned}
\text{air}\mathrm{V}_1 &= \sum_{\mathbf{x}\in\Omega_a} V_1(\mathbf{x})\,\gamma_{\text{air}}\left(I_1(\mathbf{x})\right) \\
\text{air}\mathrm{V}_2 &= \sum_{\mathbf{x}\in\Omega_a} J_{\mathbf{T}_{12}}(\mathbf{x}) V_1(\mathbf{x})\,\gamma_{\text{air}}\left(I_2(\mathbf{T}_{12}(\mathbf{x}))\right) \\
\text{air}\mathrm{V}_3 &= \sum_{\mathbf{x}\in\Omega_a} J_{\mathbf{T}_{13}}(\mathbf{x}) V_1(\mathbf{x})\,\gamma_{\text{air}}\left(I_3(\mathbf{T}_{13}(\mathbf{x}))\right)
\end{aligned} \tag{5.1}$$

where V_1 is the volume of a voxel in image I_1 and $\gamma_{\text{air}}(I)$ is the air fraction, a function of the intensity value I. Jacobian values $J_{\mathbf{T}_{12}}$ and $J_{\mathbf{T}_{13}}$ reflect the volume contraction/expansion relative to I_1 and can be calculated from $\mathbf{T}_{12}$ and $\mathbf{T}_{12}$, respectively.

Similarly, with the constrained cubic interpolation, we can derive the air volume within the same acinus region at any intermediate steps, thus obtaining changes in air volume associated with each terminal bronchiole. Subject-specific and time-varying boundary conditions for the 3D CT-resolved central airways at the instant can then be produced based on the air volume changes associated with 1D terminal bronchioles by utilizing the connectivity information between the 3D airway and the downstream 1D airway branches.

5.3 Results

5.3.1 Registration Accuracy

Figure 5.3 shows the visual comparison of a sagittal section from (a) the image I_1, (b) the warped image of I_2, and (c) the warped image of I_3 at the same axial location. The sagittal sections are oriented such that the diaphragm is at the bottom, the dorsal surface (nearest the scanner table) is on the right and the ventral surface is on the left. In addition, sections from the original images I_2 and I_3 at the same axial location are also shown in (d) and (e), respectively, for reference. All panels (a)-(e) have the same heights and widths. It is clear to see that the warped images (b) and (c) have good anatomic correlations with (a), showing that registrations are able to recover the deformations among the three original images.

5.3.2 Moving Airway Geometry

Figure 5.4 shows 3D airway geometries segmented from the three lung volumetric images: Red for I_1 (80% VC), green for I_2 (60% VC), and blue for I_3 (20% VC). We can see that the airway geometry deforms with changes in lung volumes, further demonstrating the importance of performing CFD simulation with a compliant airway geometry. As the lung volume decreases, the lengths of the branches become shorter and the airways contract towards the apex, which results in smaller airway volume.

To further demonstrate that the registration is capable of recovering the deformation of the airway geometries, we compare the airways directly segmented from I_2 and I_3 against the airways that are deformed from I_1 by using transform functions $\mathbf{T}_{12}$ and $\mathbf{T}_{13}$, shown in Figures 5.5 and 5.6, respectively. In Figure 5.5

(a), the airway of I_2, shown in green, is superimposed over the deformed airway at I_2, shown in pink. Figures 5.5 (b) and (c) present the comparisons between the two geometries at two selected cross-sections, where the extracted curves from the airway of I_2 are shown in green and the ones from the deformed airway are shown as pink dots. Curves extracted from the undeformed airway geometry of I_1 at those two cross-sections are shown in red as a reference. In Figure 5.6 the airway of I_3 is shown in blue and the deformed airway at I_3 is shown in orange. Similar to Figures 5.5(b) and (c), Figures 5.6(b) and (c) show the comparisons of the extracted curves from the airway of I_3 (blue) and the deformed airway (orange dot) at the two cross-sections, respectively. The undeformed airway geometry of I_1 is also shown in red. These comparisons clearly indicate that the deformed airways obtained from image registrations match well with the airways segmented from the images, further proving the registration accuracy. More importantly, the deformed airways are obtained by applying the transform functions onto the I_1 airway; thus, they all have the same node and connective information, establishing the correspondences among the three domains. The I_1 airway, deformed airway at I_2, and deformed airway at I_3 can then used as the base geometries for interpolations.

As discussed above, the normalized lung volume is used to extract the time information for interpolation. The lung volumes estimated from the segmented lung masks for the three images are 6.08, 5.40 and 3.75 (liters), respectively. Based on the breathing curve, we can extract the time information in one breathing cycle. With both the time information and the correspondences built from image registration, we could derive the dynamic airway geometry with changes in lung volumes.

Owing to the constrained cubic spline interpolation, trajectories of the airway

geometry exactly pass the base geometries and C_1 continuity of each path is guaranteed. By contrast, a linear interpolation would lead to C_1 discontinuities at the intersections of two segments, which would result in high discontinuities in the pressure solution during simulation. In addition, the dynamic model derived from the three lung volumes here should track the lung motion more precisely by comparing against the one derived from two lung volumes. A nonlinear interpolation can be utilized with the three lung volumes while only a linear interpolation is available with the two lung volumes. It is obvious that a nonlinear interpolation is more suitable since the lung motion is nonlinear in nature. To demonstrate the insufficiency of a linear interpolation, we calculate the interpolated airway at 60%VC using the linear interpolation between the two lung volumes I_1 and I_3 and show it (in gray) in Figure 5.5. It is clear to see the differences between the interpolated airway at 60%VC and the undeformed airway of I_2.

5.3.3 Time-Varying Boundary Conditions

Figures 5.7(a) and (b) show the generated 1D centerline airway tree from coronal and sagittal views, respectively. The 3D MDCT-resolved central airway is also shown for reference. In addition, Strahler-order-based log plots of number of branches and mean length for the generated 1D model are shown in Figure 5.8. Both plots show log-scaled linear trends, consistent with existing morphometric analysis of the human bronchial tree.

The distributions of air volume associated with each terminal bronchiole are shown in Figures 5.9(a)-(c) for the three imaged lung volume from a sagittal view. The unit of air volume is mm^3. In Figure 5.9(a) air volume is uniformly distributed in the whole lung while in Figure 5.9(b) the dependent region (dorsal region) has

less air volume than the ventral region. In Figure 5.9(c) air volume dramatically decreases since the total lung volume decreases by 2.33 liters from I_1 to I_3. In addition, the gravitational oriented gradient with less air volume in the dependent region also exists. All these observations follow well recognized physiology of ventilation in subjects positioned in the supine body posture [73]. For I_1, the lung volume is close to total lung capacity and all alveoli inside the lungs are close to full expansion, thus leading to uniform air volume distribution. When air is exhaled from the lungs, due to the motion of diaphragm and the effects of gravitation, the dorsal region collapses more than the ventral region so that less air is left in the dorsal region, forming the ventral-dorsal gradient. These can also be used to explain the distribution of air volume change shown in Figure 5.10. The air volume change ($d\mathrm{AirV}_i$) is calculated relative to the image I_1 by $d\mathrm{AirV}_i = \mathrm{airV}_i - \mathrm{airV}_1$ with $i = (1, 2, 3)$ and it reflects air flow for each terminal bronchiole. The non-uniform ventilation patterns are clearly indicated from these results.

The air volume associated with each terminal bronchiole at any intermediate step can then be derived from the three states by interpolation and the corresponding air volume change ($d\mathrm{AirV}_t$) can be calculated. Thus, air flow associated with each terminal bronchiole at an intermediate phase is obtained and can be passed to describe flow boundary conditions for the 3D CT-resolved central airways at any instant in the 3D-1D coupling framework. Again, owing to the high order interpolation, the boundary conditions vary with time. To illustrate the time-varying air flow, Figure 5.11 presents the curves for four selected locations inside the lungs. The locations are marked with spheres in different colors and the curves of air flows at the four locations are plotted in the same colors as the corresponding locations. It shows that air flow associated with terminal bronchioles changes with time, in

a nonlinear way, and also changes with location in lungs, showing the non-uniform pattern. At an instant, we can see that air flow is greater in the dorsal region while smaller in the ventral region, further demonstrating the well-recognized ventral-dorsal gradient in subjects positioned in the supine body posture [73].

5.3.4 Dynamic Lung Model

By combining the moving airway geometry and the time-varying boundary conditions, we can obtain the dynamic lung model. The four panels shown in Figure 5.12 correspond to four different time points in a breathing curve (a: $t = 0$; b: $t = T/6$; c: $t = T/3$; d: $t = T/2$, with T as the period), where (a) and (d) correspond to the lung volumes I_1 and I_3, respectively. The motion of the airway geometry and the non-uniform regional ventilation are clearly indicated.

5.4 Discussion

In this chapter, we described a technique to build a dynamic lung model from three MDCT volumetric data sets acquired at different inflation levels. Pair-wise mass-preserving image registration was performed to match any two data sets to derive transform functions. The transform functions were then used to deform the airway geometries to establish correspondence for interpolation. Comparisons between the deformed airways and the targets show good agreement. In addition, air volumes for lung parenchyma at three inflation levels were estimated with intensity-based air fractions along with registration-derived Jacobian values. Airway geometry and local air volume map at any intermediate phases during breathing cycles were derived by utilizing a constrained cubic spline interpolation. Boundary conditions for the 3D MDCT-resolved central airways at any instants were then produced based

on regional air volume map in a 3D-1D coupling multi-scale framework. Compared against two lung volumes, a nonlinear interpolation can be utilized for three lung volumes to account for the nonlinear geometry motion and time-varying boundary conditions during breathing. Work is ongoing to apply the dynamic lung model for CFD simulations. Since the airway motion and regional ventilation are derived from MDCT images, the lung model is subject-specific. With the prescribed motion of the airway geometry, CFD simulation could be performed using the moving meshes to study effects of wall motion on flow structures. In addition, the time-varying boundary conditions derived from three lung volumes account for the nonlinear and non-uniform ventilation during breathing. Investigation on the effects of non-linear and non-uniform ventilation on flow patterns will be an interesting study.

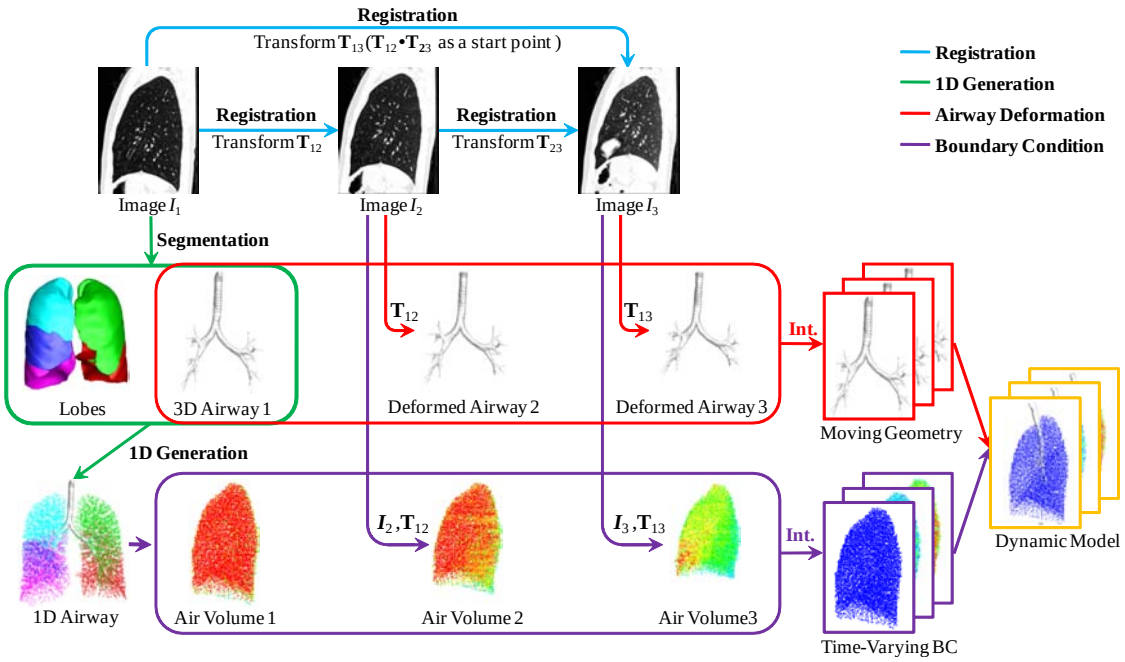

Figure 5.1: A flow chart of the entire process to develop the breathing lung model.

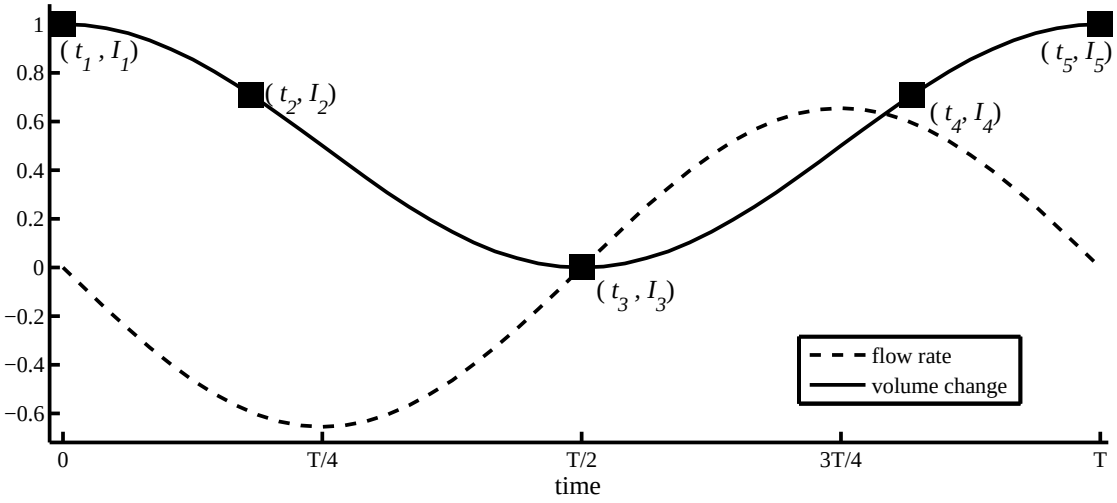

Figure 5.2: Changes in normalized inhaled air flow rate and lung volume with time during a breathing cycle. Locations of the imaged lung volumes are marked on the curve.

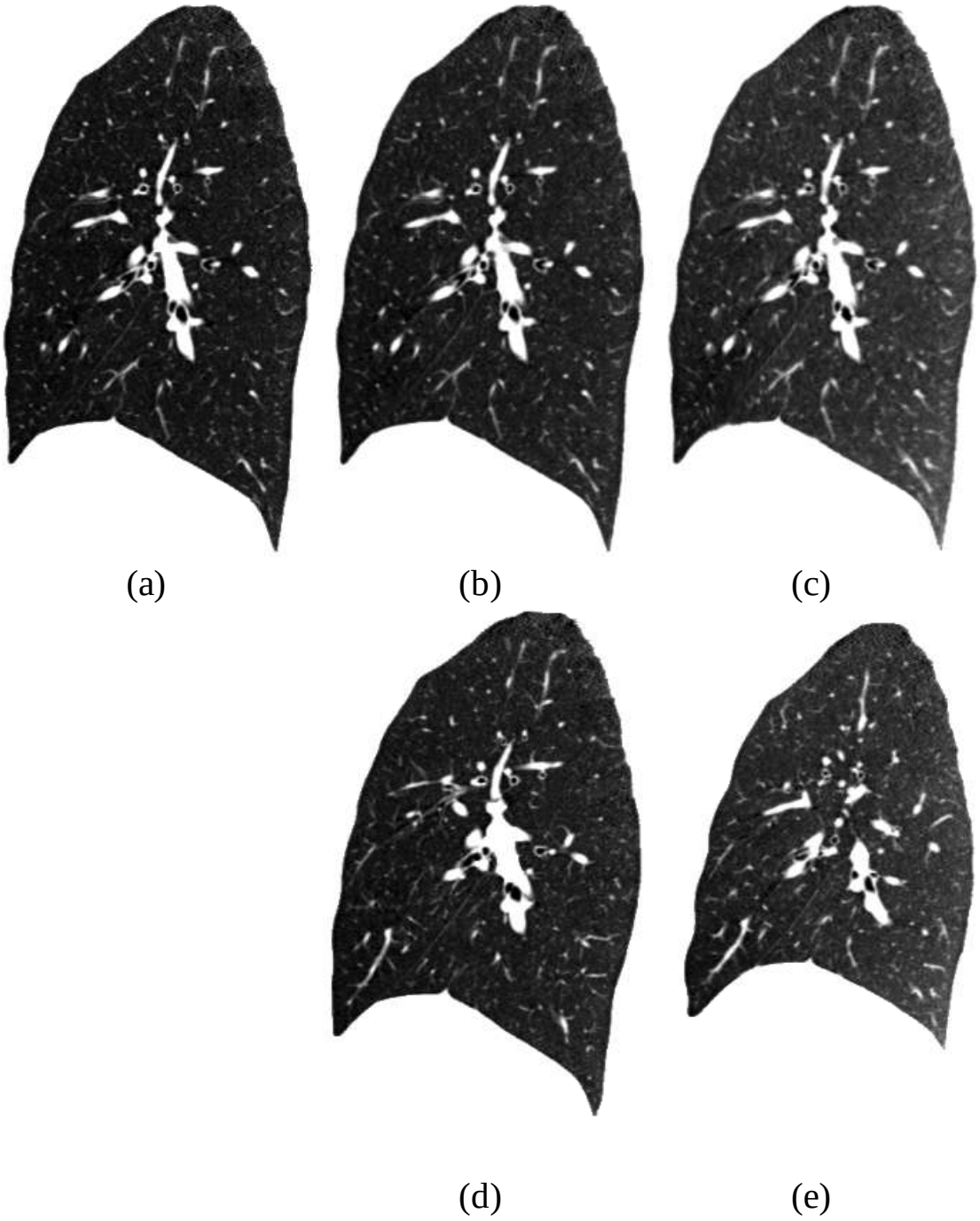

Figure 5.3: Visual assessment of registration accuracy. A sagittal slice from (a) the image I_1, (b) the warped image of I_2, (c) the warped image of I_3, (d) the image I_2, and (e) the image I_3 at the same axial locations, respectively. All panels have the same sizes.

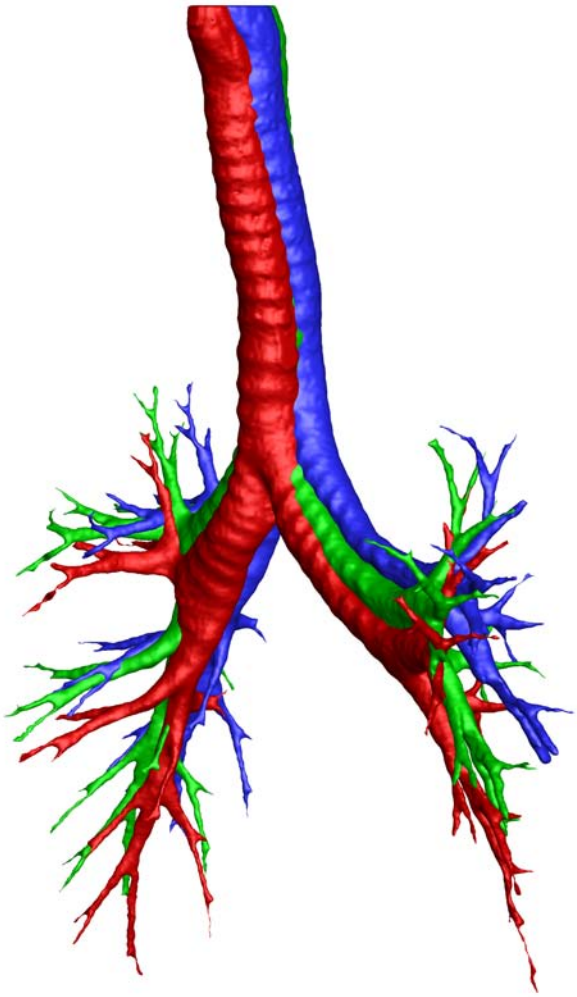

Figure 5.4: 3D MDCT-derived airway geometries segmented from the three lung volumetric images: Red for I_1 (80% VC), green for I_2 (60% VC), and blue for I_3 (20% VC).

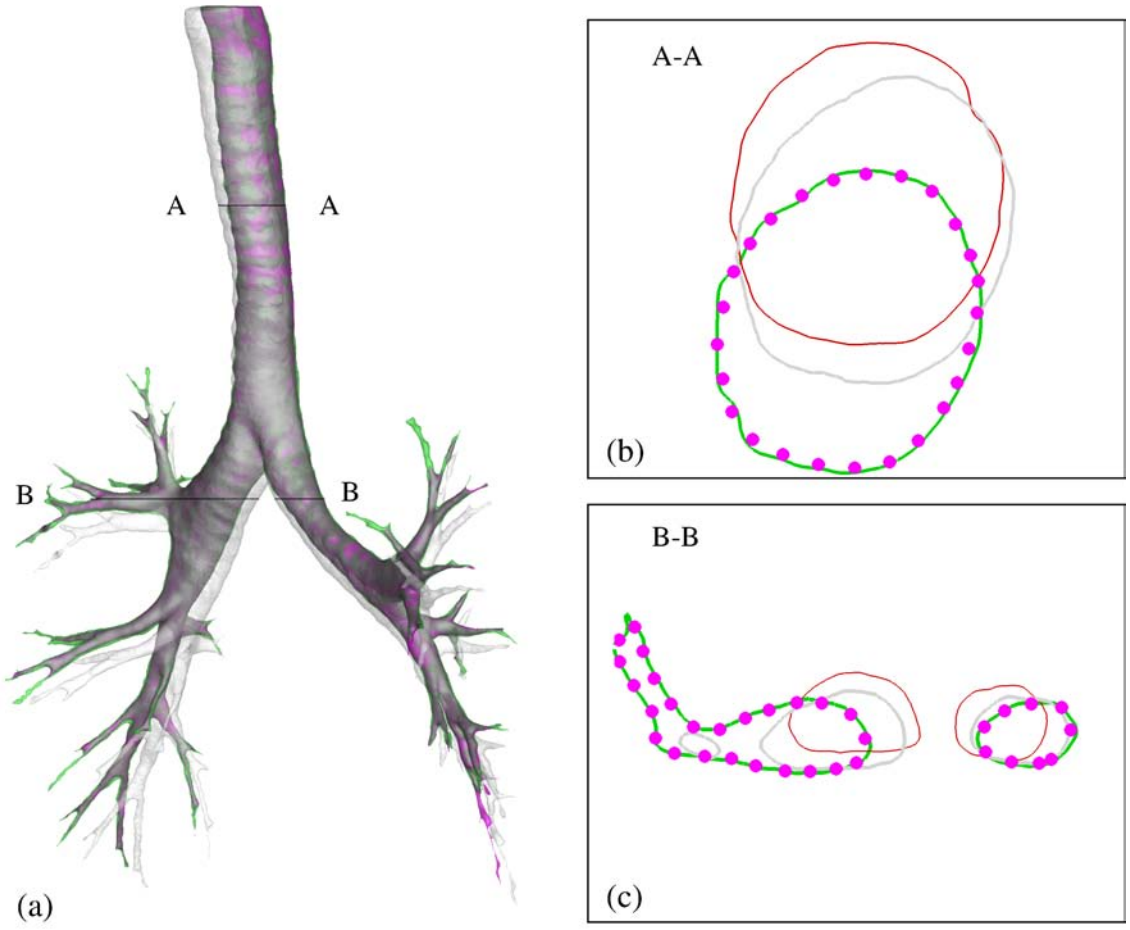

Figure 5.5: Comparison between the segmented airway from I_2 (60% VC) and the airway deformed from I_1 with the transform function $\mathbf{T}_{12}$: (a) whole airway from I_2 (green) and the deformed airway (pink); (b) the extracted curves from the I_2 (green) and from the deformed airway (pink dot) at a cross-section in the middle of trachea; (c) the extracted curves from the I_2 (green) and from the deformed airway (pink dot) at a cross-section after the carina. The undeformed airway geometry from I_1 at those two cross-sections are shown in red in both (b) and (c). In addition, an interpolated airway at 60%VC using the linear interpolation between the two lung volumes I_1 and I_3 is also shown in gray (surface or curves) to demonstrate the insufficiency of the linear interpolation.

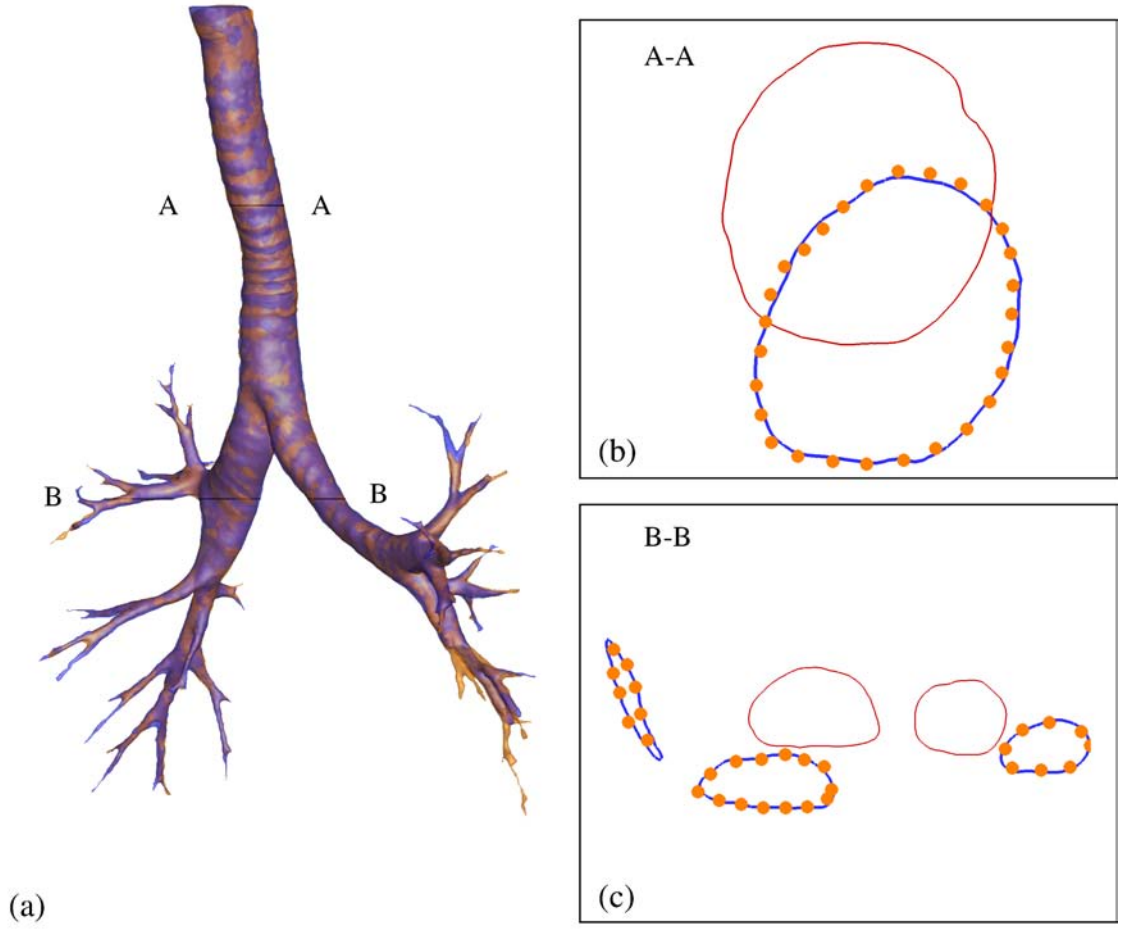

Figure 5.6: Comparison between the segmented airway from I_3 (20% VC) and the airway deformed from I_1 with the transform function $\mathbf{T}_{13}$: (a) whole airway from I_3 (blue) and the deformed airway (orange); (b) the extracted curves from the I_3 (blue) and from the deformed airway (orange dot) at a cross-section in the middle of trachea; (c) the extracted curves from the I_3 (blue) and from the deformed airway (orange dot) at a cross-section after the carina. The undeformed airway geometry from I_1 at those two cross-sections are shown in red in both (b) and (c).

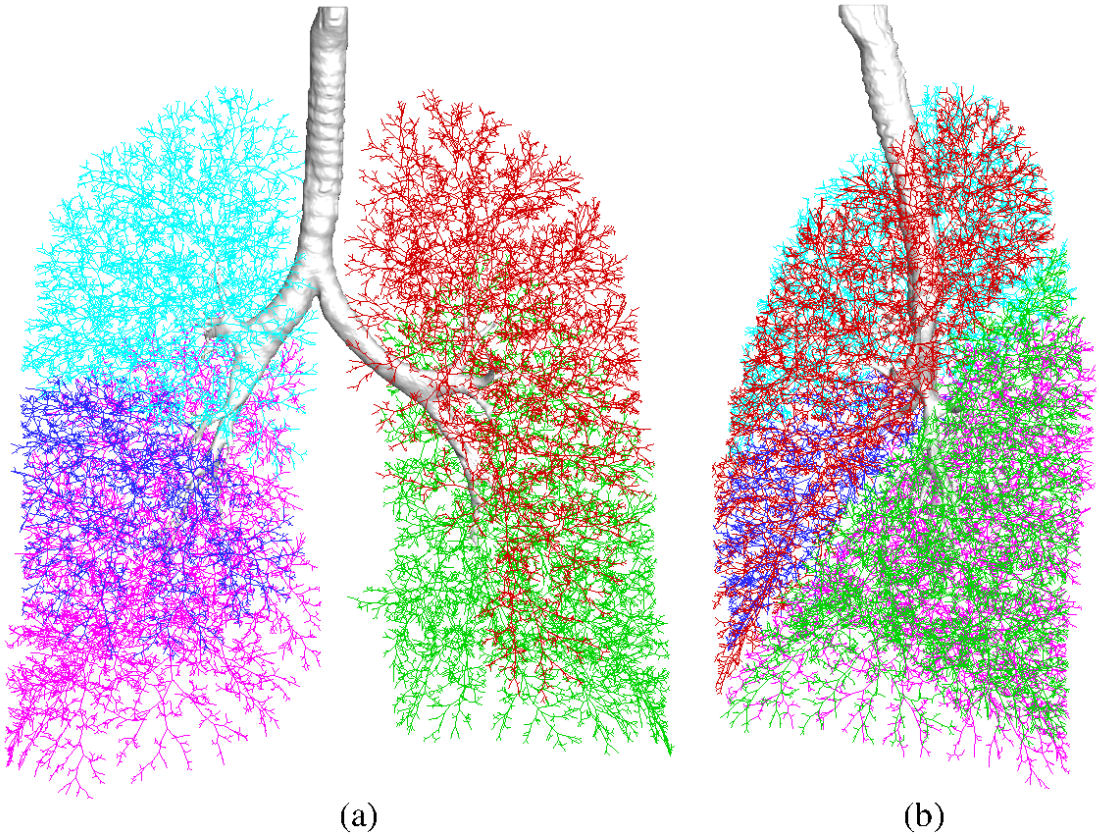

Figure 5.7: 3D MDCT-resolved airway and generated 1D centerline airway from two views: (a) coronal and (b) sagittal. The generated airways are shown in different colors for each lobe: red for left upper lobe (LUL), green for left lower lobe (LLL), cyan for right upper lobe (RUL), blue for right middle lobe (RML) and pink for right lower lobe (RLL).

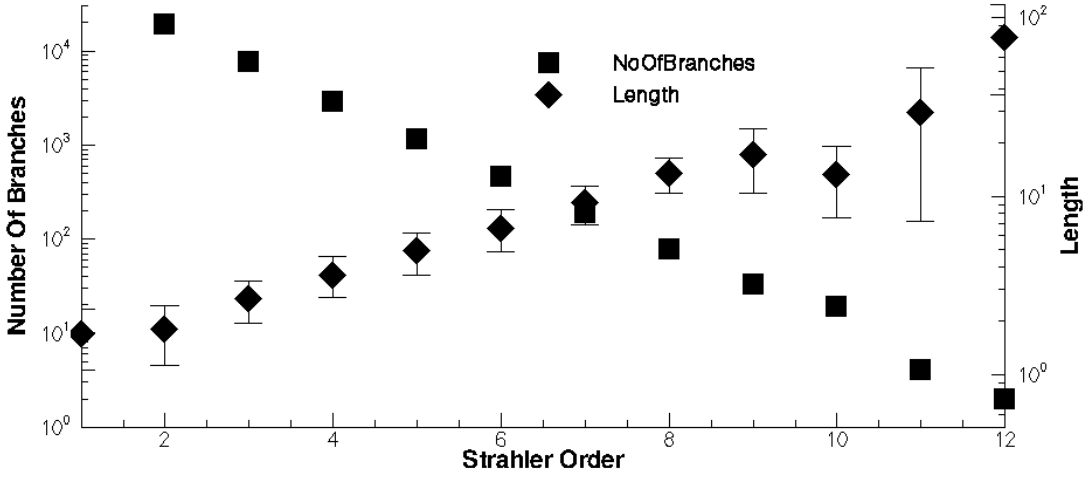

Figure 5.8: Strahler-order-based log plots of number of branches and mean length for the generated 1D model. Both plots show log-scaled linear trends, consistent with existing morphometric analysis of the human bronchial tree.

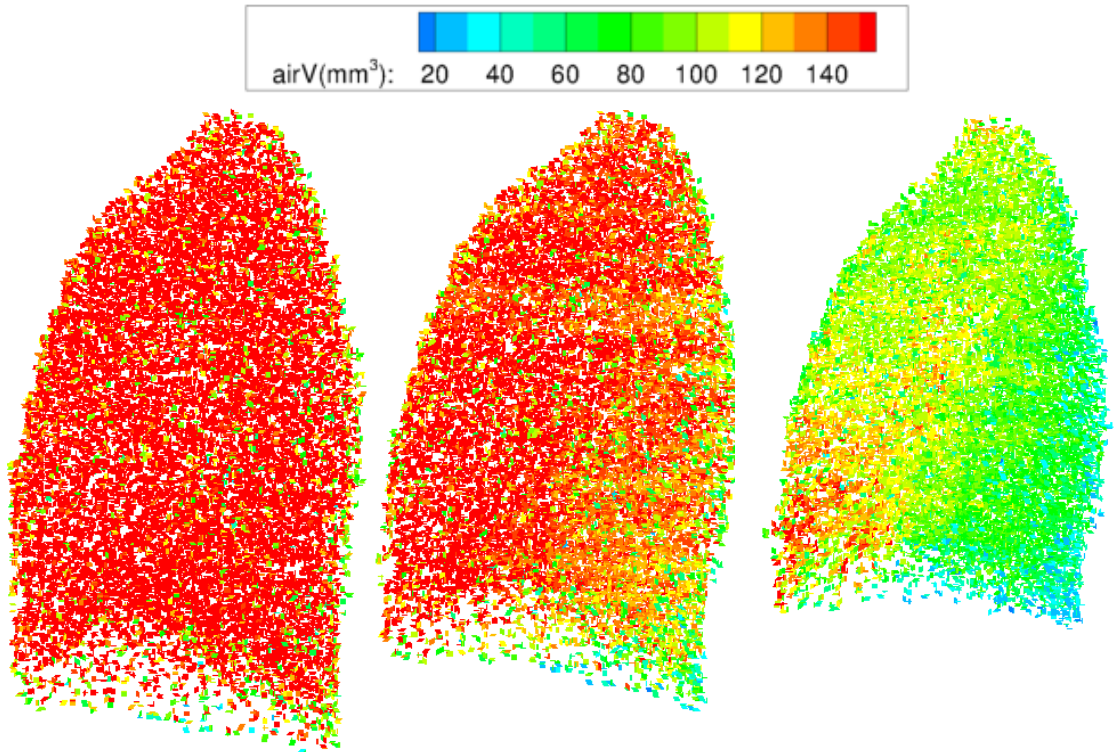

Figure 5.9: The distributions of air volume associated with each terminal bronchiole for three data sets: (a) I_1, (b) I_2 and (c) I_3. The unit is mm^3.

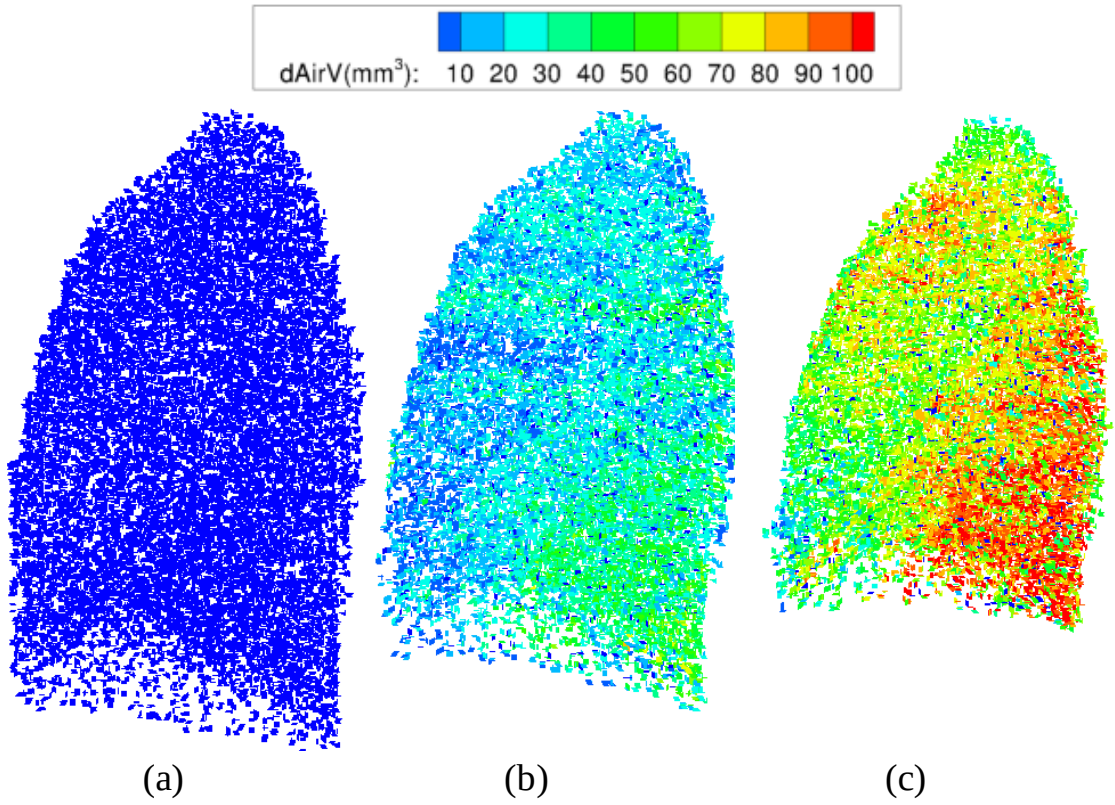

Figure 5.10: The distribution of the air volume change associated with each terminal bronchiole for three data sets: (a) I_1, (b) I_2 and (c) I_3. The unit is mm^3. The air volume changes are calculated relative to the image I_1 and reflect the air flow associated with each terminal bronchiole.

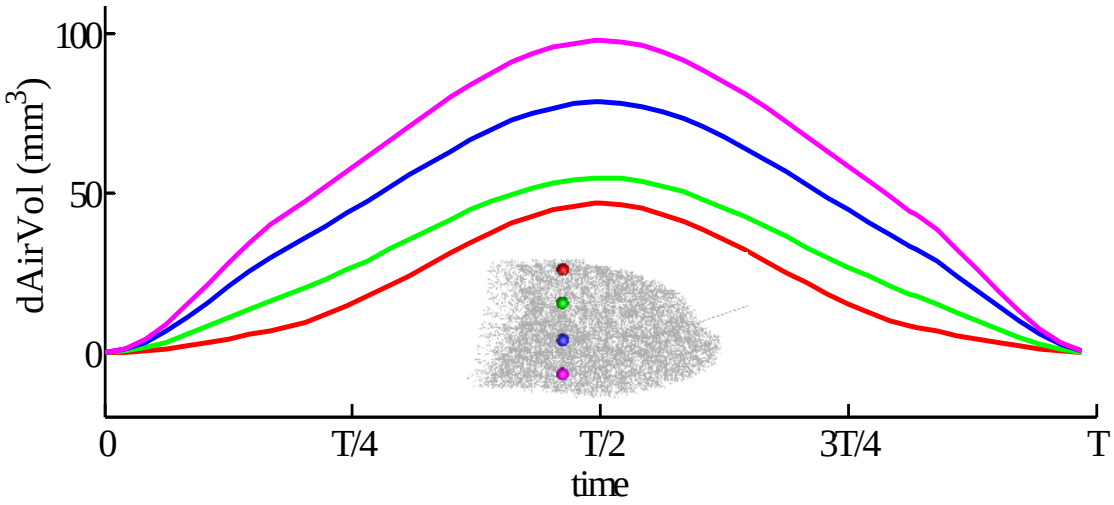

Figure 5.11: Time-varying air flows associated with terminal bronchioles for four selected locations in the lung. The locations are marked with spheres in different colors and the curves of air flows at the four locations are plotted in the same colors as the corresponding locations.

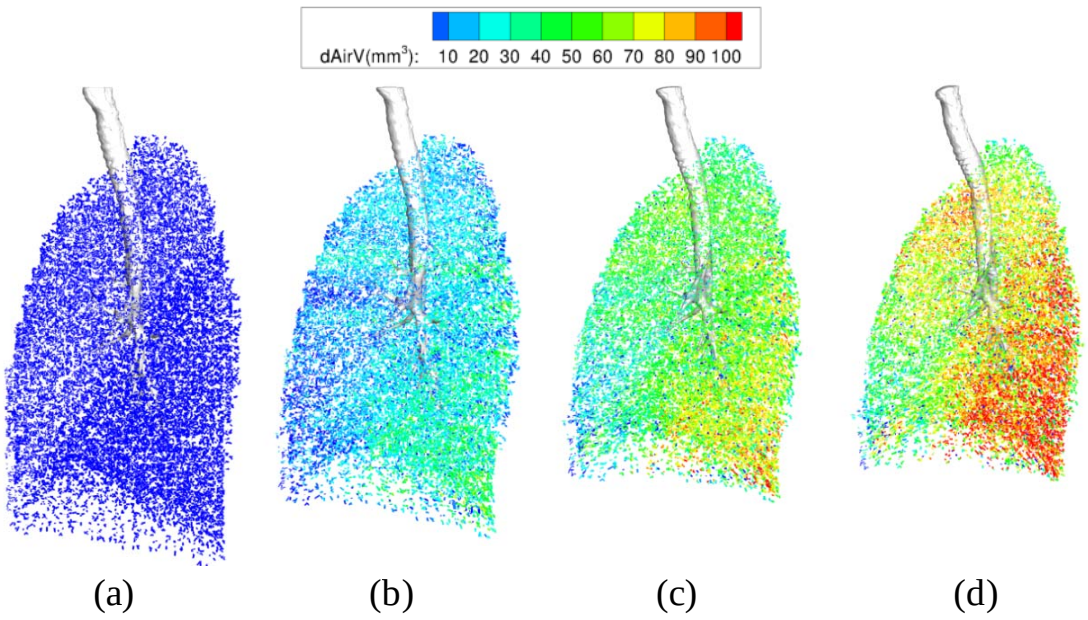

Figure 5.12: Moving airway geometry and air flow associated with terminal bronchioles extracted from the breathing lung model at four different time points in a breathing cycle: (a) t=0; (b) t=T/6; (c) t=T/3; (d) t=T/2, with T as the period. (a) and (d) correspond to the lung volume, I_1, and lung volume, I_3, respectively.

CHAPTER 6
SUMMARY AND FUTURE WORK

6.1 Summary

In this thesis, we develop MDCT-based dynamic, subject-specific lung model with realistic deforming airway geometries and physiologically meaningful boundary conditions and apply it for CFD simulation of air flow.

6.1.1 Mass-Preserving Nonrigid Registration

We first propose a novel nonrigid image registration approach to align CT-derived lung datasets acquired during breath-holds at different inflation levels when the image distortion between the two volumes is large. In contrast to the sum of squared intensity difference, a new similarity criterion, SSTVD, is introduced to take into account changes in reconstructed HU with inflation. This new criterion aims to minimize the local tissue volume difference within the lungs between matched regions, thus preserving the tissue mass of the lungs if the tissue density is assumed to be relatively constant. A composite of multilevel B-spline is adopted to deform images and a sufficient condition is imposed to ensure a one-to-one mapping even for a registration pair with large volume difference. Parameters of the transformation model are optimized by a limited-memory quasi-Newton minimization approach in a multiresolution framework. To evaluate the effectiveness of the new similarity measure, we perform registrations for six lung volume pairs. Over 100 annotated landmarks located at vessel bifurcations are generated using a semiautomatic system. The results show that the SSTVD method yields smaller average landmark

errors than the SSD method across all six registration pairs.

6.1.2 Moving Airway Geometry

We propose a new B-spline-based hybrid registration framework for pairs of lung CT datasets with large lung volume differences by incorporating anatomic landmark information and intensity patterns. A sequence of invertible B-splines is composed in a multiresolution framework to ensure local invertibility of the large deformation transformation and a physiologically meaningful similarity measure is adopted to compensate for changes in voxel intensity due to inflation. Registrations are performed using the proposed approach to match six pairs of 3D CT human lung datasets. Results show that the proposed approach has the ability to match the intensity pattern and the anatomical landmarks, and ensure local invertibility for large deformation transformations. Statistical results also show that the proposed hybrid approach yields significantly improved results as compared with approaches using either landmarks or intensity alone. By using the registration-derived deformation field we demonstrate the ability to develop a dynamic airway model.

6.1.3 Subject-Specific Boundary Conditions

A novel image-based technique is then presented to estimate a subject-specific boundary condition for CFD simulation of pulmonary air flow. The information of regional ventilation for an individual is derived by registering two CT lung datasets. And it is then passed to the CT-resolved airways as the flow BC within a 3D-1D couping framework, where the 1D airway model serves as a link between 3D central airway and lung parenchyma. The CFD simulations show that the proposed

method predicts lobar volume changes consistent with direct image-measured metrics, whereas the other two traditional boundary conditions (uniform velocity or uniform pressure) yield lobar volume changes and regional pressure differences inconsistent with observed physiology.

6.1.4 Breathing Lung Model

At last, we develop MDCT-based, subject-specific breathing lung models from three CT volumetric datasets with different inflation levels. Pair-wise mass-preserving image registration is performed to match any two datasets to derive transform functions. The transform functions are then used to deform the airway geometry and established correspondence for interpolation. Comparisons between the deformed airways and the targets show good agreement. In addition, regional air volumes for lung parenchyma at three inflation levels are estimated with intensity-based air fractions along with registration-derived Jacobian values. Airway geometry and regional air volume change map at any intermediate phase are then derived by a constrained cubic spline interpolation. Physiological boundary conditions for the 3D CT-resolved central airways at any instant are then produced based on regional air volumes. Compared against two lung volumes, a nonlinear interpolation can be utilized for three lung volumes to account for the nonlinear geometry motion and time-varying boundary conditions during breathing.

6.2 Future Work

The problems which need further investigation are discussed below.

6.2.1 Effects Of Airway Branching Patterns

It is well recognized that there are distinct variations in the human airway tree branching pattern. However, little is known about the role that such branching patterns may play in airflow dynamics including effects on inhaled particle deposition. With the established framework for the breathing lung model, it is now possible to compute airflow in physical domains that are anatomically accurate and subject specific, enabling inter-subject comparisons. Effects of airway branching patterns, ages, and gender on regional ventilation and flow dynamics could then be investigated.

6.2.2 Effects Of Gas Properties

The subject-specific boundary conditions are estimated based on local air volume changes obtained from non-contrast MDCT images with different inflation levels. Different gases, such as xenon, helium, have been used as agents for assessments of regional ventilation in medical imaging and also for enhancement of pharmaceutical drug aerosol delivery. However, those gases have different properties from air and not much is currently known about the effects of gas properties on flow structures, regional ventilation, and particle transport.

We have previously compared MDCT and MRI-based assessment of regional ventilation by using three normal non-smoking human subjects. For each subject, two volume-controlled MDCT scans were acquired at FRC and TLC and a volume-controlled HP ^{3}He static MRI scan was acquired at TLC. A mass preserving image registration algorithm was adopted to match both MDCT scans to estimate local air volume change (AVC), which is jointly estimated from changes in local air fraction along with the registration-derived Jacobian values. Registration-based ventilation

was then compared against the distribution map of HP 3He gas. The preliminary results have shown that the MDCT-based assessment and MRI assessment of regional ventilation are qualitatively similar, as in Figures 6.1 and 6.2. However, discrepancy can be observed in the ventral lung regions where MRI shows patches of much greater ventilation than MDCT, possibly arising from the gas density differences (helium 0.34 kg/m^3 vs. room air 1.2 kg/m^3), leading to higher ventilation of ventral lung portions in the HP ^{3}He MRI. These findings are consistent with previous CFD simulations of helium wash-in, which has shown the lighter gas is pushed towards the non-dependent regions [62]. It might be desirable to further investigate the effects of gas properties on regional ventilation. In addition, it is also be interesting to study such gas effects using MDCT. Different pairs of volumetric scans can be acquired with different gases (SF6, helium, air, respectively) and regional ventilation maps can be estimated by image registration. The estimated regional ventilation maps could then be used to describe boundary conditions for different gases, providing physiologically meaningful boundary conditions to investigate gas effects on flow structure and particle depositions.

6.2.3 Accounting For Lobar Sliding

It is well known that human lungs are separated into five lobes and lobes can slide against the chest wall and adjacent lobes [81]. However, most registration algorithms assume or imply a continuous and smooth deformation field, which might introduce unphysiological artifacts near object interfaces if the adjacent objects slip against each other. Thus, developing physiologically meaningful registration algorithms that account for discontinuities is becoming an important issue [23, 46, 89, 90, 124, 126].

Recently, we have proposed two approaches to account for discontinuities near lobar fissures. The first one is to register regions of interest (lobes in our cases) separately with segmentation masks [23]. Voxels outside of the region of interest are not taken into consideration during registration or are set to a uniform value before registration to form a high intensity contrast on the border. By this means this method avoids inter-object regularization and match corresponding borders with an implicit penalty of the high intensity contrast between object and "background". Once the registration is performed, lobar sliding is estimated by evaluating the relative displacement on both sides of the fissure. Figure 6.3 shows the displacement profile of the tangent component along a line perpendicular to the fissure surface at three different locations (near the apex, near the lingula and near the base) for both the whole-lung-based (square) and the lobe-based (circle) methods. It is clear to see increasing sliding (larger discontinuity) in the more basal positions when using the lobe-by-lobe analysis. However, these discontinuities are not apparent when using the lung-by-lung analysis.

Although such mask-based registration method accounts for lobar sliding, it requires a complete interface between two adjacent objects. Commonly, incomplete lobar fissures are observed in human lungs and the degree of incompleteness ranges from nearly complete absence to nearly complete presence of the fissure [69]. This means that lobes might be only partially separated and, thus, mask-based registration method would be incapable of dealing with incomplete fissures. A new registration algorithm was then proposed to deal with discontinuities near incomplete lobar fissures [131]. Discontinuities are accounted for by a spatially variable diffusive regularization. In addition, a distance penalty term is incorporated with the similarity term to explicitly match both intensity and interfaces. The new

method is evaluated using 2D synthetic examples with complete or incomplete "fissures", and results show that it is capable of capturing discontinuity of deformation in both normal and tangent directions, see Figure 6.4. An important next step is to apply the proposed method to datasets with both complete and incomplete fissures to investigate the influence of degree of fissure incompleteness on regional lung mechanics, which will help improve the breathing lung model.

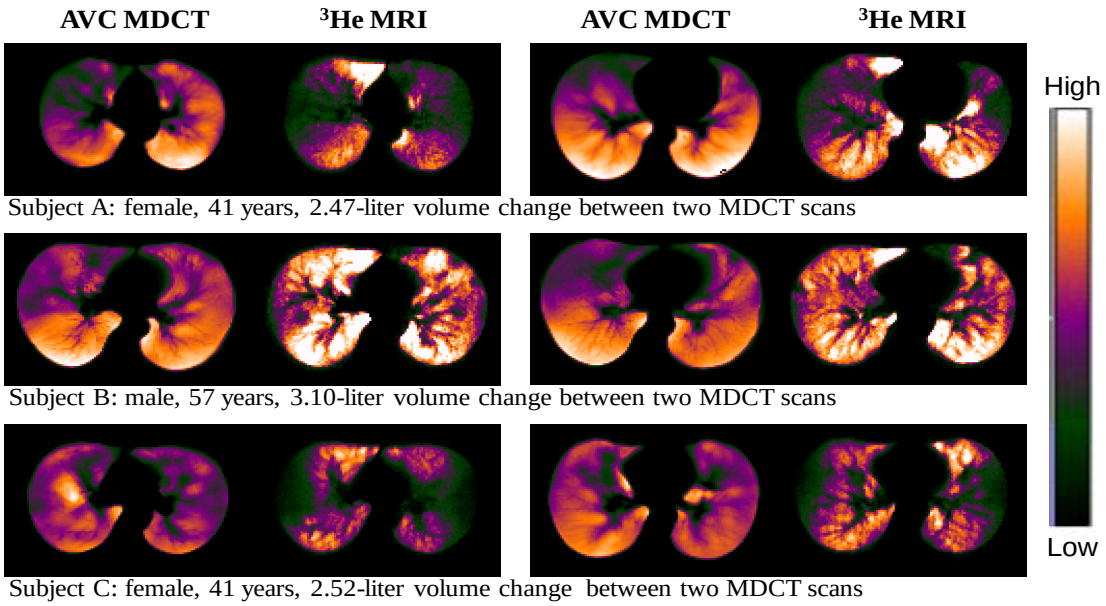

Figure 6.1: Comparisons between MRI-based ^{3}He distribution and MDCT-based AVC map for three subjects. Two transverse sections are shown for each subject.

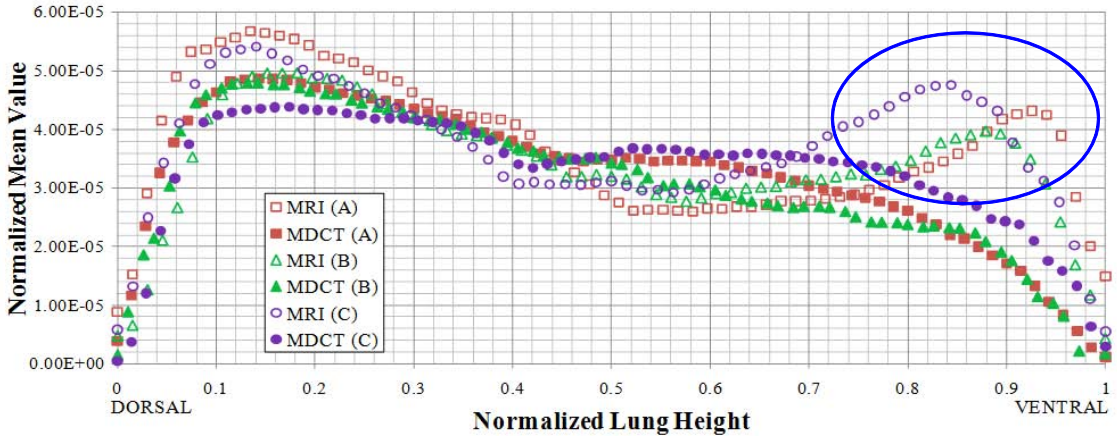

Figure 6.2: Normalized mean AVC or ^{3}He ventilation as a function of normalized lung height (dorsal-ventral) for three subjects. There are similar but not identical distribution patterns. 3He is consistently higher in the ventral lung regions (blue oval), possibly due to gas properties.

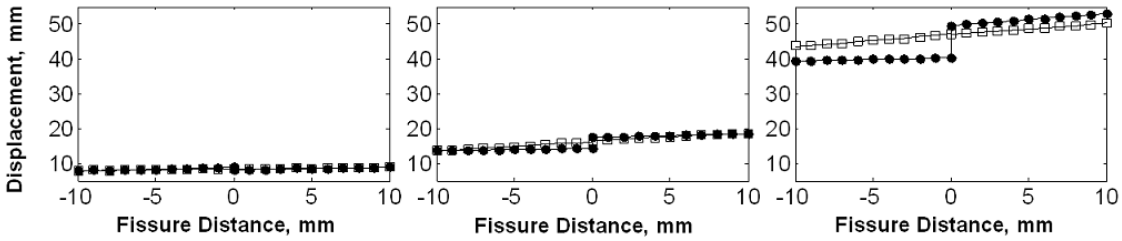

(a) Subject A with volume change = 3.2 Liters

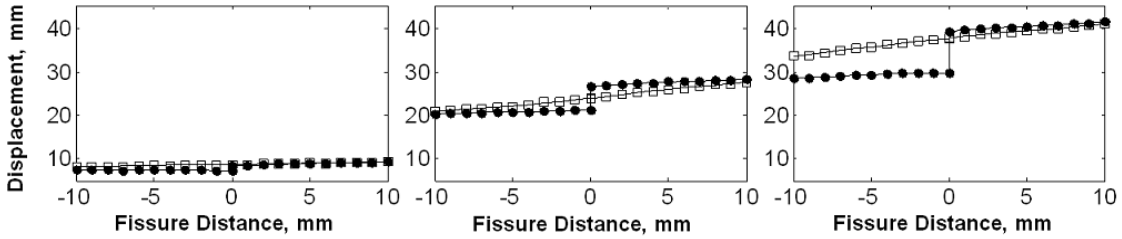

(b) Subject B with volume change = 2.3 Liters

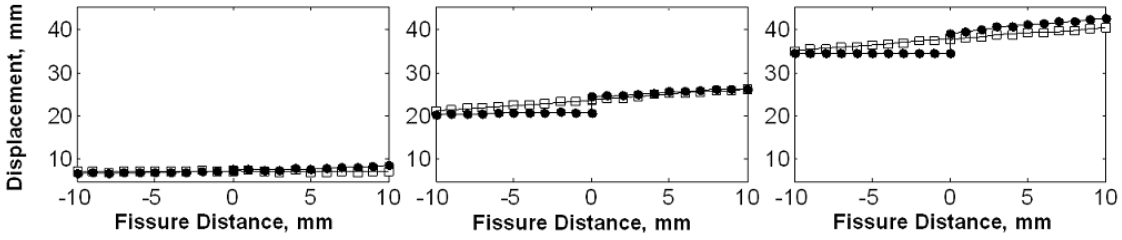

(c) Subject C with volume change = 2.4 Liters

Figure 6.3: Displacement profile of tangent components along a line perpendicular to the fissure surface at three different locations (left: near apex; middle: near lingula; and right: near base) for both the whole-lung-based (square) and the lobe-based (circle) methods.

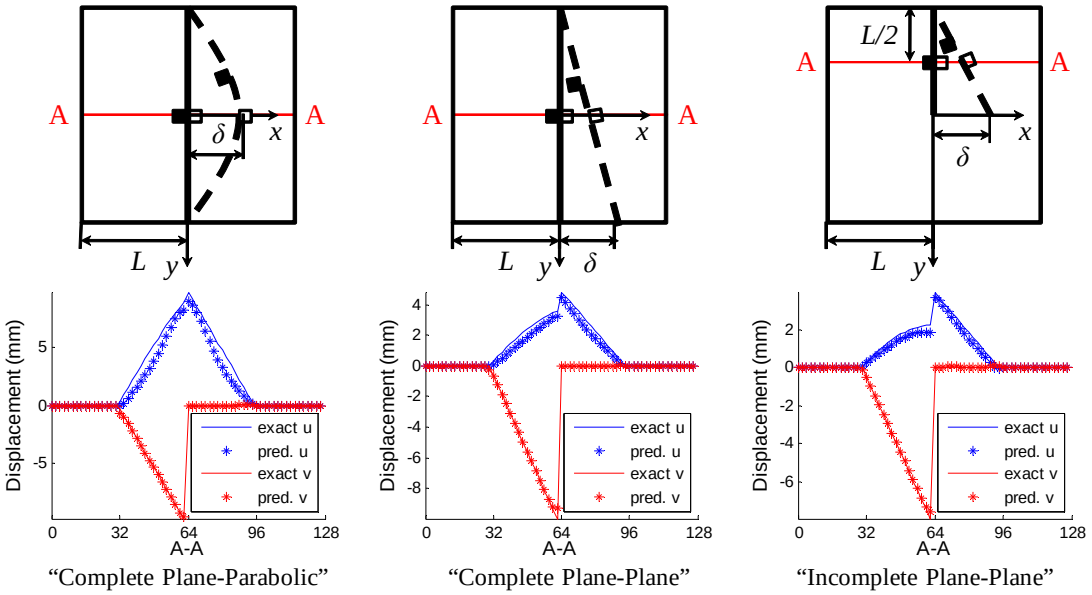

Figure 6.4: Top row shows the sketches for 2D synthetic cases. Left: Complete Plane-Parabolic, a complete plane "fissure" is deformed into a parabolic surface; Middle: Complete Plane-Plane, a complete plane "fissure" is deformed with changed orientation; Right: Incomplete Plane-Plane, an incomplete plane "fissure" is deformed with changed orientation. A pair of adjacent points on the initial interface (marked by filled and unfilled squares on the solid lines) is deformed into corresponding points on the dashed lines. A reference line A-A is marked in red. The bottom row shows the comparisons of $x-$ and y-components of displacements (u, v) between predicted results and exact solutions along A-A from left to right for the three cases, respectively. It can be seen that overall the proposed approach could recover the true deformation field for all the three cases. Discontinuities of both normal (u) and tangent (v) components of displacements for cases with complete or incomplete "fissures" are captured and are consistent with the ground truth.

BIBLIOGRAPHY

[1] Al-Mayah, A., Moseley, J., Brock, K. K., 2008. Contact surface and material nonlinearity modeling of human lungs. Physics in Medicine and Biology 53 (1), 305–317.

[2] Alford, S., van Beek, E., McLennan, G., Hoffman, E., 2010. Heterogeneity of pulmonary perfusion as a mechanistic image-based phenotype in emphysema susceptible smokers. Proceedings of the National Academy of Sciences 107 (16), 7485.

[3] Betke, M., Hong, H., Thomas, D., Prince, C., Ko, J. P., 2003. Landmark detection in the chest and registration of lung surfaces with an application to nodule registration. Medical Image Analysis 7, 265–281.

[4] Boldea, V., Sharp, G. C., Jiang, S. B., Sarrut, D., 2008. 4D-CT lung motion estimation with deformable registration: Quantification of motion nonlinearity and hysteresis. Medical Physics 35 (3), 1008–1018.

[5] Bookstein, F. L., Jun 1989. Principal warps: Thin-plate splines and the decomposition of deformations. IEEE Transactions on Pattern Analysis and Machine Intelligence 11 (6), 567–585.

[6] Byrd, R. H., Lu, P., Nocedal, J., Zhu, C., 1995. A limited memory algorithm for bound constrained optimization. SIAM Journal of Scientific Computing 16 (5), 1190–1208.

[7] Cao, K., Ding, K., Christensen, G. E., Reinhardt, J. M., 2010. Tissue volume and vesselness measure preserving nonrigid registration of lung CT images. In: SPIE Medical Imaging. Vol. 7623. p. 762309.

[8] Castillo, E., Castillo, R., Martinez, J., Shenoy, M., Guerrero, T., 2010. Four-dimensional deformable image registration using trajectory modeling. Physics in Medicine and Biology 55 (1), 305–327.

[9] Castillo, R., Castillo, E., Guerra, R., Johnson, V. E., McPhail, T., Garg, A. K., Guerrero, T., 2009. A framework for evaluation of deformable image registration spatial accuracy using large landmark point sets. Physics in Medicine and Biology 54 (7), 1849–1870.

[10] Chang, Y., 1999. A model of ventilation distribution in the human lung. Aerosol Science and Technology 30 (3), 309–319.

[11] Choi, J., Tawhai, M. H., Hoffman, E. A., Lin, C.-L., 2009. On intra- and inter-subject variabilities of airflow in the human lungs. Physics of Fluids 21 (10), 101901.

[12] Choi, Y., Lee, S., 2000. Injectivity conditions of 2D and 3D uniform cubic B-spline functions. Graphical Models 62 (6), 411–427.

[13] Chon, D., Beck, K. C., Simon, B. A., Shikata, H., Saba, O. I., Hoffman, E. A., 2007. Effect of low-xenon and krypton supplementation on signal/noise of regional CT-based ventilation measurements. Journal of Applied Physiology 102 (4), 1535–1544.

[14] Chon, D., Simon, B. A., Beck, K. C., Shikata, H., Saba, O. I., Won, C., Hoffman, E. A., 2005. Differences in regional wash-in and wash-out time constants for xenon-CT ventilation studies. Respiratory Physiology & Neurobiology 148 (1-2), 65–83.

[15] Christensen, G. E., Song, J. H., Lu, W., Naqa, I. E., Low, D. A., 2007. Tracking lung tissue motion and expansion/compression with inverse consistent image registration and spirometry. Medical Physics 34 (6), 2155–2163.

[16] Chun, S. Y., Fessler, J., Feb. 2009. A simple regularizer for B-spline nonrigid image registration that encourages local invertibility. IEEE Journal of Selected Topics in Signal Processing 3 (1), 159–169.

[17] Comerford, A., Forster, C., Wall, W., 2010. Structured tree impedance outflow boundary conditions for 3D lung simulations. Journal of Biomechanical Engineering 132, 081002.

[18] Coselmon, M. M., Balter, J. M., McShan, D. L., Kessler, M. L., 2004. Mutual information based CT registration of the lung at exhale and inhale breathing states using thin-plate splines. Medical Physics 31 (11), 2942–2948.

[19] Crum, W. R., Hartkens, T., Hill, D. L. G., 2004. Non-rigid image registration: Theory and practice. British Journal of Radiology 77, 140–153.

[20] Davis, M., Khotanzad, A., Flamig, D., Harms, S., June 1997. A physics-based coordinate transformation for 3-D image matching. IEEE Transactions on Medical Imaging 16 (3), 317–328.

[21] De Backer, J. W., Vos, W., Gorle, C., Germonpre, P., Partoens, B., Wuyts, F. L., Parizel, P. M., De Backer, M., 2008. Flow analyses in the lower airways: Patient-specific model and boundary conditions. Medical Engineering And Physics 30 (7), 872–879.

[22] Ding, K., Bayouth, J. E., Buatti, J. M., Christensen, G. E., Reinhardt, J. M., 2010. 4DCT-based measurement of changes in pulmonary function following a course of radiation therapy. Medical Physics 37 (3), 1261–1272.

[23] Ding, K., Yin, Y., Cao, K., Christensen, G. E., Lin, C.-L., Hoffman, E. A., Reinhardt, J. M., 2009. Evaluation of lobar biomechanics during respiration using image registration. In: Proc. MICCAI. Vol. 5761 of LNCS. London, UK, pp. 739–746.

[24] Dougherty, L., Asmuth, J. C., Gefter, W. B., 2003. Alignment of CT lung volumes with an optical flow method. Academic Radiology 10 (3), 249–254.

[25] Edwards, D., Hanes, J., Caponetti, G., Hrkach, J., Ben-Jebria, A., Eskew, M., Mintzes, J., Deaver, D., Lotan, N., Langer, R., 1997. Large porous particles for pulmonary drug delivery. Science 276 (5320), 1868.

[26] Eom, J., Xu, X., De, S., Shi, C., 2010. Predictive modeling of lung motion over the entire respiratory cycle using measured pressure-volume data, 4DCT images, and finite-element analysis. Medical Physics 37, 4389.

[27] Fan, L., Chen, C. W., Reinhardt, J. M., Hoffman, E. A., 2001. Evaluation and application of 3D lung warping and registration model using HRCT images. In: SPIE Medical Imaging. Vol. 4321. pp. 234–243.

[28] Freitas, R. K., Schrder, W., 2008. Numerical investigation of the three-dimensional flow in a human lung model. Journal of Biomechanics 41 (11), 2446–2457.

[29] Fuld, M. K., Easley, R. B., Saba, O., Chon, D., Reinhardt, J. M., Hoffman, E. A., Simon, B. A., 2008. CT measured regional specific volume change reflects regional specific ventilation in supine sheep. Journal of Applied Physiology 104 (4), 1177–1184.

[30] Gorbunova, V., Lo, P., Ashraf, H., Dirksen, A., Nielsen, M., de Bruijne, M., 2008. Weight preserving image registration for monitoring disease progressionin lung CT. In: Proc. MICCAI. Springer, New York, pp. 863–870.

[31] Grinberg, L., Karniadakis, G., 2008. Outflow boundary conditions for arterial networks with multiple outlets. Annals of Biomedical Engineering 36 (9), 1496–1514.

[32] Guerrero, T., Sanders, K., Castillo, E., Zhang, Y., Bidaut, L., Pan, T., Komaki, R., 2006. Dynamic ventilation imaging from four-dimensional computed tomography. Physics in Medicine and Biology 51, 777–791.

[33] Guerrero, T., Zhang, G., Huang, T., Lin, K., 2004. Intrathoracic tumor motion estimation from CT imaging using the 3D optical flow method. Physics in Medicine and Biology 49, 4147–4161.

[34] Han, X., 2010. Feature-constrained nonlinear registration of lung CT images. In: MICCAI 2010 Grand Challenges in Medical Image Analysis: Evaluation of Methods for Pulmonary Image Registration.

[35] Harris, R., Schuster, D., 2007. Visualizing lung function with positron emission tomography. Journal of Applied Physiology 102, 448458.

[36] Hoffman, E., Clough, A., Christensen, G., Lin, C., McLennan, G., Reinhardt, J., Simon, B., Sonka, M., Tawhai, M., van Beek, E., et al., 2004. The comprehensive imaging-based analysis of the lung:: A forum for team science. Academic Radiology 11 (12), 1370–1380.

[37] Hoffman, E., Tajik, J., Kugelmass, S., 1995. Matching pulmonary structure and perfusion via combined dynamic multislice CT and thin-slice high-resolution CT. Computerized Medical Imaging and Graphics 19, 101–112.

[38] Hoffman, E. A., 1985. Effect of body orientation on regional lung expansion: A computed tomographic approach. Journal of Applied Physiology 59, 468–480.

[39] Hoffman, E. A., Reinhardt, J. M., Sonka, M., Simon, B. A., J. Guo, O. S., Chon, D., Samrah, S., Shikata, H., Tschirren, J., Palagyi, K., Beck, K. C., McLennan, G., 2003. Characterization of the interstitial lung diseases via density-based and texture-based analysis of computed tomography images of lung structure and function. Academic Radiology 10 (10), 1104–1118.

[40] Hoffman, E. A., Ritman, E. L., 1985. Effect of body orientation on regional lung expansion in dog and sloth. Journal of Applied Physiology 59 (2), 481–491.

[41] Hogg, J. C., McDonough, J. E., Gosselink, J. V., Hayashi, S., 2009. What drives the peripheral lung-remodeling process in chronic obstructive pulmonary disease? Proceedings of the American Thoracic Society 6 (8), 668–672.

[42] Holden, M., Jan. 2008. A review of geometric transformations for nonrigid body registration. IEEE Transactions on Medical Imaging 27 (1), 111–128.

[43] Horsfield, K., Dart, G., Olson, D., Filley, G., Cumming, G., 1971. Models of the human bronchial tree. Journal of Applied Physiology 31 (2), 207–217.

[44] Hu, S., Hoffman, E. A., Reinhardt, J. M., Jun 2001. Automatic lung segmentation for accurate quantitation of volumetric X-ray CT images. IEEE Transactions on Medical Imaging 20 (6), 490–498.

[45] Johnson, H. J., Christensen, G. E., May 2002. Consistent landmark and intensity-based image registration. IEEE Transactions on Medical Imaging 21 (5), 450–461.

[46] Kabus, S., 2007. Multiple-material variational image registration. Ph.D. thesis, University of Lbeck.

[47] Kabus, S., Klinder, T., Murphy, K., van Ginneken, B., Lorenz, C., Pluim, J., 2009. Evaluation of 4d-ct lung registration. In: Proc. MICCAI. Springer, pp. 747–754.

[48] Kaus, M. R., Brock, K. K., Pekar, V., Dawson, L. A., Nichol, A. M., Jaffray, D. A., 2007. Assessment of a model-based deformable image registration approach for radiation therapy planning. International Journal of Radiation Oncology Biology Physics 68 (2), 572–580.

[49] Kilburn, K., 1984. Particles causing lung disease. Environmental Health Perspectives 55, 97.

[50] Klein, S., Staring, M., Murphy, K., Viergever, M., Pluim, J., 2010. elastix: a toolbox for intensity-based medical image registration. IEEE Transactions on Medical Imaging 29 (1).

[51] Klein, S., Staring, M., Pluim, J. P. W., 2007. Evaluation of optimization methods for nonrigid medical image registration using mutual information and B-splines. IEEE Transactions on Image Processing 16 (12), 2879–2890.

[52] Kruger, C., 2003. Constrained cubic spline interpolation for chemical engineering applications.

[53] Kumar, H., Tawhai, M. H., Hoffman, E. A., Lin, C.-L., 2009. The effects of geometry on airflow in the acinar region of the human lung. Journal of Biomechanics 42 (11), 1635–1642.

[54] Kybic, J., Unser, M., 2003. Fast parametric elastic image registration. IEEE Transactions on Medical Imaging 12 (11), 1427–1442.

[55] Lambert, A. R., OShaughnessy, P., Tawhai, M. H., Hoffman, E. A., Lin, C.-L., 2011. Regional deposition of particles in an image-based airway model: large-eddy simulation and left-right lung ventilation asymmetry. Aerosol Science and Technology 45 (1), 11–25.

[56] Lee, S., Wolberg, G., Chwa, K. Y., Shin, S. Y., 1996. Image metamorphosis with scattered feature constraints. IEEE Transactions on Visualization and Computer Graphics 2 (4), 337–354.

[57] Lee, S., Wolberg, G., Shin, S. Y., 1997. Scatter data interpolation with multilevel B-spline. IEEE Transactions on Visualization and Computer Graphics 3 (3), 1–17.

[58] Lee, Y., Oh, Y., Lee, J., Kim, E., Lee, J., Kim, N., Seo, J., Lee, S., 2008. Quantitative assessment of emphysema, air trapping, and airway thickening on computed tomography. Lung 186 (3), 157–165.

[59] Li, B., Christensen, G. E., Hoffman, E. A., McLennan, G., Reinhardt, J. M., 2003. Establishing a normative atlas of the human lung: intersubject warping and registration of volumetric CT images. Academic Radiology 10 (3), 255–265.

[60] Li, B., Christensen, G. E., McLennan, G., Hoffman, E. A., Reinhardt, J. M., 2008. Pulmonary CT image registration and warping for tracking tissue deformation during the respiratory cycle through 3-D consistent image registration. Medical Physics 35 (12), 5575–5583.

[61] Li, P., Malsch, U., Bendl, R., 2008. Combination of intensity-based image registration with 3D simulation in radiation therapy. Physics in Medicine and Biology 53 (17), 4621–4637.

[62] Lin, C.-L., Hoffman, E. A., 2005. A numerical study of gas transport in human lung models. In: SPIE Medical Imaging '05. Vol. 5746. SPIE, Bellingham WA, pp. 92–100.

[63] Lin, C.-L., Lee, H., Lee, T., Weber, L. J., 2005. A level set characteristic galerkin finite element method for free surface flows. International Journal for Numerical Methods in Fluids 49 (5), 521–548.

[64] Lin, C.-L., Tawhai, M. H., McLennan, G., Hoffman, E. A., 2007. Characteristics of the turbulent laryngeal jet and its effect onairflow in the human intra-thoracic airways. Respiratory Physiology & Neurobiology 157 (2-3), 295–309.

[65] Lin, C.-L., Tawhai, M. H., McLennan, G., Hoffman, E. A., 2009. Multiscale simulation of gas flow in subject-specific models of the human lung. IEEE Engineering in Medicine and Biology Magazine 28 (3), 25–33.

[66] Liu, Y., So, R., Zhang, C., 2003. Modeling the bifurcating flow in an asymmetric human lung airway. Journal of Biomechanics 36 (7), 951–959.

[67] Lorensen, W. E., Cline, H. E., 1987. Marching cubes: A high resolution 3D surface construction algorithm. Computer Graphics 21 (4), 163–169.

[68] Loring, S., ODonnell, C., Feller-Kopman, D., Ernst, A., 2007. Central airway mechanics and flow limitation in acquired tracheobronchomalacia. Chest 131 (4), 1118.

[69] Lubner, M. G., 2008. The incomplete fissure sign. Radiology 247 (2), 589–590.

[70] Ma, B., Lutchen, K., 2006. An anatomically based hybrid computational model of the human lung and its application to low frequency oscillatory mechanics. Annals of Biomedical Engineering 34 (11), 1691–1704.

[71] Ma, B., Lutchen, K., 2009. CFD simulation of aerosol deposition in an anatomically based human large-medium airway model. Annals of Biomedical Engineering 37, 271–285.

[72] Marcucci, C., Nyhan, D., Simon, B., 2001. Distribution of pulmonary ventilation using Xe-enhanced computed tomography in prone and supine dogs. Journal of Applied Physiology 90, 421–430.

[73] Milic-Emili, J., Henderson, J. A., Dolovich, M. B., Trop, D., Kaneko, K., 1966. Regional distribution of inspired gas in the lung. Journal of Applied Physiology 21 (3), 749–759.

[74] Muller, N., Staples, C., Miller, R., Abboud, R., 1988. "density mask". an objective method to quantitate emphysema using computed tomography. Chest 94, 782–787.

[75] Murphy, K., Ginneken, B., Pluim, J. P., Klein, S., Staring, M., 2008. Semi-automatic reference standard construction for quantitative evaluation of lung CT registration. In: Proc. MICCAI. Springer, New York, pp. 1006–1013.

[76] Nazridoust, K., Asgharian, B., 2008. Unsteady-state airflow and particle deposition in a three-generation human lung geometry. Inhalation Toxicology 20 (6), 595–610.

[77] Nowak, N., Kakade, P., Annapragada, A., 2003. Computational fluid dynamics simulation of airflow and aerosol deposition in human lungs. Annals of Biomedical Engineering 31 (4), 374–390.

[78] Paquin, D., Levy, D., Xing, L., 2007. Hybrid multiscale landmark and deformable image registration. Mathematical Biosciences and Engineering 4 (4), 711–737.

[79] Reinhardt, J. M., Ding, K., Cao, K., Christensen, G. E., Hoffman, E. A., Bodas, S. V., 2008. Registration-based estimates of local lung tissue expansion compared to xenon CT measures of specific ventilation. Medical Image Analysis 12 (6), 752–763.

[80] Rienmuller, R., Behr, J., Kalender, W., 1991. Standardized quantitative high resolution CT in lung diseases. J Comput Assist Tomogr 15, 742749.

[81] Rodarte, J. R., Hubmayr, R. D., Stamenovic, D., Walters, B. J., 1985. Regional lung strain in dogs during deflation from total lung capacity. Journal of Applied Physiology 58, 164–172.

[82] Rohr, K., Cathier, P., Wrz, S., 2004. Elastic registration of electrophoresis images using intensity information and point landmarks. Pattern Recognition 37 (5), 1035–1048.

[83] Rohr, K., Stiehl, H. S., Sprengel, R., Buzug, T. M., Weese, J., Kuhn, M. H., June 2001. Landmark-based elastic registration using approximating thin-plate splines. IEEE Transactions on Medical Imaging 20 (6), 526–534.

[84] Rueckert, D., Aljabar, P., Heckemann, R. A., Hajnal, J. V., Hammers, A., 2006. Diffeomorphic registration using B-splines. In: Proc. MICCAI. Springer, Copenhagen, pp. 702–709.

[85] Rueckert, D., Sonoda, L. I., Hayes, C., Hill, D. L. G., Leach, M. O., Hawkes, D. J., 1999. Nonrigid registration using free-form deformation: application to breast MR images. IEEE Transactions on Medical Imaging 18 (8), 712–721.

[86] Salerno, M., de Lange, E., Altes, T., Truwit, J., Brookeman, J., Mugler, J., 2002. Emphysema: Hyperpolarized helium 3 diffusion MR imaging of the lungs compared with spirometric indexesinitial experience. Radiology 222 (1), 252–260.

[87] Sarrut, D., Boldea, V., Miguet, S., Ginestet, C., 2006. Simulation of four-dimensional CT images from deformable registration between inhale and exhale breath-hold CT scans. Medical Physics 33 (3), 605–617.

[88] Sarrut, D., Delhay, S., Villard, P. F., Boldea, V., Beuve, M., Clarysse, P., 2007. A comparison framework for breathing motion estimation methods from 4-D imaging. IEEE Transactions on Medical Imaging 26 (12), 1636–1648.

[89] Schmidt-Richberg, A., Ehrhardt, J., Werner, R., Handels, H., 2009. Slipping objects in image registration: improved motion field estimation with direction-dependent regularization. In: Proc. MICCAI. London, UK, pp. 755–762.

[90] Schmidt-Richberg, A., Ehrhardt, J., Werner, R., Handels, H., 2010. Direction-dependent regularization for improved estimation of liver and lung motion in 4D image data. In: SPIE Medical Imaging. Vol. 7623. San Diego, US, p. 76232Y.

[91] Schreibmann, E., Chen, G., Xing, L., 2006. Image interpolation in 4D CT using a Bspline deformable registration model. International Journal of Radiation Oncology Biology Physics 64 (5), 1537–1550.

[92] Sdika, M., 2008. A fast nonrigid image registration with constraints on the Jacobian using large scale constrained optimization. IEEE Transactions on Medical Imaging 27 (2), 271–281.

[93] Shekhar, R., Lei, P., Castro-Pareja, C. R., Plishker, W. L., DSouza, W. D., 2007. Automatic segmentation of phase-correlated CT scans through nonrigid image registration using geometrically regularized free-form deformation. Medical Physics 34, 3054–3066.

[94] Shikata, H., Hoffman, E. A., Sonka, M., 2004. Automated segmentation of pulmonary vascular tree from 3D CT images. In: SPIE Medical Imaging. Vol. 5369. SPIE, pp. 107–116.

[95] Simon, B., Marcucci, C., Fung, M., Lele, S., 1998. Parameter estimation and confidence intervals for Xe-CT ventilation studies: a monte carlo approach. Journal of Applied Physiology 84, 709–716.

[96] Simon, B. A., 2000. Non-invasive imaging of regional lung function using X-ray computed tomography. Journal of Clinical Monitoring and Computing 16, 433–442.

[97] Sluimer, I. C., Prokop, M., van Ginneken, B., 2005. Towards automated segmentation of the pathological lung in CT. IEEE Transactions on Medical Imaging 24 (8), 1025–1038.

[98] Spilker, R., Feinstein, J., Parker, D., Reddy, V., Taylor, C., 2007. Morphometry-based impedance boundary conditions for patient-specific modeling of blood flow in pulmonary arteries. Annals of Biomedical Engineering 35 (4), 546–559.

[99] Stapleton, K., Guentsch, E., Hoskinson, M., Finlay, W., 2000. On the suitability of k–ε turbulence modeling for aerosol deposition in the mouth and throat: A comparison with experiment. Journal of Aerosol Science 31 (6), 739–749.

[100] Staring, M., Klein, S., Pluim, J. P. W., 2007. A rigidity penalty term for nonrigid registration. Medical Physics 34 (11), 4098–4108.

[101] Stoel, B. C., Bode, F., Rames, A., Soliman, S., Reiber, J. H. C., Stolk, J., 2008. Quality control in longitudinal studies with computed tomographic densitometry of the lungs. The Proceedings of the American Thoracic Society 5 (9), 929–933.

[102] Sundaram, T. A., Gee, J. C., 2005. Towards a model of lung biomechanics: pulmonary kinematics via registration of serial lung images. Medical Image Analysis 9, 524–537.

[103] Tajik, J., Chon, D., Won, C., Tran, B., Hoffman, E., 2002. Subsecond multisection CT of regional pulmonary ventilation. Academic Radiology 9, 130–46.

[104] Taubin, G., 1995. Curve and surface smoothing without shrinkage. In: Proceedings of the 5th International Conference on Computer Vision '95. Washington, DC, pp. 852–857.

[105] Tawhai, M. H., Hunter, P., Tschirren, J., Reinhardt, J. M., McLennan, G., Hoffman, E. A., 2004. CT-based geometry analysis and finite element models of the human and ovine bronchial tree. Journal of Applied Physiology 97 (6), 2310–2321.

[106] Tawhai, M. H., Hunter, P. J., 2001. Multibreath washout analysis: modelling the influence of conducting airway asymmetry. Respiration Physiology 127 (2-3), 249–258.

[107] Tawhai, M. H., Lin, C.-L., 2010. Image-based modeling of lung structure and function. Journal of Magnetic Resonance Imaging 32, 1421–1431, accepted for publication.

[108] Tawhai, M. H., Nash, M. P., Hoffman, E. A., 2006. An imaging-based computational approach to model ventilation distribution and soft-tissue deformation in the ovine lung. Academic Radiology 13 (1), 113–120.

[109] Tawhai, M. H., Nash, M. P., Lin, C.-L., Hoffman, E. A., 2009. Supine and prone differences in regional lung density and pleural pressure gradients in the human lung with constant shape. Journal of Applied Physiology 107 (3), 912–920.

[110] Taylor, D. J., Doorly, D. J., Schroter, R. C., 2010. Inflow boundary profile prescription for numerical simulation of nasal airflow. Journal of The Royal Society Interface 7 (44), 515–527.

[111] Torigian, D. A., Gefter, W. B., Affuso, J. D., Emami, K., Dougherty, L., 2007. Application of an optical flow method to inspiratory and expiratory lung MDCT to assess regional air trapping: a feasibility study. American Journal of Roentgenology 188 (3), 276–280.

[112] Tschirren, J., Hoffman, E. A., McLennan, G., Sonka, M., Dec. 2005. Intrathoracic airway trees: segmentation and airway morphology analysis from low-dose CT scans. IEEE Transactions on Medical Imaging 24 (12), 1529–1539.

[113] Tustison, N., Avants, B., Gee, J., 2009. Directly manipulated free-form deformation image registration. IEEE Transactions on Image Processing 18 (3), 624–635.

[114] Ukil, S., Reinhardt, J., 2009. Anatomy-guided lung lobe segmentation in x-ray ct images. IEEE Transactions on Medical Imaging 28 (2), 202–214.

[115] van Beek, E. J. R., Wild, J. M., Kauczor, H. U., Schreiber, W., Mugler, J. P., de Lange, E. E., 2004. Functional MRI of the lung using hyperpolarized 3-helium gas. Journal of Magnetic Resonance Imaging 20 (4), 540–554.

[116] van Ertbruggen, C., Hirsch, C., Paiva, M., 2005. Anatomically based three-dimensional model of airways to simulate flow and particle transport using computational fluid dynamics. Journal of Applied Physiology 98 (3), 970–980.

[117] van Rikxoort, E., Prokop, M., de Hoop, B., Viergever, M., Pluim, J., van Ginneken, B., 2009. Automatic segmentation of the pulmonary lobes from fissures, airways, and lung borders: evaluation of robustness against missing data. In: Proc. MICCAI. London, UK, pp. 263–271.

[118] Vreman, A., 2004. An eddy-viscosity subgrid-scale model for turbulent shear flow: Algebraic theory and applications. Physics of Fluids 16, 3670.

[119] Wall, W., Rabczuk, T., 2008. Fluid-structure interaction in lower airways of CT-based lung geometries. International Journal for Numerical Methods in Fluids 57 (5), 653–675.

[120] Weibel, E. R., 1963. Morphometry of the human lung. Academic, New York.

[121] Werner, R., Ehrhardt, J., Schmidt, R., Handels, H., 2009. Patient-specific finite element modeling of respiratory lung motion using 4D CT image data. Medical Physics 36 (5), 1500–1511.

[122] Wolfkiel, C., Rich, S., 1992. Analysis of regional pulmonary enhancement in dogs by ultrafast computed tomography. Investigative Radiology 27, 211–216.

[123] Worz, S., Rohr, K., 2008. Physics-based elastic registration using non-radial basis functions and including landmark localization uncertainties. Computer Vision and Image Understanding 111 (3), 263–274.

[124] Wu, Z., Rietzel, E., Boldea, V., Sarrut, D., Sharp, G. C., 2008. Evaluation of deformable registration of patient lung 4DCT with subanatomical region segmentations. Medical Physics 35 (2), 775–781.

[125] Xia, G., Tawhai, M. H., Hoffman, E. A., Lin, C.-L., 2010. Airway wall stiffening increases peak wall shear stress: a fluid-structure interaction study in rigid and compliant airways. Annals of Biomedical Engineering 38, 1836–1853.

[126] Xie, Y., Chao, M., Xing, L., 2009. Tissue feature-based and segmented deformable image registration for improved modeling of shear movement of lungs. International Journal of Radiation Oncology Biology Physics 74 (4), 1256–1265.

[127] Yang, D., Lu, W., Low, D. A., Deasy, J. O., Hope, A. J., El Naqa, I., 2008. 4D-CT motion estimation using deformable image registration and 5D respiratory motion modeling. Medical Physics 35, 4577.

[128] Yin, Y., Hoffman, E. A., Ding, K., Reinhardt, J. M., Lin, C.-L., 2011. A cubic B-spline-based hybrid registration of lung CT images for a dynamic airway geometric model with large deformation. Physics in Medicine and Biology 56 (1), 203–218.

[129] Yin, Y., Hoffman, E. A., Lin, C.-L., 2009. Local tissue-weight-based non-rigid registration of lung images with application to regional ventilation. In: Proceedings of SPIE Medical Imaging. Vol. 7262. Orland, US, p. 72620C.

[130] Yin, Y., Hoffman, E. A., Lin, C.-L., 2009. Mass preserving nonrigid registration of CT lung images using cubic B-spline. Medical Physics 36 (9), 4213–4222.

[131] Yin, Y., Hoffman, E. A., Lin, C.-L., 2010. Lung lobar slippage assessed with the aid of image registration. In: Jiang, T., Navab, N., Pluim, J., Viergever, M. (Eds.), Medical Image Computing and Computer-Assisted Intervention MICCAI 2010. Vol. 6362 of Lecture Notes in Computer Science. Springer Berlin / Heidelberg, Beijing, China, pp. 578–585.